Time Resolved Spectroscopy of Strongly Correlated Materials

Dissertation
zur Erlangung des Grades
Doktor der Naturwissenschaften (Dr. rer. nat.)
am Fachbereich Physik, Mathematik und Informatik
der Johannes Gutenberg-Universität Mainz

von:
Amrit Raj Pokharel
geboren in Tanahun, Nepal (NP)
Mainz, 2022

Amrit Raj Pokharel

Time Resolved Spectroscopy of Strongly Correlated Materials

Datum der mündlichen Prüfung: 25. Januar, 2023

Gutachter:	Aus Datenschutzgründen entfernt / Removed due to data privacy
Kommission:	Aus Datenschutzgründen entfernt / Removed due to data privacy

Johannes Gutenberg Universität Mainz
AG Demsar
Institut für Physik
Staudingerweg 7
55128, Mainz

Eidesstattliche Erklärung

Hiermit erkläre ich an Eides statt, dass ich meine Dissertation selbständig und ohne fremde Hilfe verfasst und keine anderen als die von mir angegebenen Quellen und Hilfsmittel zur Erstellung meiner Dissertation verwendet habe. Die Arbeit ist in vorliegender oder ähnlicher Form bei keiner anderen Prüfungsbehörde zur Erlangung eines Doktorgrades eingereicht worden.

Mainz, den

Amrit Raj Pokharel

Abstract

Strongly correlated materials are systems for which the complex interplay among the electrons, spin and lattice lead to the formation of different phase transitions and new orders with dramatically different electrical, optical, mechanical and thermal properties. Emergence of complex phases like- Charge Density Wave (CDW), Spin Density Wave (SDW), Superconductivity just to name a few, with remarkable properties offer great deal (such as an order of magnitude change in electrical conductivity) from fundamental research perspective and thought to shape our future technologies. Non-equilibrium spectroscopic techniques are ideal tools to investigate such correlated systems as the techniques offer simultaneous spectroscopic and temporal information. In addition, driving the system out of equilibrium and tracking the relaxation dynamics and their couplings, one can disentangle the different degrees of freedom because of the different timescales that characterize the recovery of the initial ground state.

The work described in this thesis utilizes the ultrafast spectroscopic technique as a tool to investigate the solid state materials exhibiting Charge Density Wave (CDW) order, Kondo Insulating (KI) behavior and Mott Insulating (MI) ground state. All of these materials fall into the category of strongly correlated systems where multiple phases emerges due to correlation effects. In the Kondo Insulator YbB_{12} we track the photo-induced reflectivity dynamics at various temperatures and excitation densities and discuss the corresponding changes in the

low energy electronic structure. In CDW system $BaNi_2As_2$ we study the collective amplitude modes of the CDW order and their temperature and excitation density dependence. These results provide valuable information on the nature of the CDW order and its relation to the observed structural phase transitions. In particular, the smooth evolution of several amplitude modes through the structural phase transitions suggest that CDW may be responsible for the triclinic phase transition. Moreover, robustness of the CDW order against perturbation suggest an unconventional, non-Peierls nature of the CDW order. Last, but not least, we present the time-resolved study on photo-doping the Mott insulator La_2CuO_4. By tracking the time evolution of the complex dielectric function over the broad spectral range, we study the dynamics of the charge transfer gap and the appearance of the mid-infrared excitations. By varying the excitation densities over three order of magnitude we demonstrate the extreme resilience of the Mott insulating ground state against perturbation.

Kurzfassung

Stark korrelierte Materialien sind Systeme, bei denen das komplexe Zusammenspiel zwischen Elektronen, Spin und Gitter zur Bildung verschiedener Phasenübergänge und neuer Ordnungen mit dramatisch unterschiedlichen elektrischen, optischen, mechanischen sowie thermischen Eigenschaften führen. Das Entstehen komplexer Phasen, wie Ladungsdichtewellen (Charge Density Wave, CDW), Spin-Dichtewellen (Spin Density Wave, SDW) und Supraleitung, um nur einige zu nennen, mit bemerkenswerten Eigenschaften (bspw. eine Veränderung der elektrischen Leitfähigkeit um eine Größenordnung), ist nicht nur in der Grundlagenforschung interessant sind sondern auch um neue Technologien zu realisieren. Spektroskopische Nicht-Gleichgewichts-Techniken sind ideale Instrumente zur Untersuchung solcher korrelierten Systeme, da sie gleichzeitig spektroskopische und zeitliche Informationen liefern. Zudem ermöglicht das Beobachten der Relaxationsdynamiken eines aus dem Gleichgewicht gestoßenen Systems unter anderem die Bestimmung der relevanten Kopplungen, sowie die Charakterisierung verschiedener Zeitskalen, welche bei der Rückkehr zum Gleichgewichtszustand auftreten.

Die in dieser Thesis beschriebenen Techniken nutzen ultraschnelle Spektroskopie als Werkzeug zur Untersuchung von Festkörpermaterialien, in welchen Ladungsdichtewellen-Ordnung (Charge Density Wave, CDW), Kondo-Isolation (KI) oder Mott-Isolation auftritt. Alle diese Materialien fallen in die Kategorie der stark korrelierten Sys-

teme, in denen aufgrund von Korrelationseffekten mehrere Phasen existieren. Im Kondo-Isolator YbB_12 werden die Dynamiken der Veränderungen in der elektronischen Struktur bei niedrigen Energien durch die Verfolgung der photoinduzierten Reflektivität bei verschiedenen Temperaturen und Anregungsdichten diskutiert. Im CDW-System $BaNi_2As_2$ untersuchen wir die kollektiven Amplitudenmoden der CDW-Ordnung sowie deren Abhängigkeit von Temperatur und Anregungsdichte. Hervorzuheben ist die gleichmäßige Veränderung mehrerer Amplitudenmoden beim Durchlaufen des strukturellen Phasenübergangs, welche darauf hindeutet, dass die CDW-Ordnung für den Übergang in eine trikline Phase verantwortlich ist. Des Weiteren deutet die Robustheit der CDW-Ordnung gegenüber Störungen auf eine unkonventionelle, nicht Peierls konforme, Natur der CDW-Ordnung. Zu guter Letzt präsentieren wir unsere Ergebnisse zum photoinduzierten Dopen des Mott-Isolators La_2CuO_4., bei welchem wir die zeitliche Entwicklung der komplexen dielektrischen Funktion über einen breiten Spektralbereich verfolgen und somit die Dynamik der Ladungstransferlücke, sowie Anregungen im mittleren Infrarotbereich untersuchen. Durch Variation der Anregungsdichten über drei Größenordnungen demonstrieren wir eine bemerkenswerte Resilienz des Mott-Grundzustands gegenüber Störungen.

Contents

Acronyms

AFM	Antiferromagnetic. 4, 94, 115
C-CDW	commensurate charge density wave. 60, 69, 81, 83
CDW	Charge Density Wave. 2–6, 53–56, 58–60, 78, 81, 83, 115, 116, 123
DOS	Density of States. 29
EHPs	Electron-Hole Pairs. 39–43, 45–47
EPC	electron-phonon coupling. 58
FFT	Fast Fourier Transform. 71, 75
HFPs	high frequency phonons. 39–41, 45, 46
HFs	Heavy Fermion Systems. 5, 27–30, 32, 39, 51
I-CDW	incommensurate charge density wave. 60, 69, 81, 85
KI	Kondo Insulator. 5, 28–30, 32, 33, 39, 51, 115
LHB	Lower Hubbard Band. 88
PLD	periodic lattice distortion. 54, 61
TMD	Transition-metal dichalcogenide. 53, 58
UHB	Upper Hubbard Band. 88

CHAPTER 1

INTRODUCTION

Microscopic understanding of the origin of emergent collective phenomena in strongly correlated materials represent perhaps one of the greatest unsolved problem in condensed matter physics. On one hand, fundamental properties like electrical, mechanical and thermal properties of simple metals, some semiconductors and insulators are understood reasonably well both in terms of theory and experiment within the view of non-interacting electrons approximation in solids. On the other hand, complex materials with partially filled d and f electron shells, have properties complicated to explain [1]. In contrast to commonly used materials like silicon and aluminium where the kinetic energy of the electrons dominates, the strongly correlated materials are fundamentally affected by the strong electron-electron interaction (Coulomb repulsion) [2]. In case of materials with strong electron-electron interaction, one cannot treat the single electron independently as embedded in a static mean field generated by the other electrons, simply because the influence of an electron on other electrons is too pronounced to be neglected [1]. The prime example of such is the

Mott insulating ground state in some materials. The complex internal interplay between multiple degree of freedom - spin, charge, lattice - can exhibit remarkable properties and transitions between distinct, competing symmetry-broken ground states with dramatically different electronic, and magnetic ordering at low temperature (see Fig. 1.1 as an example). These rich and fascinating phenomenon arising from complex correlation offer great deal from fundamental research perspective and also offer the possibilities of technological relevant features such as an order of magnitude change in electrical resistivity in metal-insulator transition or colossal magnetoresistance in manganites [2] . However, emergence of different properties comes with a greatest challenges in understanding, controlling and predicting the complexity in the strongly correlated materials and still remains the topic of intense debate.

One of the best known example of interaction of lattices and electrons in solids is the discovery of Superconductivity in the early 1900s [3], which was then gradually understood when the first theory (BCS-theory) of superconductivity emerges [4]. The theory explains the interaction of the electrons and phonons leads to the formation of the so-called Cooper pairs. The condensation of cooper pairs generate quantum phenomena called superconductivity when temperature decreases to transition temperature T_c.

Soon, another type of ordering called Charge Density Wave (CDW) order has been theoretically conceptualized by Peierls in 1955 [5], where he pointed out that one-dimensional electron system is unstable when electron-phonon coupling is taken into account. Such a coupling leads to the redistribution of the conduction electron density forming a periodic charge density modulation accompanied by the periodic lattice distortion. In fact CDW order can be realized

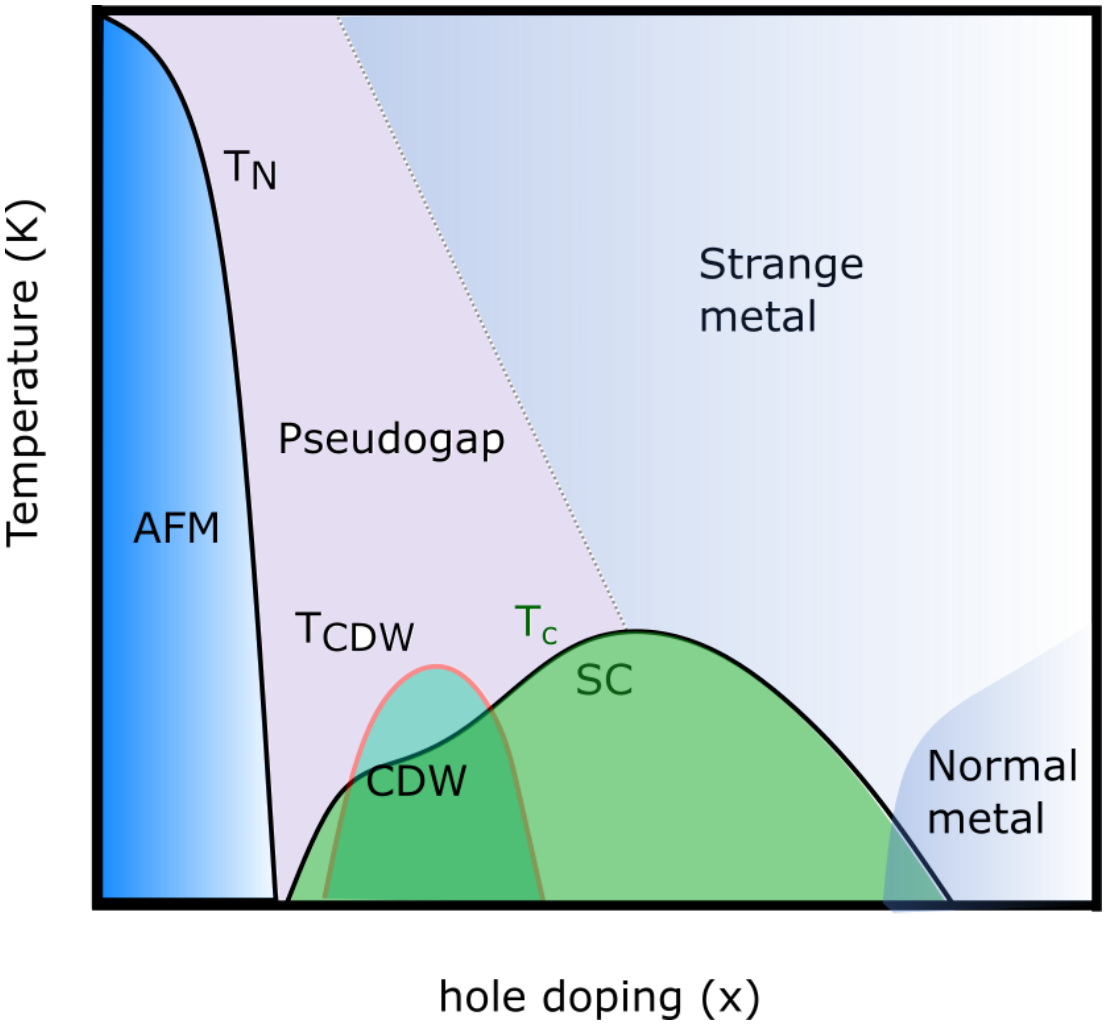

Figure 1.1: Generic phase diagram of hole doped cuprates with various doping level indicating the emergence of different phases. Antiferromagnetic order and the superconducting dome is represented by the blue and green region respectively. The red outlined area is the charge density wave order setting in at T_{CDW}. Emergence of several other phases are marked accordingly.

also in 2D and 3D system [6–8]. In some materials, CDW phase is found in the proximity of superconducting phase and the two often compete with each other. Furthermore, another type of materials called heavy fermion systems further gain on scientific interest where the mobile carriers at low temperature were found to have mass thousand times larger than the free electron mass. Here, the existence of localized magnetic moments and a large on-site Coulomb repul-

sion leads to an antiferromagnetic exchange interaction with the surrounding conduction sea of electrons. Heavy fermions are systems with strong correlation effects where different phases were realized ranging from superconductivity to Kondo insulating quantum critical phenomena to fermi liquid behaviours. Here, magnetic correlations are believed to drive the superconductivity [9]. The era of high temperature superconductivity emerged in mid-1980s, when the superconductivity was realized in layered structure La-Ba-Cu-O ceramics [10]. Ever since many materials are synthesized and the critical temperature was raised rapidly. Here, correlation between charge, spin and lattice play an important role, however the topic is still under intense debate and a common understanding of emergence of superconductivity in this class of materials is still missing. Finally, discovery of superconductivity in iron-based compounds [11–15], in the proximity to the magnetically ordered state, come as a new paradigm in the field of strongly correlated materials. The magnetic order in these systems is believed to play an important role in the emergence of superconductivity, however, wide consensus is yet to come. Figure 1.1 presents one of the generic phase diagram of hole doped cuprates, where multiple phase seem to exist ranging from Antiferromagnetic (AFM) order, CDW order, to Superconductivity. Figure 1.1 provides an example with different phases that could arise in the correlated electron systems.

Therefore, understanding such different quantum phases of matter that often compete with each other pose one of the main challenge in modern condensed matter physics. Due to multiple degree of freedom, strongly correlated materials are very sensitive to small changes in the external parameters like - pressure, doping, temperature, etc. By applying external perturbation and controlling the external parameters one can induce changes in the low energy electronic struc-

ture in materials and study the competition between different phases. Furthermore, by applying external stimuli and bringing the system out of equilibrium one can study the interplay among electrons, lattice and spin dynamics and can be disentangled because of the different timescales that characterize the recovery of the initial ground state. This concept became apparent when the ultrafast lasers with pulse duration ranging from few to several hundred femtosecond has been realized. To this end, we apply femtosecond laser pulses as an external knob to control the transient electronic state on a femtosecond timescale. By driving the system out of equilibrium with ultrafast laser pulses, we study the dynamical evolution of different phases in real time.

In this thesis, we utilize the time-resolved techniques to study the photo-induced dynamics in three different correlated materials. This thesis is divided into four main chapters.

The chapter 2 introduces the experimental technique used for studying the carrier relaxation dynamics in different materials in this thesis. The chapter discusses advancement of the technique for extraction of data with high signal to noise ratio from the pump-probe experiment.

Chapter 3 present the time resolved pump-probe study in Kondo Insulator (KI). Here, we start with basic concept of Heavy Fermion Systems (HFs) and KI. Detail analysis of the experimental data demonstrate the emergence of hybridization gap upto the temperature nearing room temperature and the robust nature of the hybridization gap against electronic excitation.

Chapter 4 present an approach to use pump-probe to study the collective modes in $BaNi_2As_2$, demonstrating the CDW nature of it's ground state. Here,

we start by introducing the basic concept of CDW. By studying the collective dynamics in $BaNi_2As_2$, we demonstrate the existence of multiple CDW amplitude modes and discuss their unconventional origin.

Chapter 5 discusses the photo-doping phenomena in charge transfer insulator, La_2CuO_4. Utilizing broadband spectroscopic technique and analysing the experimental data, we discuss the changes in the low energy electronic structure. By studying the changes in the complex dielectric function over three order of magnitude in excitation density, we discuss the absence of metallicity, where in the case of comparable chemical doping a metallic state is realized.

CHAPTER 2

Experimental Techniques

The field of ultrafast time resolved spectroscopy and its implications have grown as one of the most prominent tools to investigate the dynamics in condensed matter systems. The progress in this field has culminated in the generation and detection of attosecond ($\approx 10^{-18}$s) pulses [16], making it possible to study the elementary excitations and fundamental processes on a timescale with unprecedented resolution. This chapter starts with the introduction to the laser laboratory and the commercial laser system which has been extensively used in the course of this thesis. The conceptual design and implementation of pump probe technique and the steps towards improvement in the detection scheme for high signal to noise ratio is discussed.

This chapter facilitates the reader with insight into the fundamental concept of time resolved technique and its application in strongly correlated material systems.

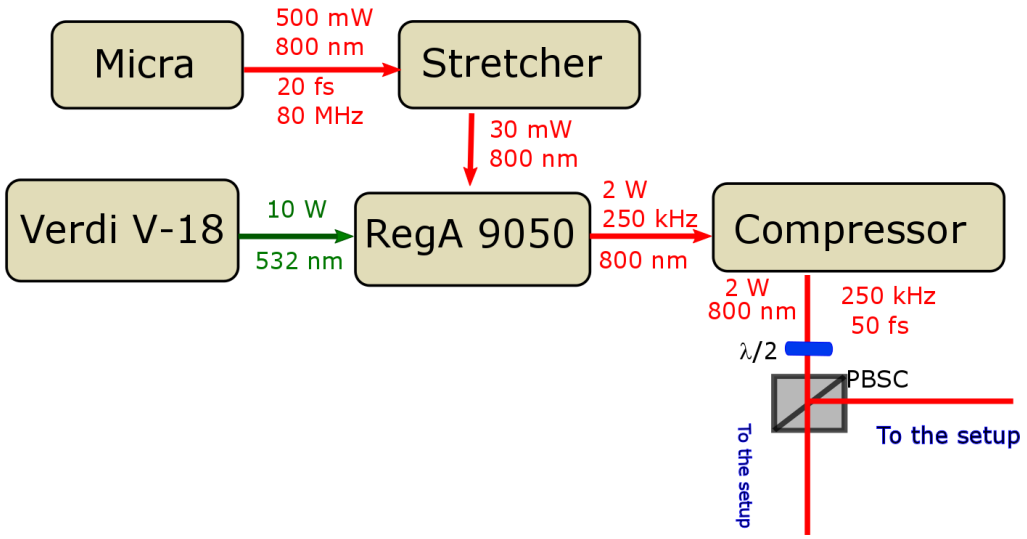

Figure 2.1: Schematic of the laser laboratory. Micra oscillator with MHz repetition rate with fundamental wavelength (λ) of 800 nm is used as a seeding beam for the RegA amplifier. The temperature stabilized "Verdi V-18" pumped amplifier outputs the power $\approx$ 2 W with 250 kHz repetition rate and with pulse energy in the μJ range.

2.1 Femtosecond Laser Source

For performing the time resolved measurements, ultrashort laser pulses are generated by commercial temperature stabilized mode-locked Titanium-Sapphire (Ti:Sa) laser system, manufactured and supplied by Coherent Inc, were used. Two laser system namely *Coherent: Micra* oscillator and *Coherent: RegA* amplifier is used to perform experiments in our laser laboratory. The basic layout of the laser system is shown in figure 2.1.

Coherent: Micra oscillator is a compact Ti:Sa femtosecond oscillator operating at a repetition rate of 80 MHz (12.5 ns pulse-to-pulse). The Ti:Sa oscillator is pumped with temperature tuned frequency doubled Nd:YVO_4 continuous wave (cw) solid state laser with average output power of 5 W. Using principle of Kerr lens modelocking, the oscillator is designed to passively stabilize the

mode-locked operation with short pulse with high energy exiting the cavity with average power of ≈ 500 mW. The emitted laser pulse wavelength (λ) offers tunability ranging from 710 - 980 nm, with the spectral bandwidth (full width at half maximum - FWHM) of $<$ 30 nm to $>$ 100 nm making the temporal pulse width of 30 fs down to sub-10 fs. The output of the laser pulse is adjusted to 800 nm (1.55 eV) with the prism compressor and provide the operation with approximately 20 fs resolution. The highest emitted pulse energy is then estimated by $E_{pulse} \approx 500\ mW/80\ MHz = 6.25\ nJ$

The femtosecond oscillator operating at 80 MHz produces the pulse energy in the sub 10 nJ regime and is optimal for weak perturbation regime when performing pump-probe experiment. On the other hand, one of the major drawback of the 80 MHz oscillator is the accumulation of steady-state heating on the sample of interest because of the high repetition rate in the MHz range. As a result, the effective temperature of the sample can increase substantially, hindering the study of the photo-induced dynamics with the fast recovery timescale. In this case, steady state heating needs to be considered while studying photo-excited dynamics even at low excitation densities.

To overcome the limitations of an oscillator and to study the non-linear dynamics of the solids, regenerative amplifier (*Coherent: RegA*) is applied where the *Micra Ti:Sa* oscillator is being used as a seeding laser and RegA is amplifying the pulse energy from nJ to μJ range. The output of the *Micra* oscillator pulses are first temporally stretched to about 10 ps using an external grating before entering the amplifier, to prevent the non linear effects inside the cavity, which could damage the sensitive optics. The stretched pulsed enters the cavity of the Nd:YVO_4 continuous wave (cw) laser pumped regenerative amplifier via an op-

tical switch in a double pass configuration. At each round trip of the pulse in the cavity, the pulse get amplified in the Ti:Sa crystal. After approximately 25 round trips the cavity dumper ejects the amplified pulse which is then compressed by a grating compressor to a pulse of 50-70 fs. At a repetition rate of 250-300 kHz, the *RegA* output power is $P \approx 2$ W with a pulse energy ≈ 6 μJ, the central wavelength is 800 nm and the spectral width of 30 nm. Detail principle of operation of the amplifier system is found in the original paper. [17]

2.2 Time resolved pump probe Spectroscopy

Time resolved pump-probe spectroscopy represents an ideal tool to investigate the ultrafast response of the strongly correlated electron systems such as Heavy Fermion Systems (HFs), Charge Density Waves (CDW), high temperature superconductors, just to name a few. In its simplest form, the output of the laser is split into two : the pump beam and the probe beam. First, the strong pump pulse drives the system out of equilibrium. The initial excited state exhibits a relaxation processes on the femtosecond to picosecond timescales. A second (weaker) probe beam measures the pump-induced changes as a function of time delay either in transmission (ΔT) or in reflection (ΔR). The technique harness the evolution of the pump induced excited state as a function of time delay of the probe pulse with respect to the pump pulse and hence the term pump-probe spectroscopy. In a standard all-optical pump-probe setup, the sample is excited with pump pulse (operating at certain wavelength) and the pump-induced changes are monitored with probe beam operating at the same wavelength. However, probing of the pump-induces changes can be obtained by using other non-linear optical methods. One example is broadband White light supercontinumm that allows to measure the pump-induced changes of the sample over the broad spec-

tral range. Similarly, probing can be extended in the THz region.

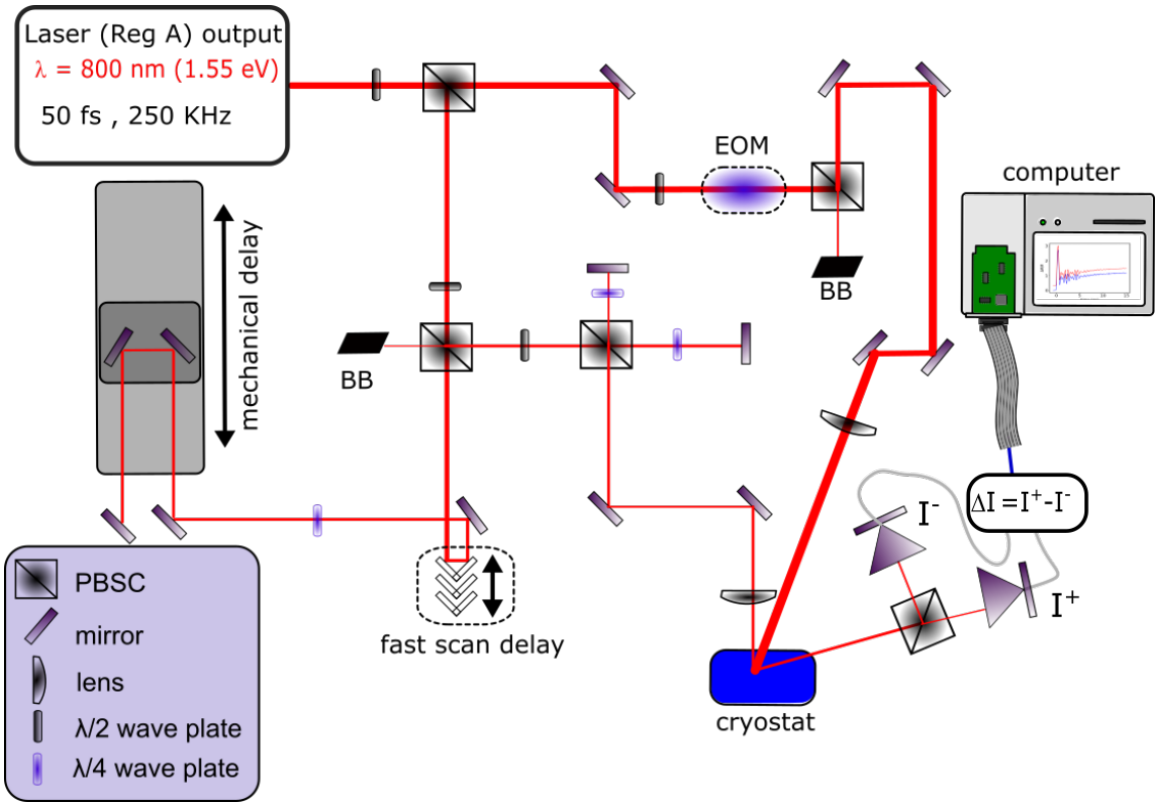

Figure 2.2: Schematic of the pump probe setup in the reflection geometry. The laser output is split into two portions, pump and the probe with the help of $\lambda/2$ and the polarizing beam splitter (PBSC). The pump and the probe transverse in the different optical path finally meeting again in space and time at the sample position. The probe beam is further split into two - the probe and the reference for the balance detection. The reference beam arrives at the sample position before the pump beam and measures the reflectivity of the sample without pump excitation. Different optical components (labeled in the figure) common for all optical setups are used to guide the beam for spatial and temporal overlap at the sample position. Beam blocker (BB) blocks the rejected beam.

Figure 2.2 presents the schematic of the pump-probe setup in the reflection geometry designed for studying different materials presented in this thesis. All the optical components used in the setup are common for all-optical experiments. The output beam of the regenerative amplifier is splits into stronger pump beam with vertical polarization (p-polarized) and the weaker probe beam with hori-

zontal polarization (s-polarized). The intensity of the beam and it's polarization is controlled with the help of the half-wave plate ($\lambda/2$) and the polarizing beam splitter cube (PBSC). Both the pump and the probe beams travel through different optical components along different paths yet travelling the same distance and finally meeting again (both in space and in time) at the sample position. In the probe arm, a mechanical stage is used to control the time delay between the pump and the probe beam in the double pass configuration. The mechanical delay stage is mainly used to find the time overlap of the pump and probe at the sample position. After determining the zero time-delay, the mechanical stage position is fixed during the measurement. A periodically driven shaker mounted with a retroreflector modulates the time delay between the pump and the probe beam during the measurement. Depending on the shaker oscillating frequency and the amplitude of oscillation, time delays up to 100 ps (200 ps in double pass) corresponding to the shaker travelling distance of 15 mm (measurement time window) can be obtained. This so called fast-scan technique is advantageous over conventional (slow) scan with mechanical delay stage during data acquisition and helps in enhancement of signal to noise ratio and will be discussed later in this chapter. The probe beam is then guided with additional optical components and focused at the sample position with an achromatic lens resulting in a beam diameter of ≈ 50 μm on the sample (standard configuration). On the other hand, the pump beam traverse through various optical components and makes a detour to have a similar path length as of the probe beam. The pump beam is focused down to ≈ 100 μm at the sample position [1]. The pump beam is modulated with electro-optical modulator (EOM) (discussed in 2.3) for enhanc-

[1]The spot size of the pump beam is larger than the probe beam to ensure a better spatial overlap of the pump and probe beam and to ensure a homogeneous probing of the pump volume after excitation.

ing signal to noise ratio during data acquisition. The end mirrors in the pump beam path are used to obtain the spatial overlap of the pump beam with the probe beam at the sample position. This completes the optical path length and design of the single color pump-probe setup.

2.3 Signal to noise enhancement and detection scheme

The state of the art pump probe spectroscopy allows to study the excitation and decay processes in materials and to extract the physics governing such phenomena. Using excitation densities as low as 1 $\mu J/cm^2$, recording differential changes on the order of 10^{-6} can be achieved either in transmission or reflection. However, measuring small changes comes with a great challenge in the detection because of various source of noise that could add up in the pump-probe signal. First and foremost, the photo-diode used for photo detection can react to other source of light in the laser laboratory. Second, the laser system have the pulse to pulse stability in the order of 10^{-3}. If the measurement time is long enough - several minutes to several hours- the pump-probe signal could be affected even by the external factors like changes in humidity and temperature and vibrations in the laser laboratory.

In order to reduce possible sources of noise and enhance the detected signal to noise ratio, the detection technique has to be designed carefully. Here, we discuss the data acquisition and detection schemes that are commonly in practice and also discuss the techniques that we harness in our optical pump probe setup.

2.3.1 Lock-in Detection Technique

Lock-in detection technique is one of the conventional detection scheme where the signal to noise ratio is substantially enhanced. Here, the pump beam is modulated at certain frequency and the pump-induced changes are recorded at this particular frequency. In principle, modulation at certain frequency acts as a band pass filter, by suppressing noise components with other different frequencies. Possible pump modulation units include, mechanical chopping upto a few kHz or electro-optical and acousto-optical modulation with possible modulation frequency even on the order of half the frequency of the laser repetition rate (250 KHz in our case). The measured periodic signal is then multiplied with the modulation function and thereafter integrated. To enhance the sensitivity, the measured signal is integrated with adjustable time constant. The recording of the signal in a lock-in detection can be achieved using commercially available lock-in amplifiers.

Even though the signal to noise is greatly enhanced with this technique, one should keep in mind that the highest signal at the pump modulation frequency is the pump itself. Therefore it is of utmost importance to prevent any scattered pump light from reaching the photo-diode. In addition, electronic components used in the lock-in detection can further contribute to noise. On the other hand, the number of data points and the integration time constant has to be considered carefully to keep the measurement time reasonable. The longer the measurement time larger will be the impact of laser drift on the pump-probe signal. Here, small intrinsic features that could appear in the pump-probe signal can easily be obscured by the noise level because such features can have amplitude in the range of excitation pulse to pulse noise or much smaller.

2.3.2 Fast Scan Technique

In contrast to conventional lock-in detection scheme where the measurement is done in combination with slow scanning speed (with mechanical stage) and low modulation frequency (e.g. mechanical chopping), more advanced and faster measurement technique is adapted for data acquisition in this thesis. This so-called "fast scan" technique has a major advantage in recording a complete photo-induced transient within fractions of a second. Here, we discuss the details of the fast scan technique used for the data acquisition.

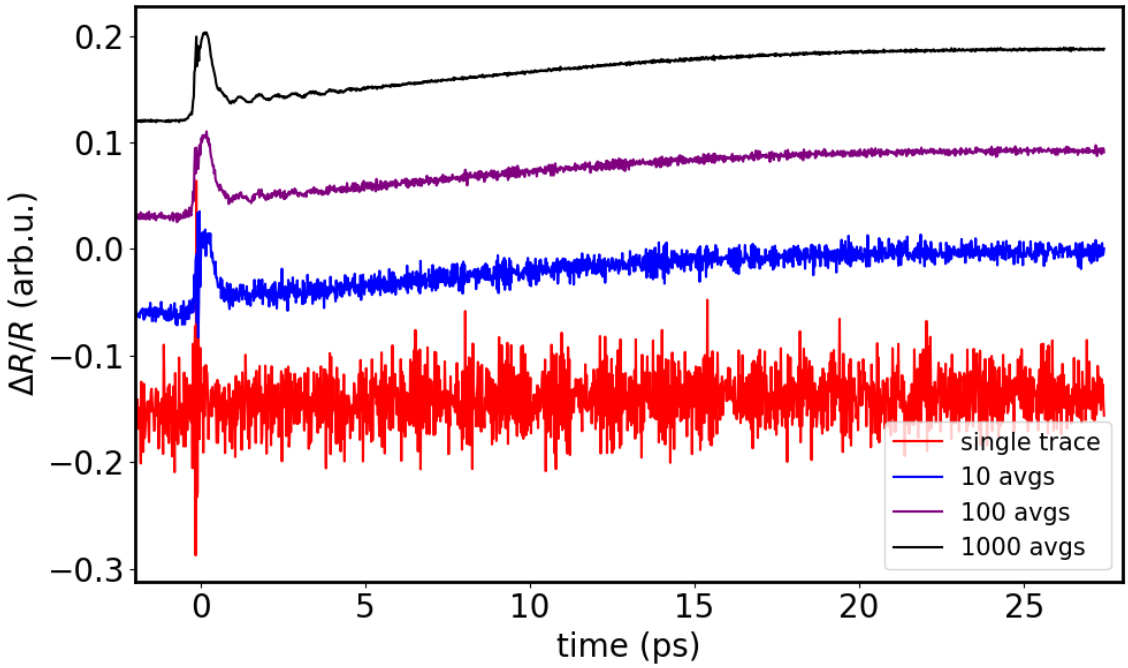

Figure 2.3: Demonstrating the advantage of using fast scan technique. Figure presents the typical traces of photo-induced change in reflectivity recorded using fast-scan pump-probe technique. One complete transient consist of a few thousand data points recorded within few tens of millisecond. By increasing the number of averages (from bottom to top) signal to noise ratio is substantially enhanced resolving the small intrinsic response of the sample (here, oscillatory component) in the pump-probe signal.

Figure 2.4 presents the idea behind the fast scan technique. The fast scan technique incorporates the retroreflector mounted to the drive arm of a translator

powered by periodically (Sinusoidal) driven signal. The shaker/translator can also be made out of a retroreflector mounted on a loudspeaker or can be bought commercially (from e.g. APE [2]). The driving signal of the shaker is generated by a signal generator. Depending on the frequency and amplitude of the shaker, corresponding to the shaker traveling distance, time window can be easily adjusted. Shaker is incorporated in one the beam (the pump or the probe) paths (probe in our case) and the time delay between the pump and the probe (hence the time window) is adjusted. The periodically (sinusoidal) oscillating shaker scans the photo-induced signal twice within one cycle, once on the leading edge and again on the falling edge. Finally, the recorded single transient corresponds to the half the period of the shaker oscillation. In our experimental setup, we incorporate the shaker in the probe arm, so that any misalignment resulting in the sinusoidal background can easily be subtracted using pump modulation unit/reference measurement.

Typical shaker oscillating frequencies are in the range 1-50 Hz. In our experiment, the shaker oscillating frequency, ν is 10 Hz corresponding to period, $T = 100$ ms. A complete transient of 100 ps (depends on the amplitude of the shaker oscillation) is traversed within 50 ms. In addition, to have a better time resolution, the build up of the photo-induced signal (right after time zero- that ensures temporal overlap of the pump-probe beams) is usually kept at the reversal point (either on the leading edge or on the falling edge) of the shaker oscillation. At the turning point of the oscillation shaker moves slower due to the declining velocity of the mirror therefore reducing the time interval between the data points. The build up of the photo-induced signal (time zero) can be moved relative to the phase of the shaker with the help of external mechanical translation stage.

[2] Angewandte Physik & Elektronik GmbH (APE)

Depending on the desired time resolution and the time window, one can easily tune the frequency and amplitude of the shaker. For example, for a time window of 100 ps with a time resolution of approximately 100 fs, photo-induced changes up to the level of 10^{-4} can be achieved in a single shot. Using fast scan technique, few thousands averages of the photo-induced transient can easily be acquired. Indeed, such a technique substantially enhance the signal to noise ratio, where the signal to noise scales with number of averages (N_{avg}) taken, as $1/\sqrt{N_{avg}}$. In addition, this method is not susceptible to long term laser drift. As Laser amplitude fluctuations scale with inverse of the frequency, utilizing fast scan for photo-induced signal minimizes such laser fluctuations.

However, one of the disadvantage of using only a fast scan technique can be seen in the noise spectrum of the measured signal. The shaker has a oscillating frequency of 10 Hz (in our case), in this case the measured noise spectrum is mainly determined by $1/f$ noise that obscure the signal containing small features like coherent oscillations (see Fig.2.3). Now, to overcome such a scenario, one can implement the fast scan in combination with lock-in detection. However, the modulation frequency in this case must be higher than the detection bandwidth in order to achieve a better time resolution. The optimal modulation frequency can be achieved by looking at noise spectrum ($1/f$ noise) at different modulation frequencies. The optimal modulation frequency is found to be half the frequency of the laser repetition rate and is the fastest modulation possible. Due to the high frequency, the modulation can only be achieved using an acousto-optical or electro-optical modulators. Modulation with such a high frequency reduces the noise level and ensures a significant improvement in the signal quality.

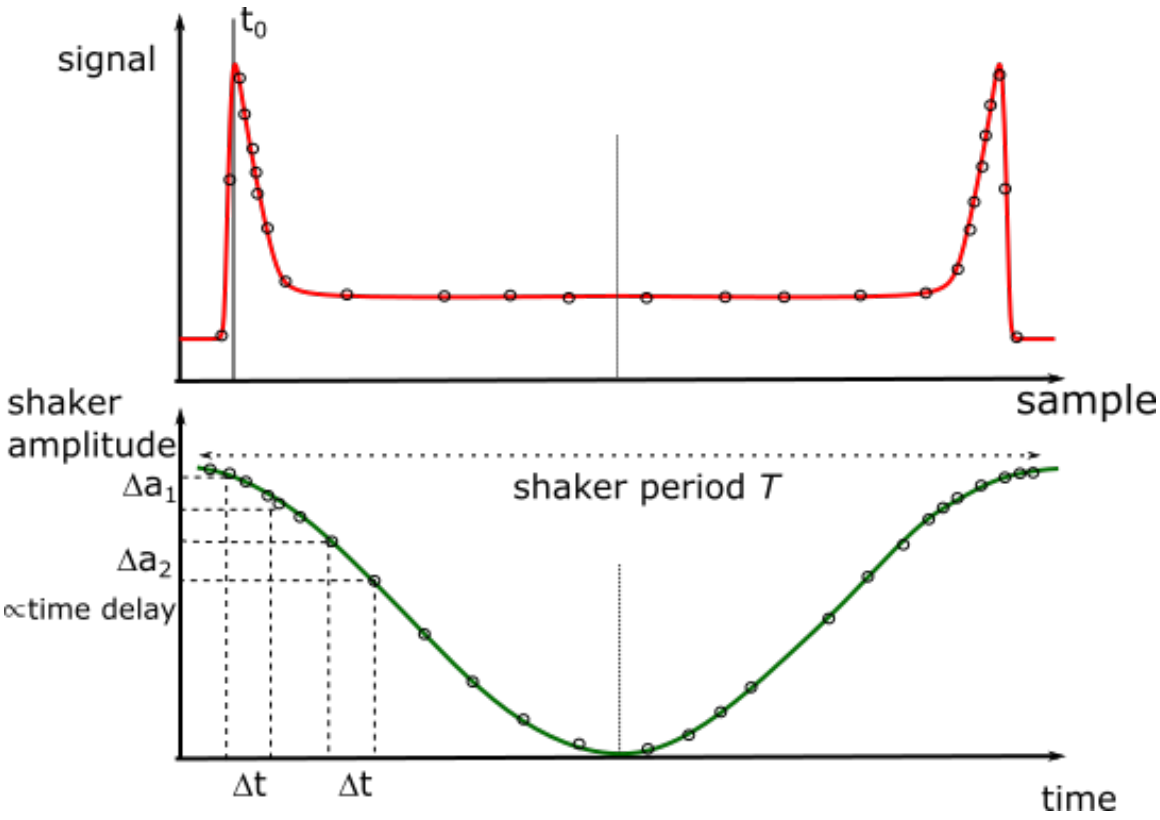

Figure 2.4: Illustration of fast scan technique. Top panel depicts the photo-induced transient recorded one period of the shaker. Lower panel on the other hand shows the shaker oscillation plotted in real time with a shaker frequency of $\nu = 10$ Hz corresponding to the shaker period $T = 100$ ms. The amplitude change Δa_1 for a given time interval Δt is smaller than the amplitude change Δa_2 due to the declining velocity of the mirror at the reversal point of the shaker phase. The time zero t_0 is usually placed at the reversal point of the shaker oscillation due to the declining velocity, therefore more data points withing the smaller time interval and hence the better time resolution. The actual time of the of the experimental time window (time axis) are defined by $\Delta a_x/c$, where c is the speed of light.

2.3.3 Differential Detection

In addition to lock-in detection and fast-scan technique, on of the things that comes into practice is the interferometer type of design and implementation of the difference detection scheme. Here, as shown in Fig.2.2, the probe beam is further split into two - reference and probe beam. The reference arm is slightly

shorter than the probe arm. The optical delay between the probe and the reference is made such that the reference pulse arrives at the sample position substantially before the pump pulse and the probe pulse arrives after/slightly before pump. Recording the response of the sample before pump excitation allows one to have reference measurement. After hitting the sample, the reflected/transmitted probe and reference beam traverse through the same optical components before being split and fed to two coupled photo-diodes. The photo-detector we incorporate is the differential detector, where the response is kept at zero (balancing of the probe and the reference) before pump excitation. After photo excitation with the pump pulse, the measured signal from the photo-detector is proportional to the absolute change in reflection or transmission. In addition, normalizing the change in the photo-induced signal with the unperturbed reference (DC value) beam provides the relative change of the reflection or transmission

$$\frac{I_{sig} - I_{ref}}{I_{ref}} = \frac{\Delta R}{R}, \frac{\Delta T}{T} \tag{2.1}$$

Since the laser system have pulse-to-pulse noise on the order of 10^{-3}, even the perfectly aligned setup will have noise in the photo-induced signal. Thus, incorporating differential detection scheme, substantially reduces such noise in the pump-probe signal. However, implementing differential detection only is not enough to get rid of the noise, as the photo-diode itself is sensitive to other light source that could be present in the laser laboratory. In addition, mechanical vibration of the sensitive optics could induce further fluctuations. To eliminate such noise, one can incorporate modulation techniques, such as lock-in detection or fast scan detection technique or a combination of both. In our experiment,

we incorporate both.

Time Calibration

Final step in the pump-probe setup is the time calibration i.e. converting the real time into the experimental (time delay between the pump and the probe) time. Here, the procedure during time calibration of our pump-probe setup is explained. Time calibration is performed right after finding the spatial and time overlap in the pump-probe setup. This can be easily achieved using e.g. a non-linear crystal in case of degenerate pump-probe. Here, we use Barium-borate, BaB_2O_4 (BBO) which is widely used in time-resolved setups. The idea is, two beams - the pump and the probe- are spatially overlapped in a BBO, and if both beam arrive at the BBO at the same time (delay between two beam is controlled by shaker/delay stage), the sum frequency generation (SHG) occurs and a second harmonic beam with shorter wavelength (400 nm) appears in between two fundamental beams (800 nm). The SHG beam is used to check the pulse duration of our femtosecond laser - known as Autocorrelation.

Now, to perform the time calibration, the autocorrelation pulse can be moved in the measurement time window (measurement time window can be adjusted with the known amplitude of the shaker). The autocorrelation (cross-correlation) pulse can be moved in the measurement window with the help of a computer controlled translation stage with known distance. Figure 2.6**a** presents the autocorrelation traces at different positions with respect to the shaker phase. Conversion of the translation stage travel distance to time delay is known given the step-to-micrometer conversion provided by the translation stage. Fitting the autocorrelation pulse with Lorentzian function allows to extract the centre and FWHM (full width at half maximum) (see Fig. 2.6 **b**). The same fitting proce-

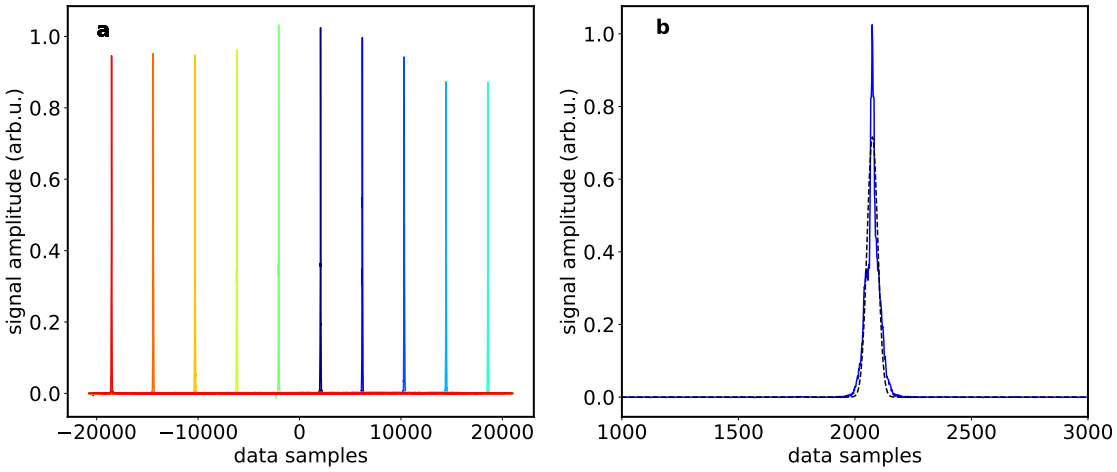

Figure 2.5: Time calibration procedure. **a** autocorrelation pulse at different position with respect to the shaker phase achieved by moving the mechanical translation stage with known distance. **b** fit of the single autocorrelation pulse using a Lorentzian function.

dure is then repeated for all the cross-correlations recorded at different position of the mechanical delay stage. The extracted parameter (central position) from the fit is then plotted against the voltage readout of the shaker instantaneous position. By using a linear fit and extracting the slope of the linear curve one can determine the conversion factor between the shaker voltage readout and thus the time delay between the pump and the probe pulses. The value of the slope extracted from the fit is then used in the data-acquisition software (*Femtoscan*) as a shaker calibration factor.

2.4 Example of a pump-probe study

As described above, pump-probe is a type of a modulation technique, where a pump pulse causes some sort of perturbation of the optical properties of the sample and the decay of this perturbation is mapped out in time by tracking the changes either in transmission or reflection. The pump-probe data allows one to

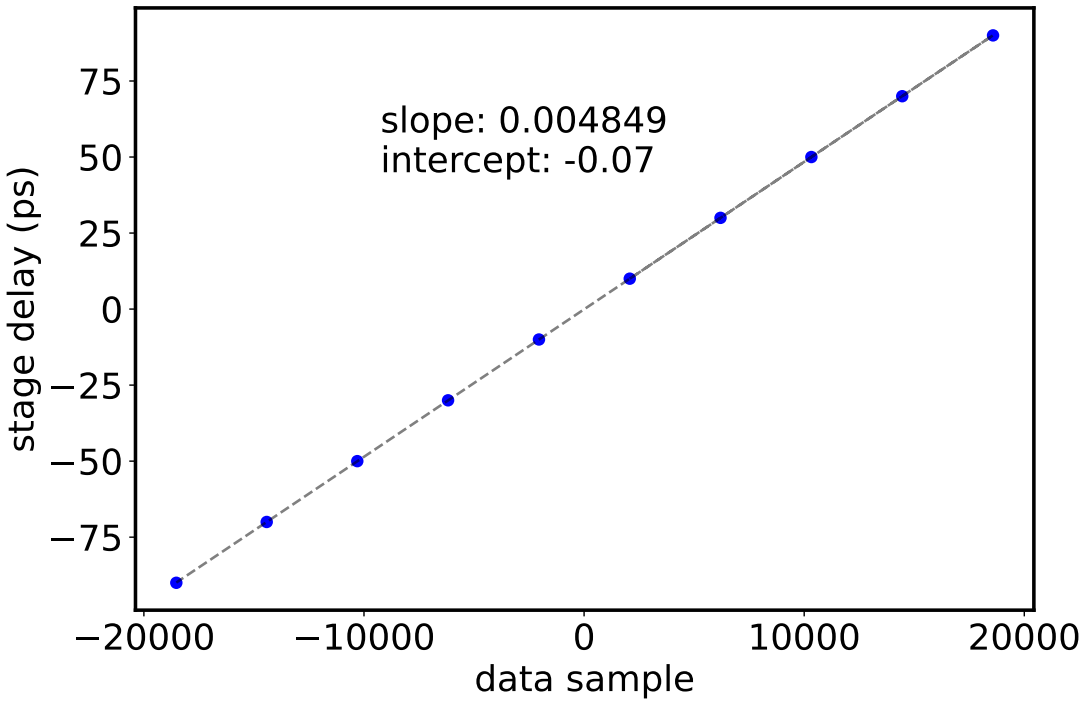

Figure 2.6: Shaker calibration factor.The voltage readout of the instantaneous position of the shaker as a function of central position extracted from the Lorentzian fit (see Fig2.6 **b**). Dotted line is the linear fit with fit parameter (slope and intercept) is given in the inset. The value of the slope is incorporated in the fast-scan software as a shaker calibration factor.

study the physics of excitation and relaxation processes in a material. However, ultrafast phenomena in correlated materials with complicated electronic structure are difficult to understand. Most of the correlated materials are metallic in their normal state but posses various ordering at low temperatures like superconductivity, charge and spin density wave order, and heavy electron behavior. Therefore, understanding the relaxation processes in metal serves as a basis for understanding the relaxation phenomena in correlated materials investigated later in this thesis. Here, we present one of the example of the pump-probe data and present an approach to understand such data. Figure 2.7 presents the photo-induce reflectivity traces extracted with pump-probe technique at dif-

ferent temperatures for $LuAgCu_4$. Following photo-excitation, the reflectivity traces show relaxation on a sub-picosecond timescale. However, the relaxation dynamics display a very weak temperature dependence with change in reflectivity recovering on a sub-ps timescale at all temperatures. The question that arises is how one can understand such relaxation process in materials. Considering only the electron-electron (e-e) and electron-phonon (e-ph) scattering, this can be understood by thermalization of two sub-system (electron and phonon). The intense laser pulse heats up the electronic sub-system, which then termalizes with the lattice sub-system on certain timescale. Indeed, this is observed in regular metals such as Au and Ag [18].

In case of a metallic system, the photo-induced change in reflectivity depends on the occupancy of the states near the Fermi level and thus on the electronic temperature. The optical pump may induce interband transition, exciting the electrons into higher energy states or the pump energy may be absorbed by free carriers. In both cases, the electron gas will have non-thermal distribution immediately after excitation. After photo-excitation, the non-equilibrium electrons scatter via electron-electron scattering. This leads to the rapid thermalization of electron system and the distribution of electrons is characterized by a temperature T_e. The fast scattering process (less than the period of a phonon vibration) in the electronic system leads to a situation where $T_e >> T_l$, where T_l is the lattice temperature. In addition, the heat capacity of the electron system is smaller than that of the lattice, as a result, T_e can rise to very high temperature on the order of several hundred degrees kelvin (K) above the lattice temperature, T_l. This entire process takes place in a time scale of $\approx$ 20 fs, much shorter than the pump pulse width ($\approx$ 50 fs). After optical excitation with pump pulse, we have non-equilibrium situation in the system ($T_e >> T_l$) characterized by two

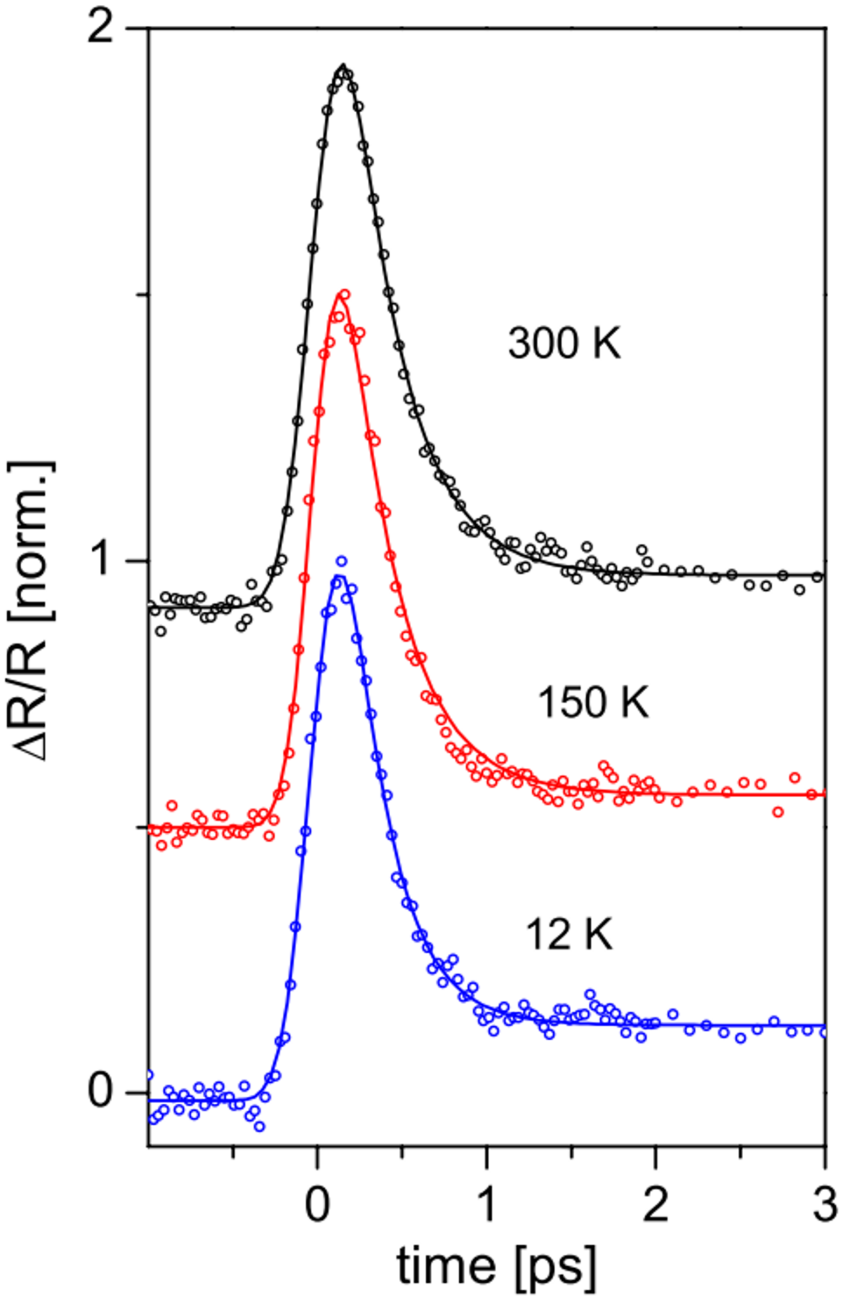

Figure 2.7: Normalized photo-induce change in reflectivity traces on $LuAgCu_4$. The experimental data are presented by the open circles, while the solid lines are fit to the data with single exponential function. Figure adapted from [19].

temperatures, T_e and T_l [20].

Experimentally, the relaxation time(s) of the photo-excited electronic system can be determined by measuring the time dependence of the reflectivity change on a fs to ps timescales [21]. As mentioned above, in a simple approximation one can consider the relaxation process to be governed by the thermalization due to e-e scattering and the relaxation via e-ph scattering. Such a scenario is theoretically explained by the two temperature model (TTM) [22–24]. The model describes the time evolution of the electron (T_e) and lattice (T_l) temperatures. For detail theoretical description of the model reader can refer to the references [18, 19, 22, 24]. The TTM model has been extensively adapted in understanding the relaxation processes in femtosecond thermomodulation experiments [18, 19].

Figure 2.8 presents the results of the TTM simulation of the e-ph thermalization time as a function of temperature compared to the experimental data on metallic $LuAgCu_4$ compound. The model captures the overall trend of the data well down to 50 K and shows divergence at low temperature [19]. The model suggest the decay time should increase as T^{-3} at low temperature, however data do not show this trend. Such absence of divergence at low temperatures was also observed in metals such as Au and Ag [18]. This indicates general failure of the TTM at low temperatures. The disagreement between the experimental observation and the TTM simulation is due to the fact that TTM neglects the e-e thermalization time (model assumes the Fermi-Dirac distribution created instantly after photo-excitation) at low temperatures. At low temperatures the e-e and e-ph thermalization time is comparable, this was indeed shown by simulation of couples Boltzmann equations [25]. Overall agreement between the

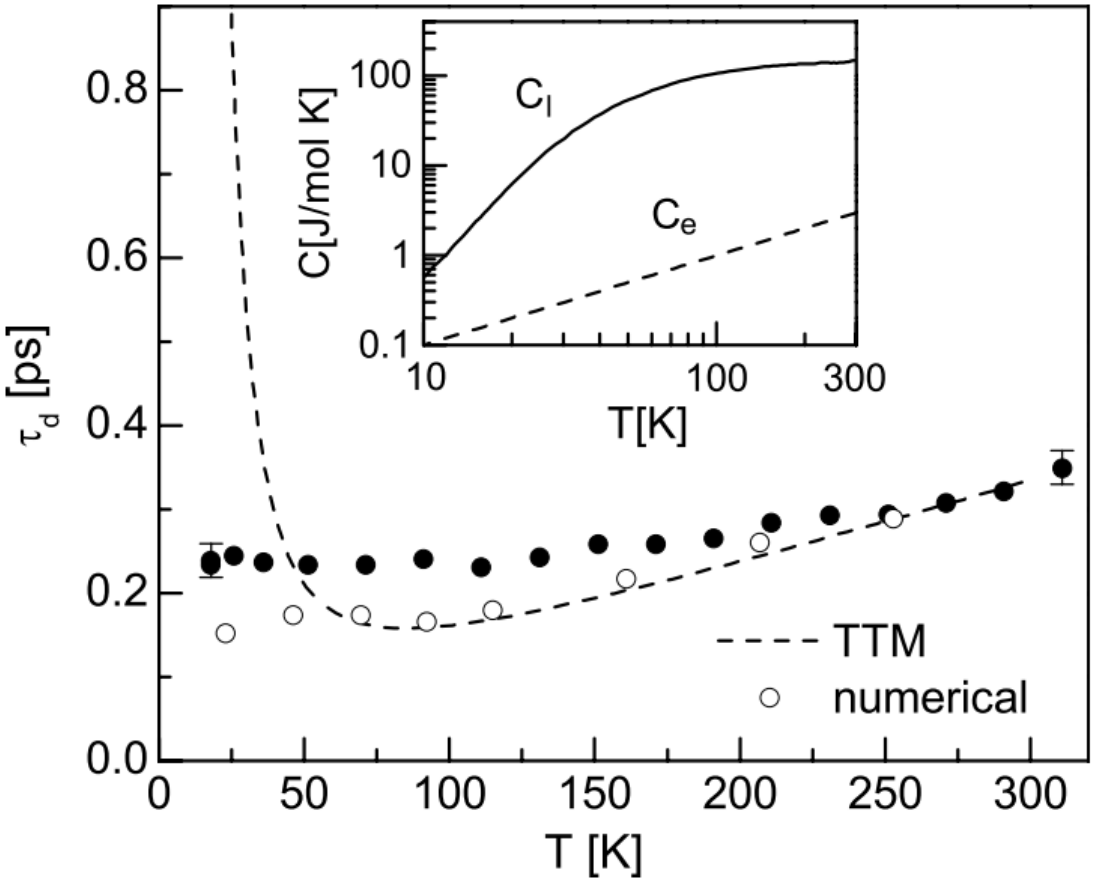

Figure 2.8: Comparison of temperature dependence of the electron-phonon relaxation time of metallic $LuAgCu_4$ compound and the simulation of the TTM model. The solid dots are the experimental data and the dashed line is the TTM simulation. Open circle are the result of the simulation using coupled Boltzmann equations [25]. Insert: electronic and lattice specific heat of $LuAgCu_4$. Figure adapted from [19].

experimental data and the TTM simulation seems to be valid for high temperature (qualitatively), however, the TTM seems to fail at low temperature even in case of simple metals [18, 19, 25]. Furthermore, several observations made in correlated materials (discussed in this thesis) cannot be accounted for by the simple thermomodulation scenario and is discussed in the later chapters.

CHAPTER 3

CARRIER RELAXATION DYNAMICS IN KONDO INSULATOR YbB_{12}

3.1 INTRODUCTION TO HEAVY FERMION SYSTEMS

The history of HFs dates back to 1930's when de Haas *et al.* [26] first found a minimum in electrical resistivity at low temperatures in disordered gold. When decreasing the temperature, after reaching resistivity minimum, the resistivity increased dramatically. Later, dilute magnetic alloys showed similar behavior indicating a connection to the presence of magnetic impurities [27]. Theoretical model for a microscopic understanding of such an anomaly in resistivity was proposed by Kondo in 1960's [28]. The model is based on the microscopic model proposed by Anderson [29] few years earlier. The model explains the observation by the existence of localized magnetic moments and a large on-site Coulomb repulsion leading to an antiferromagnetic exchange interaction with the surrounding conduction sea. Ever since, HFs are widely studied materials in

condensed matter physics as they host different exotic phases ranging from superconductivity to Kondo insulating quantum critical phenomena to Fermi liquid behaviours when crossing different phases. Despite the fact that HFs are widely studied, a complete microscopic understanding of the low temperature behavior in these class of materials is still highly debatable. In this chapter, we will discuss the basic concept behind the HFs and KI and the more recent scientific interest in this material class. We will further present our time resolved spectroscopic measurement on YbB_{12}, one of the prototypical KI. By performing the temperature and fleunce dependence measurement, we study temperature dependence changes in low energy electronic structure and discuss the possible underlying mechanisms. We will introduce the phenomenological model adapted for the data analysis and discuss the temperature dependence in the electronic structure. Most of the results and the discussion work presented in this chapter have been published and are adapted from the Ref. [30].

3.2 Properties and concept of Heavy Fermion and Kondo Insulator

Primarily, Heavy Fermions (HFs) are intermetallic compounds in which one of the constituents is a rare earth or actinide ion with partially filled 4*f*- or 5*f* - electron shells. HFs fall in the category of strongly correlated materials where the correlations result from the strong local interaction of the partially filled *f* shells [31]. They present one of the most challenging classes of materials as they host different electronic, magnetic and thermodynamic phases at low temperatures [32–34], giving rise to the new ground state in the electronic system. Some of the best known examples include - Ce based compounds $CeAl_3$,

$CeCu_2Si_2$, $CeRu_2Si_2$, $CeCu_6$ and the U-based systems UBe_{13} and UPt_3. At high temperature, HFs behave like ordinary metals with magnetic rare-earth or actinide systems having non-interacting itinerant conduction electrons and well localized f moments and the magnetic susceptibility is characterized by a Curie-Weiss dependence $\chi = M^2/3T$ with M being the magnetic moment of an f state [35]. As the temperature is lowered below the material specific Kondo temperature (T_K), the localized magnetic moments residing in the sea of conduction (c) electrons hybridized with them. In other words, at low temperature, the f electrons couple strongly with conduction electrons forming a narrow resonance in the density of states near the Fermi level. As a result, HFs behave like a system of heavy itinerant electrons with large effective mass m^* [36]. The effective mass (m^*), typically 1000- times larger than the bare electron mass. Such a $c-f$ hybridization results in the formation of indirect hybridization gap in the Density of States (DOS) (see fig3.1). Other remarkable properties of the HFs include the linear dependence of specific heat with temperature $i.e. C = \gamma T$, with (γ being of the order of $J/MolK^2$, several order of magnitude larger than those of ordinary metal, large T^2 term in electrical resistivity at low temperature, the magnetic susceptibility, χ, approaching the Pauli like form and becoming temperature independent [31].

Kondo Insulators (KI), on the other hand, are the class of heavy fermion system, whose properties are governed by the presence of an energy gap below T_K. While in metallic heavy fermion systems the Fermi level (or chemical potential) lies in one of the flat $c-f$ hybridized bands, in KI the Fermi level lies within the indirect hybridization gap. One of the measure consequence of the $c-f$ hybridization, in simple approximation, is the formation of the renormalized band with upper $E_1(K)$ and lower $E_2(K)$ band, which have both f and conduc-

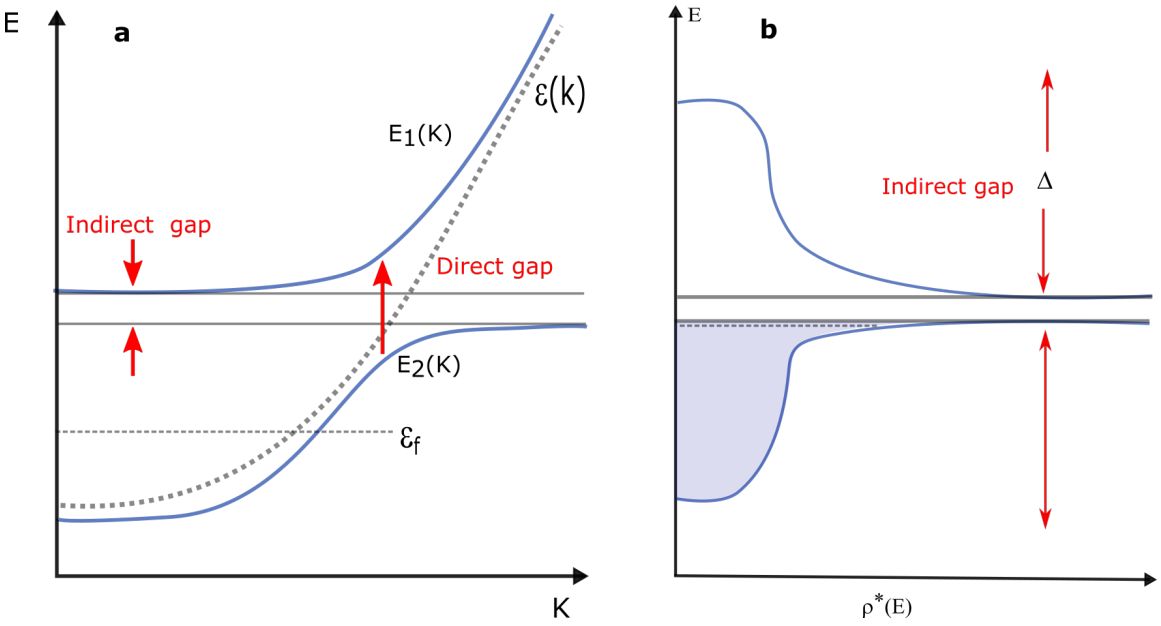

Figure 3.1: (a) Schematic band picture of the hybridized bands of the Kondo lattice system. ε_f and $\varepsilon(k)$ represent the unhybridized f and the conduction band respectively. $c-f$ hybridization leads to the formation of upper, $E_1(k)$ and lower, $E_2(k)$ bands giving rise to the direct and indirect gap. (b) Renormalized density of states demonstrating the presence of indirect hybridization gap close to the Fermi level. In case of HFs, the Fermi level lies in one of the flat $c-f$ hybridized band, while in KI, the Fermi level lies within the indirect hybridization gap. The figure is redrawn with the idea from [37] and adapted from [35] .

tion band character (see Fig. 3.1). They exhibit an indirect hybridization gap of width $\Delta = T_K$ [37]. On cooling below T_K, inter-site correlations of localized f magnetic moments arranged in a dense periodic array of Kondo lattice, mediated by the conduction electrons can give rise to a magnetic long range order. This impurity-impurity correlation mediated by RKKY interaction [38–40] favors the indirect exchange coupling between neighbouring local moments and play an important role in understanding the ground state of the material. For a broad spectrum on the concepts of HFs and KI, the readers can refer to the references [29, 31, 35–37, 41].

3.3 Kondo Insulator YbB_{12}

YbB_{12} is one of the best-known Kondo insulators with an indirect hybridization gap, E_g, on the order of 10 meV. Optical conductivity measurements [42] reveal a crossover from metallic behaviour at high temperatures to insulating behaviour at low temperatures with suppression of the free carrier response below 80 K. The data suggest the hybridization gap to fully open below $\sim$ 20 K, with $E_g \sim 20$ meV [42]. Similar values for the low temperature gap were extracted also from high resolution photoemission spectroscopy data (PES) [43, 44], while transport measurements suggest a low temperature gap of $\sim$ 13 meV [45]. Interestingly, a combined PES and time-resolved-PES study [46] suggests the gap closing only at temperatures above 100 K. The presence of a gap at low temperatures has been unambiguously confirmed by many thermodynamic experiments and are interpreted with single impurity model or Kondo-lattice model. The temperature dependence of the gap, or more explicitly, is the gap always present even at $T > \Delta$, is still an open question.

Recently, YbB_{12} has further gained on scientific interest as a candidate for hosting a non-trivial topological surface state, driven by strong electron correlations and strong spin-orbit coupling. Indeed, recent experimental observation of quantum oscillation in electrical transport and magnetic-torque measurements [47] seem to support the idea of a non-trivial topological surface state. Despite tremendous theoretical efforts, suggesting the existence of fermionic charge neutral excitations [48], Majorana fermions [49] and strong correlation effects [50], the physics governing such unusual behaviour remains unclear.

The low energy electronic structure of heavy electron systems were studied earlier using femtosecond real-time spectroscopic methods. Here, femtosecond

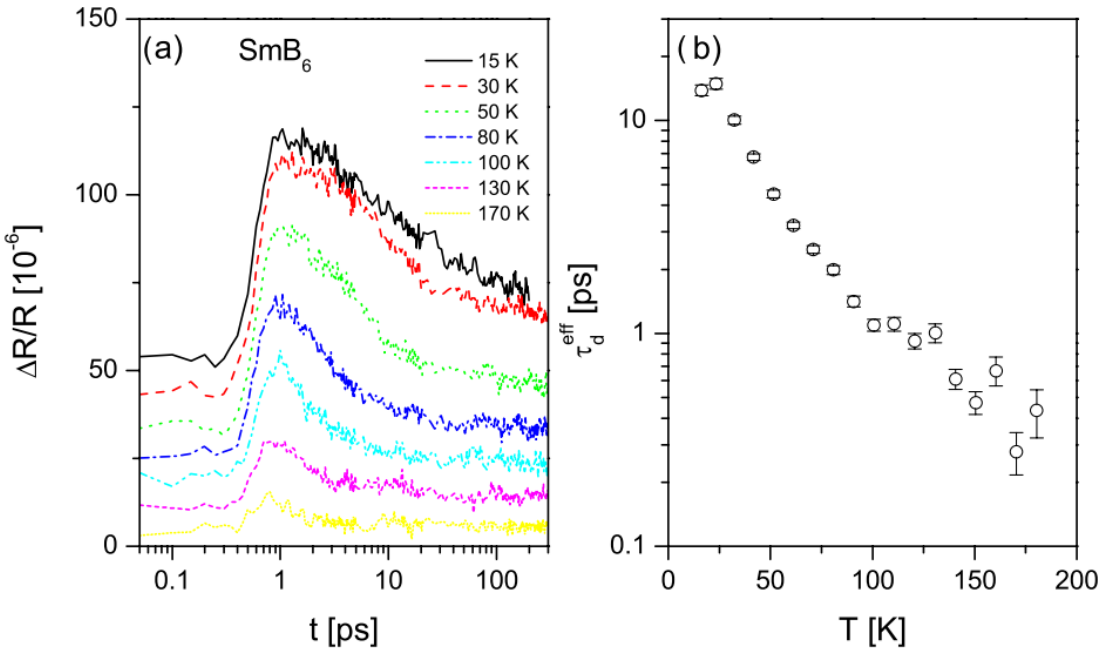

Figure 3.2: (a) Temperature dependence of the photo-induced reflectivity dynamics of KI SmB_6. (b) The temperature dependence of the relaxation time (τ_d^{eff}). The figure is adapted from [19]

time-resolved studies on a series of heavy fermion systems [19, 51–55] as well as on the Kondo insulator SmB_6 [19, 52, 56] were performed. These studies have shown the lifetimes of photo-excited carriers to be highly sensitive to the presence of the hybridization gap. Figure 3.2 presents the earlier study on one of the Kondo insulating material SmB_6. Here, the photo-induced reflectivity change is found to be non-exponential. The carrier relaxation dynamics is found to be governed by the presence of hybridization gap and increases by nearly two order of magnitude upon lowering the temperature. The similar observation was made also in other HFs [19, 51–55] Time-resolved measurement on KI and HFs, particularly, the relaxation dynamics of quasiparticles, coupled to phonons with frequency larger than the energy of the indirect hybridization gap, were accounted for by the phenomenological Rothwarf-Taylor bottleneck model (elaborated in

Section 3.5) [57–61]. The model, originally developed to describe the relaxation dynamics in photo-excited superconductors, was surprisingly able to account for the dynamics in both, metallic heavy fermions and Kondo insulators [19, 52]. In addition to transient reflectivity studies, the dynamics of Kondo insulators was recently probed also by tr-PES [46] and transient THz spectroscopy [56]. Here, tr-PES study on YbB_{12} [46] demonstrated that the recombination of carriers at low temperatures proceeds on a 100 ps timescale, consistent with observations on SmB_6[52]. The temperature dependence of the dynamics suggested the gap to have a weak temperature dependence and to affect the relaxation dynamics up to at least about 100 K. Studies of THz dynamics in SmB_6 revealed similar nearly temperature-independent gap at temperature above 20 K [56]. However, the analysis of the temperature dependence of the thermally excited density of quasiparticles (QPs), extracted from the quantitative data analysis using the bottleneck model [58], suggested additional changes in the electronic structure below $\sim$ 20 K. Together with the observation of a rapid changes in the free carrier response it was argued that another relaxation channel was opening up at low temperatures, which was attributed to the onset of the surface state [56].

3.4 Time resolved study on YbB_{12}

Following up the recent tr-PES study [46] demonstrating the recombination of carriers at low temperature proceeding on a 100 ps timescale being governed by the indirect hybridization gap, we study the carrier relaxation dynamics in the Kondo system YbB_{12} using femtosecond time-resolved optical spectroscopy (technique described in chapter 2). Because of the higher dynamic range of an all-optical approach [62], we can track the carrier relaxation dynamics in KI and by analysing the experimental data within the model, we can obtain the

information on the nature of the hybridization gap, its temperature dependence and gain on complementary knowledge on the low energy electronic structure.

To this end, we explore in detail the temperature and excitation density dependence of carrier relaxation dynamics in YbB_{12}. In order to account for the experimental observations, phenomenological model has been proposed (see Section 3.5).

3.4.1 T-dependence of carrier relaxation dynamics on YbB_{12}

Temperature dependence photo-induced reflectivity measurements are performed to study the carrier relaxation dynamics. The sample under study is a single crystals of YbB_{12} grown by the travelling solvent floating zone methods [45]. A disk-shaped sample 4.5 mm in diameter was cut from the crystal, and mechanically polished for optical measurements [42]. Transient reflectivity traces are recorded using 60 femtosecond (fs) NIR optical pulses, utilizing an amplified Ti:sapphire laser amplifier operating at 250 kHz. Figure 3.3 presents the photo-induced reflectivity traces recorded at several temperatures between 5 and 290 K at a constant fluence (F) of 8 μJ/cm^2. The excitation fluence can be obtained with: $F = P/(f.\pi/4.\sigma^2_{FWHM})$, here, P denotes the averaged power, f is the repetition rate of the laser and σ^2_{FWHM} is the full width at half maximum of the Gaussian beam profile inside the sample. The choice of the low excitation fluence is based on the goal to study the temperature dependence dynamics in the low perturbation limit where the dependence on fluence is still linear.

From Fig. 3.3(a) one can clearly see a strong temperature dependence of the recovery time, which varies between several tens of ps at 5 K to about 1 ps at

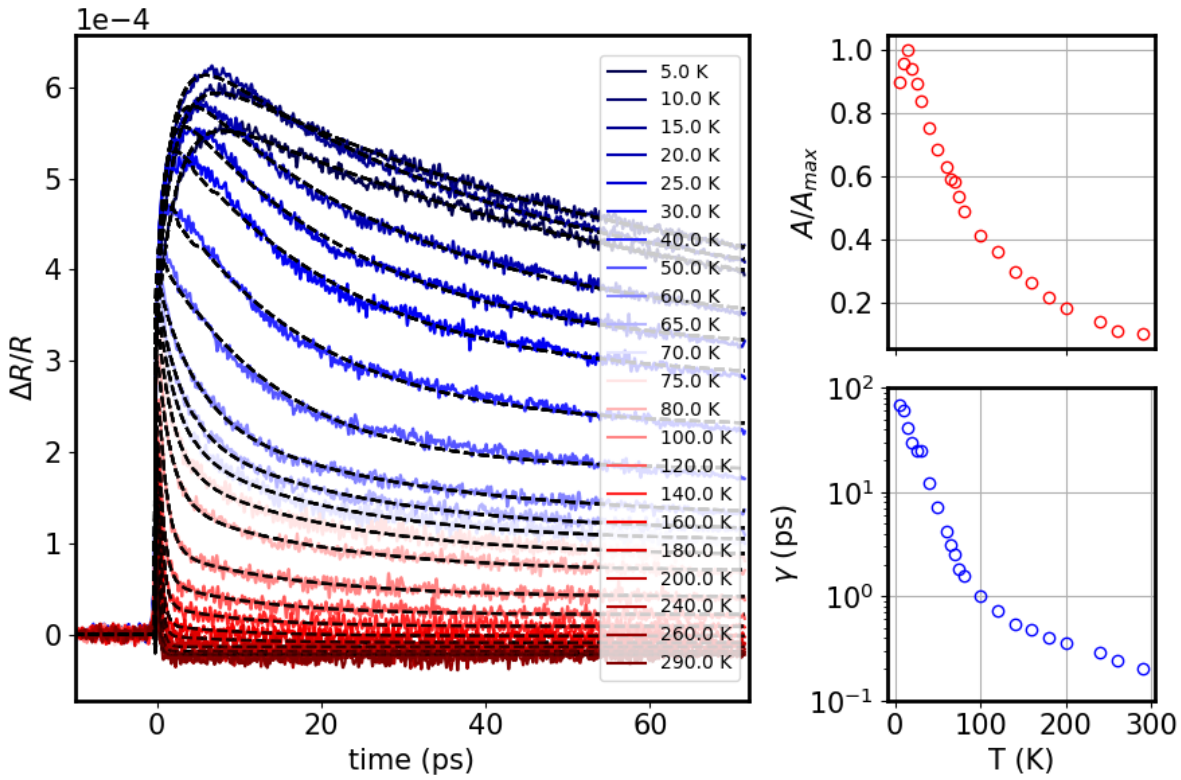

Figure 3.3: (color online): Dynamics of photo-induced change in reflectivity of YbB_{12} single crystal at 800 nm. (a) Temperature dependence of reflectivity traces recorded at a constant fluence of 8 $\mu J/cm^2$. Dashed lines are fits to the data (see text). (b) Photo-induced change in amplitude (A) of the reflectivity traces recorded at several temperatures between 5 and 300 K. The values are normalized to maximum change in amplitude (A_{max}). (c) Recovery dynamics at selected temperatures extracted from fitting the reflectivity data at panel (a).

80 K. Moreover, the data at T $\leq$ 40 K display a slow picosecond rise-time, which was not observed before in any Kondo insulators (for example see another prototypical kondo system, SmB_6 [52] and Fig. 3.2) but is commonly observed in superconductors with a small energy gap [59–61]. As elaborated later, when addressing the excitation density dependence, the long risetime can be attributed to electron-hole pair creation by absorption of high-frequency phonons, created during the initial relaxation of hot carriers towards the hybridization gap edge.

To address the temperature dependence of the amplitude and the recovery time we first fit the photo-induced reflectivity traces with the following fit function:

$$\frac{\Delta R}{R}(t) = H(t)\left[A\left(1-e^{-\frac{t}{t_{rise}}}\right) . e^{-\gamma t} + B\right] \tag{3.1}$$

Here, H(t) is the Heaviside step function with resolution limited rise time of $\sim$ 100 fs. A, t_{rise} and γ are the amplitude, rise time and the decay rate of the transient reflectivity, respectively. B corresponds to a remaining signal at long time-delays, attributed to a bolometric signal (decay of which is governed by heat diffusion). This simple model fits the data well for T< 60 K, while at higher temperatures the recovery is better accounted for by a double exponential decay. One should note that, this is the simplest model that accounts the data quite well to study the carrier relaxation dynamics in all-optical experiments. As discussed in 2, TTM model used to understand the dynamics in simple metals fails to account for the observations made at low temperatures.

Figure 3.3 (b) and (c) presents the amplitude (A) and the recovery time of the reflectivity traces extracted from the fit using equation 3.1. Figure 3.3(b) presents the temperature dependence of A, taking simply maximum values of reflectivity transients presented in Figure 3.3 (a). Upon lowering the temperature, the amplitude displays a continuous growth down to $\approx$ 20 K. Below 20 K, however, A does not saturate, but displays a slight decrease - similarly as in SmB_6 [56] indicating additional modification in low energy electronic structure. Figure 3.3 (c) shows the overall decrease of the relaxation time of the photo-excited carriers with decrease in temperature. The relaxation persist tens of picosecond at low temperature to few picosecond at high temperature. The overall slowing down of the relaxation upon lowering the temperature was previously interpreted as an indication of the presence of an energy gap in the excitation

spectrum. Such behavior was observed both in superconductors [58–61] as well as in heavy electron systems[19, 51, 52, 54, 56], and was attributed to a boson (phonon) bottleneck[19, 58]. Here, after photo-excitation, hot electrons relax via e-e and e-ph collision processes leading to the formation of excess densities of QPs (or electron-hole pairs) and high frequency ($\hbar\omega > E_g$) phonons (HFP). The presence of gap hinders the relaxation of the photo-excited carriers due to the competing creation of QPs by HFP absorption, resulting in a so-called phonon bottleneck. Here, the slow decay of the HFP population (via anharmonic decay or via diffusion out of the excitation volume) determines the relaxation of the coupled EHP-HFP system back to equilibrium (see Fig. 3.5).

3.4.2 Excitation fluence dependence study

The temperature dependence study shows an indication of presence of energy gap as the temperature is lowered below characteristic temperature of $\approx$ 100 K. Next thing would be to check, if there is an energy gap, how robust is it against external optical perturbation. To this end, we performed excitation fluence dependence study on YbB_{12} at low temperature (5 K). Indeed, our measurement shows the dramatic dependence of the reflectivity change and the relaxation rate on the excitation fluence (see subsection 3.5.2).

Figure 3.4 presents the fluence dependence reflectivity transients recorded at 5 K. The excitation fluence is varied over three orders of magnitude from 0.5 $\mu J/cm^2$ to 820 $\mu J/cm^2$. The reflectivity traces are normalized to fluence (F) to emphasise the non-linearity of the response at higher F. For low excitation fluences, up to F $\sim$ 20 μJ/cm^2, the excitation density dependence data do display slightly sub-linear dependence of amplitude on fluence, yet the characteristic timescales remain constant. For higher fluences, however, both the amplitudes

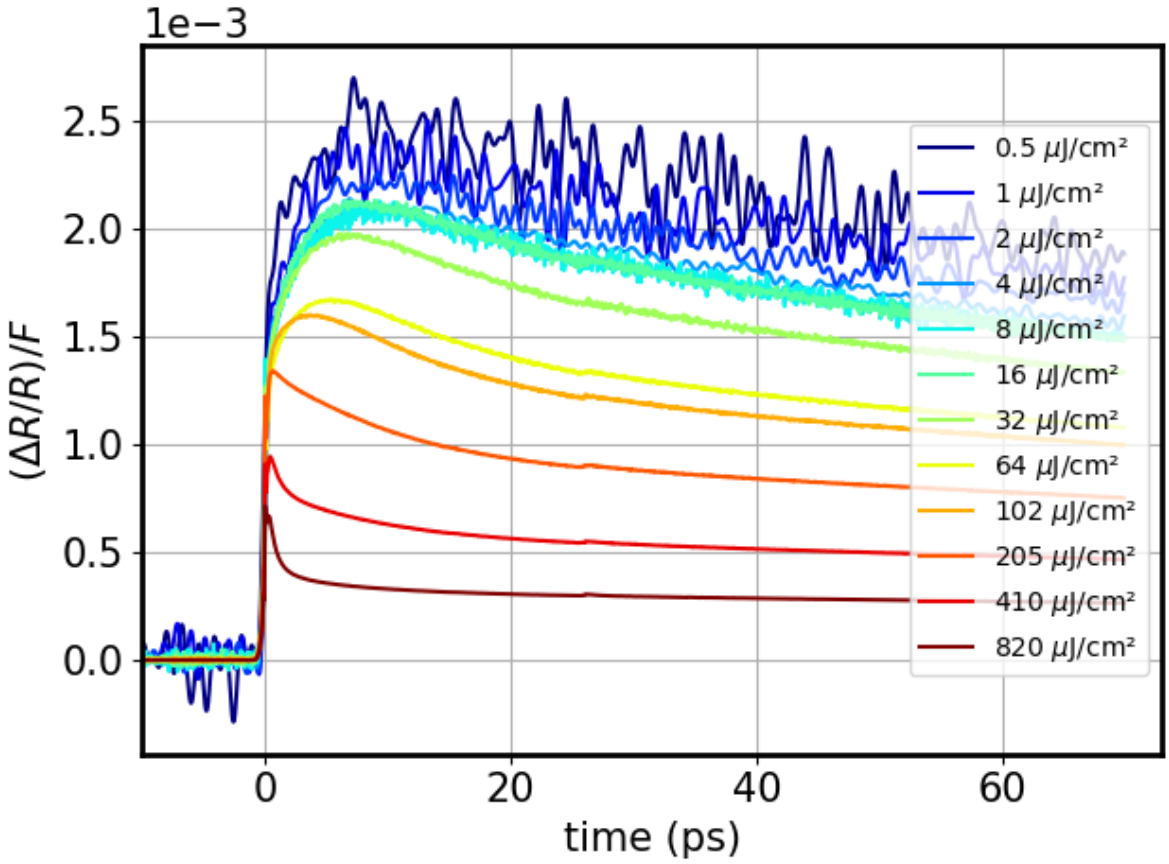

Figure 3.4: (color online): Dynamics of photo-induced change in reflectivity of YbB_{12} single crystal recorded for excitation fluences spanning over three orders of magnitude. Note that the data are normalized to the corresponding excitation fluence to emphasize the observed nonlinearity.

as well as the characteristic timescales show a quite dramatic dependence on F. The relaxation rate changes on a multi-ps timescale becomes slower with the decrease in fluence. The relaxation rate changes over two order of magnitude over the fluence range used. In addition to the relaxation rate, we observed long build-up times of photo-excited carriers. The instantaneous build-up of photo-excited carrier ($\approx$ 100 fs) followed by delayed rise on a ps timescale. This slow rise time gradually decreases with increased excitation density and finally becomes resolution limited above $F = 102\ \mu J/cm^2$.

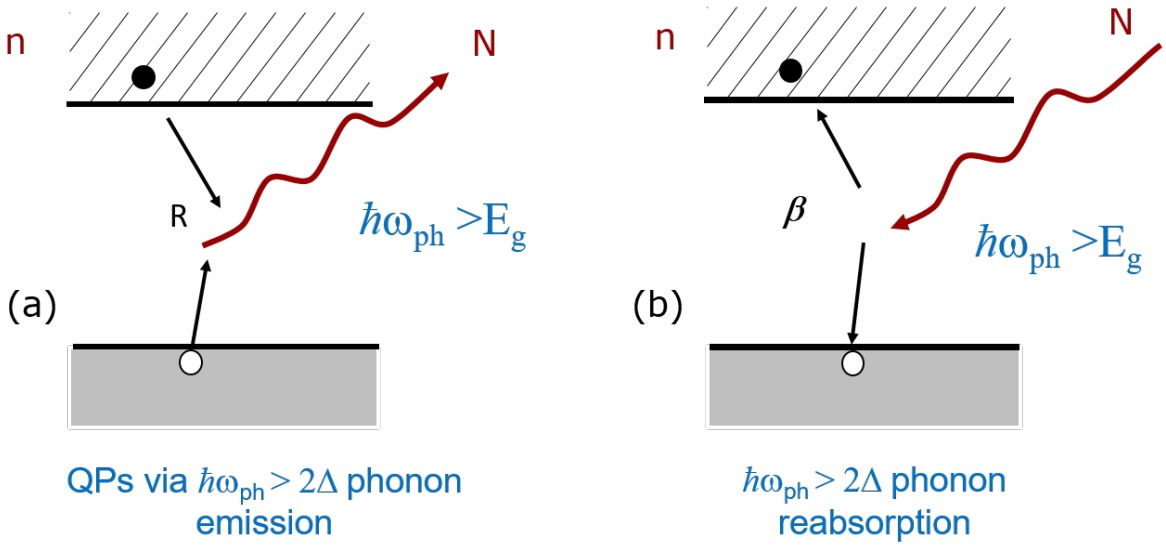

Figure 3.5: Schematic of the carrier relaxation processes in a narrow band gap semiconductor considering the phonon bottleneck. (a) Presents the bare recombination of the electron-hole pair through the creation of a high frequency phonon. Following photo-excitation, the EHPs recombine with releasing energy to the HFPs (2Δ phonons where $Delta$ being the energy gap). The bare recombination of the EHPs is given by the microscopic parameter R, (b) creation of an electron-hole pair by re-absorption of a high frequency phonon. When the HFPs start to decay, EHPs are created due to re-absorption process of the HFPs. The probability of EHPs creation by HFPs absorption is defined by the microscopic parameter β. Figure is adapted and redrawn from [19].

3.5 Data Analysis

In the following we make use of the phonon bottleneck model [52, 58] for a quantitative analysis of the experimental data to gain information on the temperature dependence of the low energy gap in YbB_{12}. Before discussing the analysis of the data, we first review the RT model and it's solution (necessary for interpreting our experimental data) using the language appropriate for narrow gap semiconductor. The model has been extensively used to understand the temperature and fleunce dependence studies on several HFs [19, 51–55] and KI [19, 52, 56].

Figure 3.5 presents the scenario for relaxation of photo-excited narrow band semiconductor. Similar to superconductors, immediately after the photo-excitation, highly energetic electrons initially release their energy by e-e and e-ph collision process (Fig. 3.5 a). Following the process, the system is characterised by excess densities of EHPs and HFPs. When EHPs with energy greater than the 2Δ recombines, a high frequency phonon is created with an energy (E) $> E_g$ (see figure 3.5 (a)). Since the HFPs can further excite EHPs (figure 3.5 (b)), the recovery dynamics of the EHPs is actually governed by the decay of the HFPs population. Following photo-excitation, the model assumes that the absorbed energy is initially (on the 100 fs timescale) distributed between EHPs and HFPs while the dynamics of the EHPs and HFPs densities governed by a set of two coupled differential equations [58]:

$$\frac{dn}{dt} = \beta N - Rn^2 + n_0\delta(t) \tag{3.2}$$

$$\frac{dN}{dt} = -\frac{1}{2}\left[\beta N - Rn^2\right] - \frac{(N-N_0)}{\tau_\gamma} + N_0\delta(t) \tag{3.3}$$

Here, n and N are the electrons/holes and HFPs densities, respectively, β is the probability of electron-hole pair creation by HFPs absorption, and R the bare EHPs recombination rate with creation of HFPs. n_0 and N_0 are the initial densities of EHPs and HFPs created after photo-excitation and the initial avalanche process (on a 100-fs timescale). Considering a phonon bottleneck scenario, the initial (before HFPs decay) thermalization between EHPs and HFPs will result in a quasi-equilibrium state, given by the detailed balance equation, $Rn_s^2 = \beta N_s$, where, n_s and N_s are the quasi-thermal concentrations of EHPs and HFPs at some new effective temperature T^+[63].

Assuming that no energy is yet transferred to phonons with energy smaller

than the gap energy this quasi-stationary case is given by

$$Rn_s^2 = \beta N_s \; ; n_s = \frac{\beta}{4R}\left[\sqrt{1+\frac{8R\,(2n_0+N_0)}{\beta}} - 1\right]. \tag{3.4}$$

As noted above, once this quasi-equilibrium state has been reached, the coupled systems relaxes through the decay of HFPs (e.g. via diffusion out of the probed volume or anharmonic decay).

3.5.1 T-DEPENDENCE ANALYSIS

We now focus on the temperature dependence of the amplitude of the reflectivity transient and its relaxation rate. In the weak perturbation case, the amplitude or reflectivity change, A, is assumed to be proportional to the photo-excited EHPs density. In other words, $A \propto (n_s - n_T)$, where n_T is the density of thermally excited EHPs before photo-excitation. With this, and taking into the account the detailed balance equation, Eq.(3.4), it has been shown [52, 58], that the magnitude and the temperature dependence of the gap (or pseudogap) can be extracted from the temperature dependence of A in the weak perturbation limit. In particular, it follows that the temperature dependence of the reflectivity amplitude, A is governed by the temperature dependence of n_T [19, 58]:

$$n_T\,(T) \propto \frac{A(0)}{A(T)} - 1, \tag{3.5}$$

where $A(T)$ is the amplitude of the transient at the base temperature T and $A(0)$ is the amplitude in the limit when $T \to 0$ K. Since, $n_T\,(T) \propto \left(E_g T\right)^p e^{-E_g/2k_B T}$ [19], where power p depends on the exact shape of the density of states, the extracted n_T allows us to estimate the gap magnitude and its temperature dependence.

Moreover, the initial recovery rate γ has also been shown to depend on n_T in the low excitation density limit and is given by [19]

$$\gamma \propto [D(En_T + 1)^{-1} + 2n_T] \tag{3.6}$$

with D and E being temperature independent proportionality constants.

Figure 3.6a presents $n_T(T)$, extracted through Eq.(3.5), where the maximum amplitude recorded at 20 K was used as *A(0)*. Above 20 K, we fit the extracted $n_T(T)$ with $n_T(T) \propto \left(E_g T\right)^p e^{-E_g/2k_B T}$. We use $p = 1/2$, which corresponds to the variation in the density of states near the gap edge, similar to a superconductor (the fit is rather insensitive to small variations in p). The continuous increase of n_T with increasing temperature suggest that the hybridization gap (or pseudogap) is present up to room temperature. We further consider E_g to be temperature independent in the temperature range in question (T < 200 K). Our observation is in-line with earlier tr-ARPES study [46], where the hybridization gap is argued to be present up to 110 K. We did consider different temperature dependence of E_g, similar to those observed in $Ce_3Bi_4Pt_3$ [33, 64], yet no major improvement in the fit quality has been achieved. The extracted values for E_g (see Figure 3.6a) are around 15 meV, consistent with earlier spectroscopic studies [19, 51–55].

Note that, a decrease in amplitude below 20 K (see Figure 3.3b), which is reproduced by several measurements on different days, could be interpreted by an increase in n_T (see Figure 3.6a) as a result of lowering of the characteristic gap energy scale (for example due to in-gap states). On the other hand, at these low temperatures the density of thermally excited EHPs becomes low compared to the density of photo-excited EHPs. Therefore, in the limit of $n_s >> n_T$, a

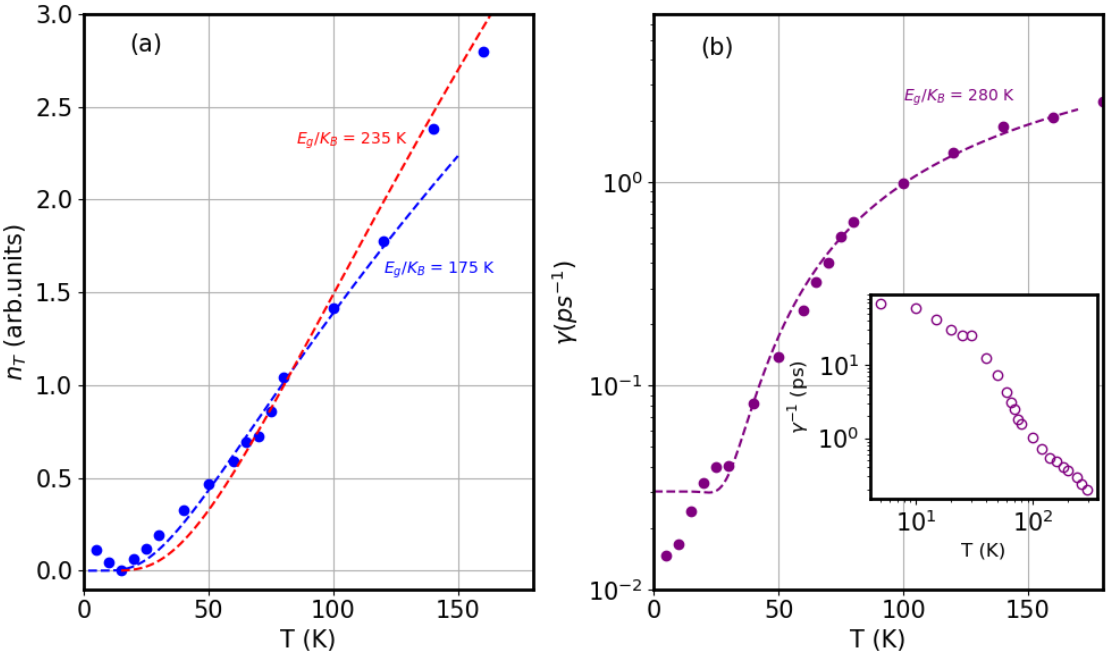

Figure 3.6: (color online): Temperature dependence of (a) thermally excited EHPs density extracted from the temperature dependence of amplitude presented in the figure 3.3a, and (b) the initial relaxation rate. The data were recorded at constant fluence of 8 $\mu J/cm^2$. The solid spheres are the experimental data and the dotted lines are the fit to the data (see text)

decrease in the signal is more likely caused by a (slight) increase in the characteristic gap energy scale, or sharpening of peaks in the density of states, as suggested by recent tunneling studies of SmB_6 [65].

The temperature dependence of the decay rate, γ, further supports the later scenario. As shown in Figure 3.6b, γ continuous to increase up to highest temperatures used in this study. Fitting the data with Eq.(3.6), using the same functional form for n_T, we obtain somewhat higher value for E_g = 23 meV (E_g/k_B = 280 K). Note, that also in this case, at low temperatures there seems to be a departure from the high temperature behavior, consistent with changes in the low energy structure below 20 K. Given the simple approximations for the shape of the den-

sity of states and assuming the gap to be simply temperature independent, the overall agreement of the model to our experimental data is very good.

Our observation of departure from constant gap behavior below 20 K implies changes in the low energy excitation spectrum near 20 K. We note that in SmB_6 similar departure from the high temperature behavior was observed at low temperatures [56]. Together with the observed large residual THz conductivity, such observation was in SmB_6 attributed to a (topological) surface state. In YbB_{12}, however, the residual THz optical conductivity is (below 20 K) at least two orders of magnitude lower than in SmB_6 [42, 66]. Thus we exclude this possibility. We argue that correlations arising from the lattice effect of the local moments give rise to changes in the low energy excitation spectra, resulting in a departure from the single-ion Kondo behavior.

3.5.2 Analysis of the F-dependence data

As pointed above, the temperature dependent study suggests the hybridization to be present nearly up to room temperature. At room temperature the relaxation dynamics becomes as fast as the e-ph thermalization in a metallic state, thus it is hard to distinguish between the dynamics as a result of a relaxation bottleneck or dynamics in a gapless metal. The question is, how robust is the gap with respect to electronic excitation, triggered by an optical pulse. Moreover, the peculiar behavior with a finite temperature and excitation density dependent, rise-time, needs to be addressed (see Figure 3.3a and 3.4). As shown in Fig. 3.4 at low enough temperatures, the instantaneous build-up of photo-excited carrier density on a $\sim$ 100 fs timescale is followed by a further increase on a ps timescale. The rise-time of this delayed response gradually decreases with increasing excitation density and finally becomes resolution limited for $F > 100$

$\mu J/cm^2$.

Such an observation of the delayed rise has not been made on Kondo insulators so far. However, similar behavior has been reported in superconductors [59, 60, 67], where the delayed rise has been attributed to additional Cooper pair-breaking by absorption of high frequency bosons (phonons in case of conventional superconductors). These HFPs, created during the initial e-ph relaxation of hot carriers towards the gap edge, further break Cooper pairs until the quasi-equilibrium (quasi-thermal state) between the condensate, quasiparticles and HFPs is reached (see Eq.3.4). This, so-called, pre-bottleneck dynamics [57, 58] has been used to determine the e-ph coupling constant in a conventional superconductor NbN [60]. In analogy to superconductors, the dynamics in a Kondo insulator, where the Fermi level (E_F) lies within the well-established (indirect) hybridization gap, can be treated using the same approach (see Fig.3.5). Importantly, the nonlinear dynamics in superconductors is limited to excitation densities, for which the gap is not dramatically suppressed after photo-excitation. Thus, such study provides means to quantitatively analyze the robustness of the hybridization gap against photo-excitation and to obtain information on the electron-phonon coupling.

Simulation of pre-bottlencek dynamics

To address the delayed rise time dynamics, we first focus on the simulation of the dynamics of the effective carrier density considering various limiting cases to compare with our experimental results. Detailed discussion of the analytical solution of the pre-bottleneck dynamics is already presented in earlier work [58, 60]. Following up with pre-bottleneck effect, at low enough temperatures, the density of thermally excited EHPs and HFPs can be neglected. Moreover, for

excitation densities, where the gap remains largely unperturbed, the coupled differential equations, (3.2),(3.3), have analytical solutions for *n(t)* and *N(t)*, with the initial conditions n(t∼0) = n_0 and N(t∼0) = N_0 [58]. Here, the delayed rise time dynamics of *n(t)*, which is well separated from recovery dynamics (> 10 ps), can be directly fit with the following analytical expression [58–61]

$$n(t) = \frac{\beta}{R}\left[-\frac{1}{4} - \frac{1}{2\tau} + \frac{1}{\tau\left(1 - Ke^{-\frac{t\beta}{\tau}}\right)}\right]. \tag{3.7}$$

In Eq. 3.7, τ^{-1} and K are the dimensionless parameters determined by the initial conditions, n_0, N_0 and R and β [58–61].

$$\tau^{-1} = \sqrt{\frac{1}{4} + \frac{2R}{\beta}(n_0 + 2N_0)} \qquad K = \frac{\frac{\tau}{2}(\frac{4Rn_0}{\beta} + 1) - 1}{\frac{\tau}{2}(\frac{4Rn_0}{\beta} + 1) + 1} \tag{3.8}$$

Figure 3.7 presents various limiting cases for n(t) in the pre-bottleneck regime, which depend on microscopic parameters R and β, as well as on the initial conditions ($n_0 and N_0$) determined by the e-e and e-ph relaxation rates of hot electrons [58, 61]. Here, n(t) is obtained by convoluting Eq. (3.7) with the Heaviside step-function, where rise time is 100 fs, corresponding to the time resolution of the experiment.

In this simulation, we consider E_g = 15 meV. To determine the absorbed energy density (A), we use the penetration depth of 50 nm and reflectivity of 0.3 extracted from the optical data [42] (e.g. F = 1 muJ/cm^2 corresponds to A = 0.364 meV/ucv or 0.091 meV/Yb). We assume the absorbed energy is distributed between EHPs, with energy per EHPs $E_g/2$, and HFPs with energy E_g such that

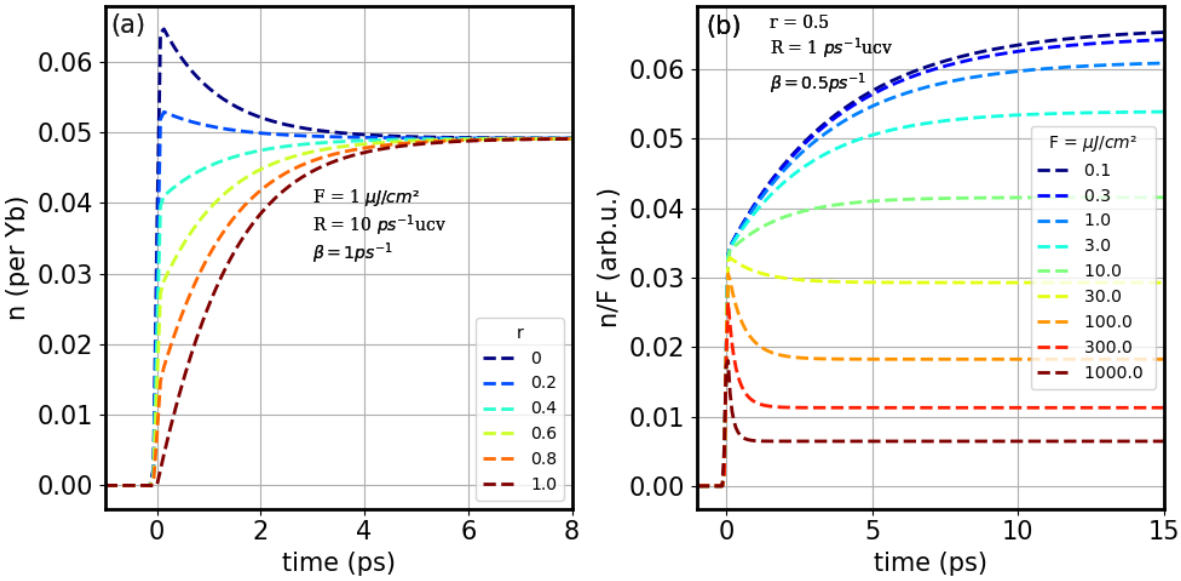

Figure 3.7: (color online): Simulation of the pre-bottleneck dynamics using Eq. (3.7) considering the hybridization gap $E_g = 15$ meV. Panel (a) presents the evolution for constant F = 1 mJ/cm^2 and different values of r from 1 (all the energy initially in the QP channel) to 0 (all the energy initially in the HFP channel). (b) Fluence dependence of dynamics for constant R, β, r (the values are given in the plot). Here n(t) is normalized to excitation fluence, F, to emphasize the nonlinearity of dynamics.

$N_0 = \frac{A(1-r)}{E_g}$ and $n_0 = \frac{2Ar}{E_g}$, where r is the fraction of absorbed energy density, A, in the EHPs channel ($0 \leq r \leq 1$).

Figure 3.7a presents the evolution of the carrier density for different values of r. While for all value of r the same quasi-equilibrium is reached (determined simply by the detailed balance equation, $Rn_s^2 = \beta N_s$), over large range of r the excitation is followed by generation of additional EHPs via HFP absorption (delayed build-up of the signal).

Figure 3.7b presents the excitation density dependence of EHP dynamics using constant values of R, β and r. The absorbed energy density (or F) is varied over four orders of magnitude. At the lowest fluences, the dependence is linear

(normalized traces are identical to the experimental data - see Fig. 3.4), governed solely by the electron-hole pair generation rate β. For higher excitation densities the dynamics becomes nonlinear, reflecting the bi-molecular nature of the electron-hole recombination. At around 10 μJ/cm^2 (for the given choice of parameters) one observes a change in character of the initial dynamics from being governed by pair-generation (delayed build-up) to being governed by the bi-molecular recombination (decay of the signal). In conventional superconductors such a change in dynamics has never been observed at high excitation densities, likely due to the quenching of the superconducting gap before this regime is reached. Comparison of Fig. 3.7b to the experimental data on YbB_{12} (Figure 3.4), however, suggests such a change in dynamics to take place near F = 100 μJ/cm^2 in YbB_{12}.

Following up with the simulation described above, we compare the model with our experimental data to extract the microscopic parameters of YbB_{12}. Here, we perform a global fit to our experimental data. To fit time-traces over the entire time-window, we first determine the (excitation density dependent) values of the recovery rate γ, by fitting the slow recovery dynamics, t > 10 ps by $Be^{-\gamma t} + C$. The resulting function is then multiplied to Eq. (3.7). With the known value of the gap, E_g = 15 meV, the known absorbed energy density, and the extracted γ(F), we perform a global fit of all the datasets, with only three F-independent fitting parameters: R, β and r. As shown in Figure 3.8a, an excellent agreement is obtained, especially considering that the excitation density here spans over three orders of magnitude. The extracted (global) fit parameters are: r = 0.47 +/- 0.01, β = 0.61 +/- 0.01 ps^{-1} and R = 0.14 +/- 0.01 ps^{-1}ucv.

Figure 3.8b presents the intensity dependence of reflectivity change at the 15

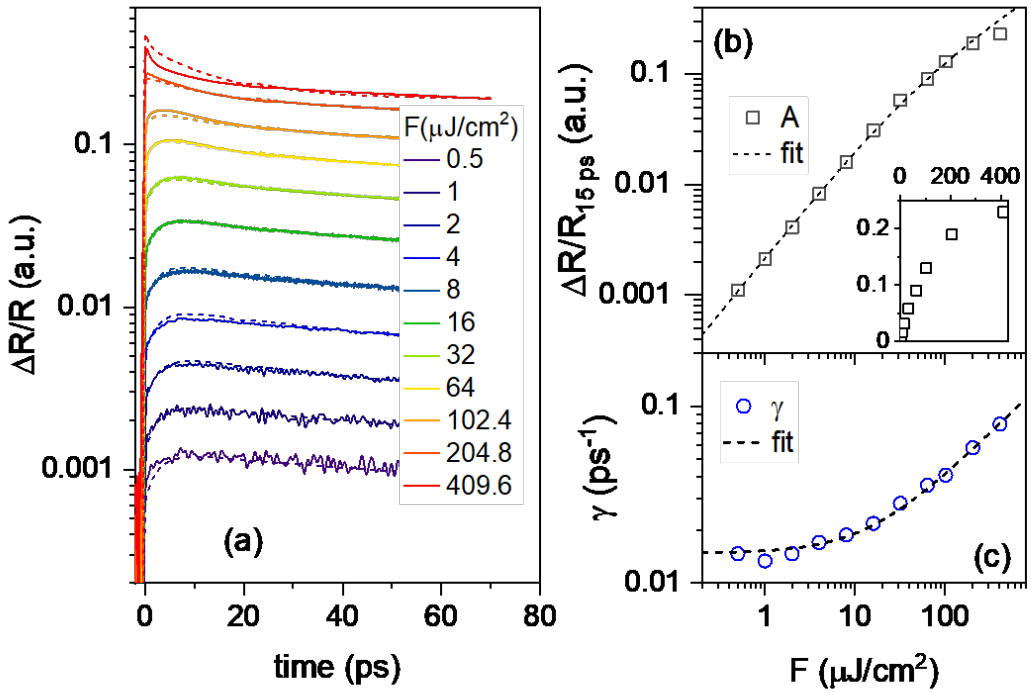

Figure 3.8: (color online): The analysis of the excitation density dependence of transient reflectivity at 5 K using the Rothwarf-Taylor phonon-bottleneck model. Panel (a) presents the data recorded for excitation densities spanning three orders of magnitude (solid lines) fit by the global fit (dashed lines), providing access to parameters R, β and r. (b) The intensity dependence of reflectivity change at 15 ps time delay (open black squares), together with the fit (dashed line) with n_s(F), given by Eq.(3.4). (c) The F-dependence of the relaxation rate g (open blue circles), fit by $\gamma \propto (n_s + C)$ (dashed line). For all fits the same values of microscopic parameters were used: r = 0.47 +/- 0.01, β = 0.61 +/- 0.01 ps^{-1} and R = 0.14 +/- 0.01 ps^{-1}ucv.

ps time delay. Here, we assume that a quasi-equilibrium state, with $Rn_s^2 = \beta N_s$, has been established and we can fit the data with n_s(F), given by Eq.(3.4). An excellent agreement between the experimental data and the fit further supports our analysis with the simple phenomenological bottleneck model. Figure 3.8c presents the F-dependence of the relaxation rate γ, again displaying the behav-

ior constituent with the proposed bottleneck model. Indeed, for low temperatures, γ was shown [58] to follow $\gamma \propto (n_s + n_T)$. Strictly speaking, this relation implies a divergence of relaxation time, where $\gamma^{-1} \rightarrow \infty$ in the limit of T,F $\rightarrow$ 0. However, the model does not take extrinsic effects into account, as for example the diffusion of photo-excited carriers out of the probed volume [54]. Indeed, both temperature and fluence dependent data show a saturation of the initial relaxation time at around 60 ps for T,F $\rightarrow$ 0, which is likely limited by carrier transport into the bulk of the crystal.

Let us now turn to the extracted values of the microscopic fit parameters. The ratio r $\approx$ 0.5 implies a high e-ph relaxation rate of hot carriers, which is consistent with an extremely fast relaxation dynamics at room temperature, where the hybridization gap may already have been closed (e-ph thermalization as in the case of simple metals). Moreover, the rate of creation of electron-hole pairs via HFP absorption, β, is similar to the value obtained in conventional superconductors like NbN [60], whose superconducting gap is of the same order as the hybridization gap of YbB_{12}. What is however dramatically different between the two systems is the extracted value of the bi-particle (electron-hole) recombination rate R, which is in YbB_{12} found to be about three orders of magnitude lower than in NbN[60]. To address this, we consider the detailed balance equation $n_T^2 / N_T = \beta / R$. It follows that the ratio β / R is governed by the densities of states of electrons and phonons (at high temperature, the DOS, $n_T^2 \approx N_T$, thus one would expect similar β / R if it is only the gap that is opening at low-T). Estimating N_T and n_T from [58], it is evident that only a small variation in carrier densities can result in the 1000-fold increase of β / R in YbB_{12} compared to NbN, even though the density of states of conduction band electrons are comparable for both systems [68, 69]. This suggest that the hybridization not only result in

the formation of gap in the density of states (which is also the case in superconductors) but is also accompanied by a strong charge transfer from the localized $4f$ states into the hybridized band.

Importantly, the hybridization gap is quite robust against electronic excitation. As shown in Figure 3.8, the model with a constant hybridization gap is able to reproduce the experimental data up to absorbed energy densities of the order of 140 meV per unit cell (i.e. $\sim$ 35 meV per Yb), which exceeds values in superconductors with comparable gap sizes by two to three orders of magnitude.

3.6 Conclusion

In conclusion, in this chapter we started with providing the basic concept of the HFs and KI and discussed the recent interest in these material class. We performed temperature and fluence dependence all-optical measurements on a prototypical material YbB_{12} and provide the detail analysis of our experimental data. We demonstrate that in YbB_{12} the (indirect) hybridization gap persists to temperatures nearing the room temperature and is quite robust against electronic excitation. Furthermore, we showed that the analysis of excitation density dependent carrier dynamics provides access to microscopic parameters, such as the electron-hole recombination rate. The extracted values of the electron-hole recombination rate suggest the rate is governed by a small number of zone boundary acoustic phonons. Finally, we demonstrate that, below 20 K both the density of photo-excited quasiparticles and their relaxation show a departure from the high temperature behavior, further suggesting the appearance of sub-gap structure in the density of states, with possible origin being the correlation effects between localized moments.

CHAPTER 4

COLLECTIVE MODES IN AN UNCONVENTIONAL CDW $BaNi_2As_2$

More than 60 years have past since the basic concept of the CDW was first discussed by Peierls in 1955 [5]. He pointed out that a one-dimensional metallic state coupled to the lattice is unstable at low temperature and the system could minimize its free energy [5, 70, 71]. Such a coupling of electron and phonon result in the metal-insulator transition into a new ground state leading to the redistribution of the electron density forming a periodic charge density modulation accompanied by the periodic lattice distortion, while both period being described by the Fermi wavevector k_F. This periodic modulation of the electron density is called a CDW. Ever since the basic concept of the CDW has been derived, CDW phase is being realized in many correlated systems, ranging from Transition-metal dichalcogenide (TMD), organic, in-organic solids to unconventional superconductors. In this chapter, we focus on the time-resolved study of

$BaNi_2As_2$. In $BaNi_2As_2$ periodic lattice distortion is observed with two different periodicity above and below structural phase transition temperature. Is this the CDW order? Can we observe collective amplitude modes of the CDW? What is the nature of collective modes in this material? These are the questions we try to address in this chapter. We first start with the introduction to the CDW physics and proceed with the ultrafast pump-probe technique to study the photo-induced change in reflectivity to simultaneously track the ultrafast evolution of lattice and electronic orders. Real time analysis of the experimental data enables decomposition of the response to track the temperature and excitation density dependence of collective modes and thus provides the insight into the nature of these modes. Major part of the result and analysis presented in this chapter are published and adapted from [72]

4.1 Brief introduction to CDWs

CDW order with broken translation symmetry was first proposed by Peierls in 1950s [5], where he described the instability in the one-dimensional (1D) linear chains of atoms against formation of a modulated ground state. In a 1D metal at T = 0 K, without electron-electron and electron-phonon interaction, the linear chains of atoms are arranged in a periodic fashion with the lattice constant a. In this case, the electron states are filled up to the Fermi level, similar to the situation illustrated in figure 4.1(a) (occupancy of the states upto E_F is marked with thick blue line). On the other hand, the Peierls instability occurs in the presence of electron-phonon interaction. As a consequence, the periodic lattice distortion (PLD) occurs (change in atomic periodicity) with period $\lambda = 2a$. Figure 4.1(b), presents the situation of such a reconstructed atomic chain. As a result an energy gap opens up at the Fermi surface, thereby lowering the energy of the occupied

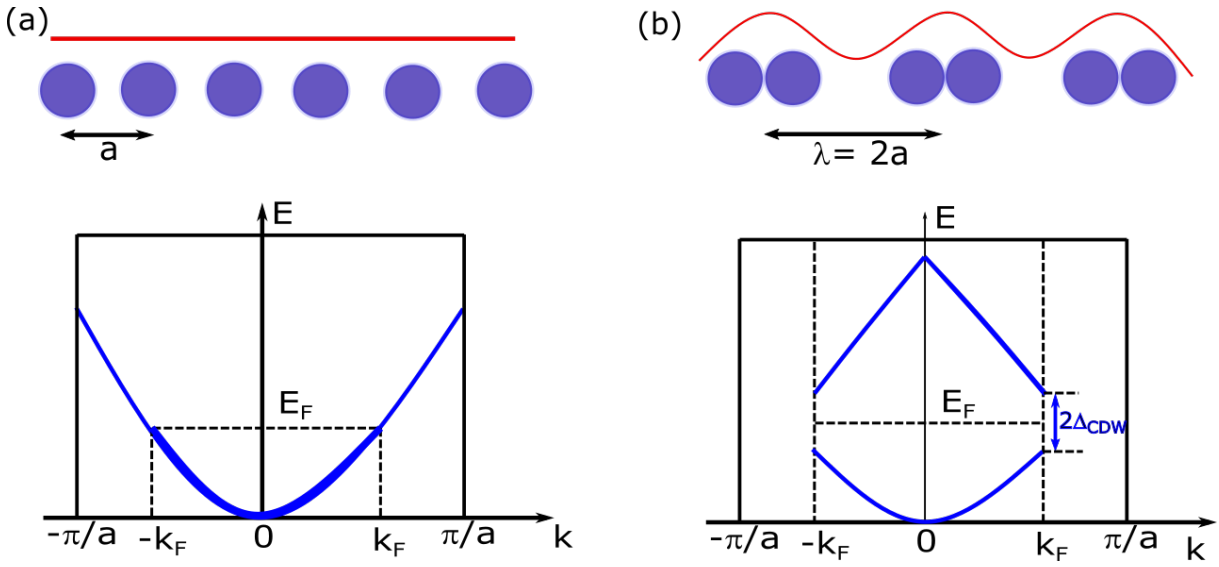

Figure 4.1: Illustration of the Peierls description of the CDW ground state in a one-dimensional metal. (a) Undistorted metal with linear chain of atoms arranged in a periodic fashion with period of lattice constant a. In this case the electron states are filled up to the Fermi level E_F. (b) Illustration of the periodic lattice distortion due to the presence of electron-phonon interaction with new period of $2a$ (a being the lattice constant. The electron band after Peierls distortion with period $\lambda = \pi/k_F = \pi/2a$ that opens up a gap near the fermi level E_F is shown in the bottom panel. Figure adapted from [70].

states and raising the energy of the empty states [73]. The corresponding electronic band structure is presented in figure 4.1(b), with a gap energy of $2\Delta_{CDW}$ at $k = \pi/2a$.

The Peierls transition is best understood by considering a response of the 1D electron gas to an external perturbation. The Lindhard response function $\chi(q)$ defines the system response against external perturbation as a function of q [71, 74]. In 1D for $T = 0$, the Lindhard response function $\chi(q)$ exhibit a divergence at $q = 2k_F$. The calculated response function as a function of q for all q is shown in figure 4.2. For completeness, the response functions in 2D and 3D system are also presented assuming circular of spherical Fermi surface for 2D and 3D case, respectively. The divergence of $\chi(q)$ at $q = 2k_F$ implies that an external pertur-

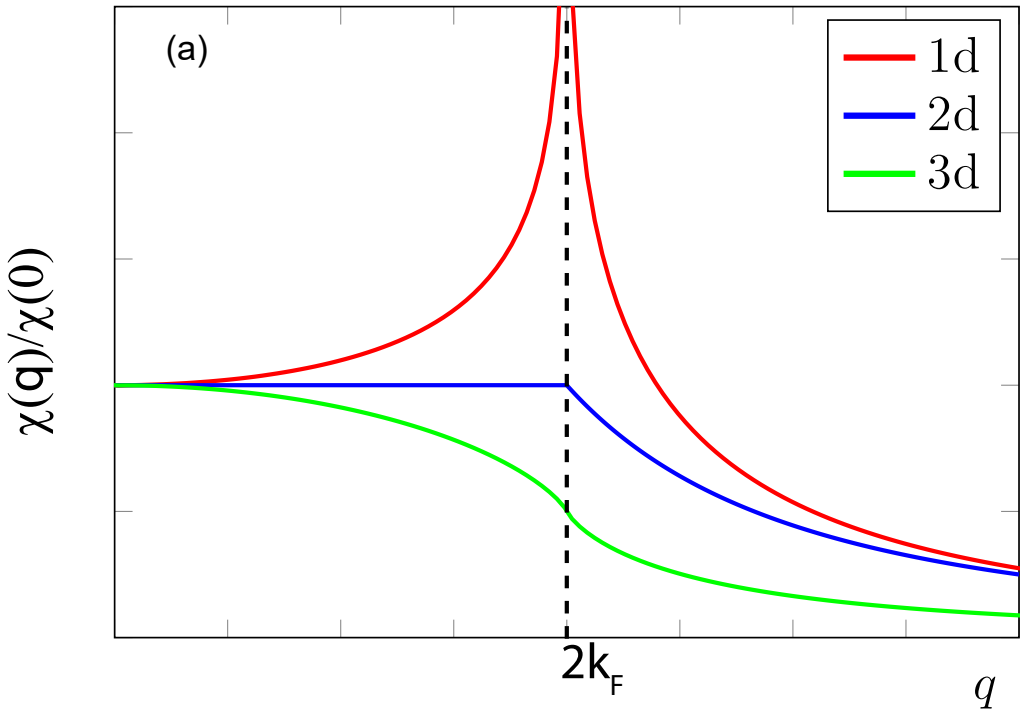

Figure 4.2: Wavevector dependent Lindhard response function for 1D, 2D and 3D system at T = 0. Figure adapted from [71].

bation leads to a charge redistribution, meaning, that at $T = 0$ the electron gas itself is unstable with respect to the formation of a periodically varying electron charge (or electron spin) density with period given by π/k_F [71]. Importantly, the divergence of the response function is caused by the topology of the Fermi surface, in 1D case we have a perfect "nesting" since the Fermi surface in 1D is made of just two fixed points at $k_F = \pm\pi/2a$, leading to various instabilities at low temperatures. In case of 2D and 3D system, one could have nesting driven CDW if large areas of Fermi surface are connected by the same wavevector.

Furthermore, Kohn pointed out in 1954 [75] that there is an 'Image of the Fermi surface in the vibration spectrum', because the zero energy electronic ex-

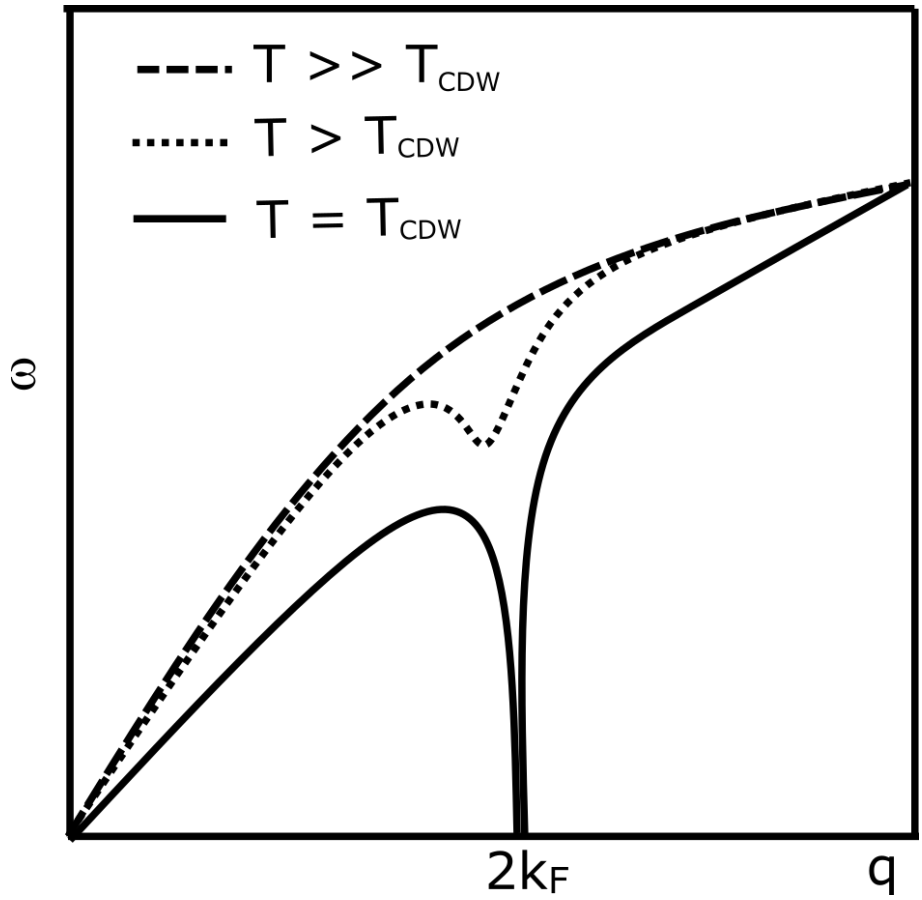

Figure 4.3: Acoustic phonon dispersion relation of the 1D free electron system at various temperature above and at the temperature equal to transition temperature. Figure adapted from [71].

citations at $2k_F$ will effectively screen any lattice motion with this wavevector [76]. The divergence of the Lindhard response function $\chi(q)$ at $q = 2k_F$ leads to the renormalization of the phonon mode with a wavenumber close to $2k_F$. This renormalization of the phonon at $2k_F$ due to the interaction with the electronic system is called the Kohn anomaly [77]. Due to the electron-phonon interaction, the renomalized phonon mode lowers the energy, generally referred to as phonon softening. The phonon renormalization is strongly temperature dependent and the phonon energy decreases as the temperature approaches critical temperature (T_{CDW}) and becomes zero at T_{CDW}. This zero energy phonons are

called frozen phonon modes. The phonon dispersion relation for 1D system is presented in Figure 4.3 at various temperatures. Figure 4.3, illustrate the situation appropriate for the renormalization of an acoustic phonon branch at various temperatures above the phase transition temperature (T_{CDW}). To this end, phase transition is defined by the temperature when the phonon energy goes to zero due to strongly divergent response function of the 1D electron gas.

Indeed, first evidence of the CDW was revealed in 1D systems, including the transition metal chalcogenides MX_3 (M = Nb and Ta, X = S, Se or Te) [71, 78], halogen transition metal tetrachalcogens $(MX_y)_nh$ such as $TaSe_4I$ [79] and blue bronzes $A_{0.3}MoO_3$ (A = K and Rb) [80]. Although the divergence of the Lindhard response function is strictly seen in 1D case, slight divergence of the response function in 2D (see Figure4.2, blue curve) is already an indication of possibility of Fermi surface nesting driven CDW transition in materials with highly anisotropic band structures both in 1D and 2D [8]. Indeed, occurrence of CDW was confirmed in layered TMDs, cuprates and the rear earth tellurides R_2Te_5 (R represents rare earth) [81–83]. In addition, CDW has also been reported in various 3D compounds, including rare earth and alkaline earth intermetallics such as $R_5Ir_4Si_{10}$ [6, 7], RTe_3 [84] (R represents rare earth) and $A_3T_4Sn_{13}$ (A = Ca, Sr; T = Ir, Rh) system [85, 86].

Even though CDW has been reported in multiple quasi-2D and 3D materials, the charge ordering phase transition is not truly analogous with the Peierls' picture. To this end, various observations, models, and interpretations have been put forward such as occurrence of CDW due to $\vec{q}$-dependent electron-phonon coupling (EPC), strong electron correlation effect, orbital degree of freedom playing an important role and so on. While some of the observations and in-

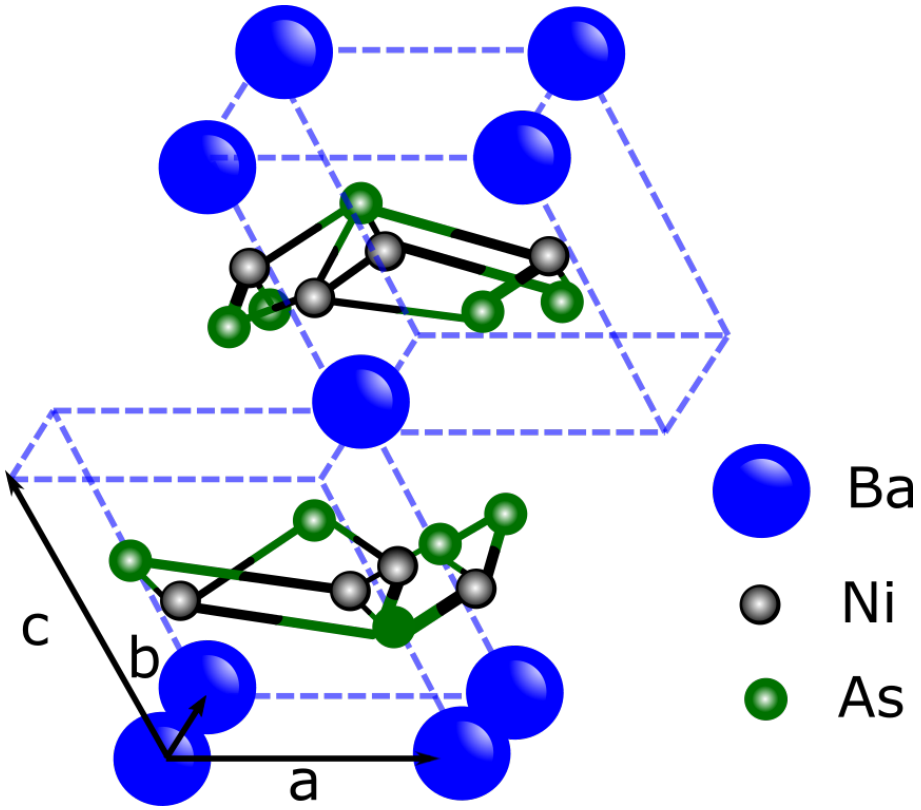

Figure 4.4: **Crystal structure of $BaNi_2As_2$.** Crystal structure showing the triclinic unit cell, with unit cell defined with blue dashed lines. Black arrows indicate the basis vector. Figure adapted and redrawn from [87]

terpretations are well understood and accepted by now, other still remain topics of intense discussion. The complexity in higher dimensions make the mechanism of CDW much more complicated and highly material dependent. Covering all the details of the formation of CDW in different materials is clearly out of the scope of this thesis. Here, we tried to present some fundamental concepts of CDW. For details on the topic of CDW, readers may refer to various articles and review papers [8, 70, 71, 73, 76]. Here, we study the $BaNi_2As_2$ compound, which is a nickel homologue of Fe-based system. The field is at the forefront of research after the discovery of superconductivity in Fe-based compounds [11–15] in the proximity to the magnetically ordered state.

4.2 $BaNi_2As_2$

$BaNi_2As_2$ (Ni-122) is a non-magnetic analogue of Fe-122. It shares the same tetragonal $I4/mmm$ high-temperature structure and upon cooling, undergoes a phase transition below $T_S = 138$ K where the structure is triclinic $P\bar{1}$. Figure 4.4 presents the crystal structure in the triclinic phase. Ni-122 displays superconductivity already in the undoped case ($T_c \approx 0.6$ K) with no magnetic order reported down to the lowest temperatures [88]. Instead, recent X-ray diffraction studies suggest an unidirectional incommensurate charge density wave (I-CDW) slightly above T_S which transforms into a commensurate charge density wave (C-CDW)[1] order on cooling into the triclinic phase [87]. When doping Ni-122 with phosphorus a six-fold enhancement in the superconducting T_c and a giant phonon softening is observed at the doping level where the structural transition is completely suppressed [89]. Similar T_c enhancement at the quantum critical point between the triclinic and tetragonal phases was recently observed also in strontium substituted Ni-122 [90]. Here, the electronic nematic fluctuations were demonstrated in the non-magnetic analogue of Fe-122, exhibiting a dramatic increase in the fluctuation range near the quantum critical point [90]. The observed correlation between the enhancement of superconductivity and the increase in nematic fluctuations, and the same B_{1g} symmetry breaking for both the nematic fluctuations and the CDW order, provide an indication of a charge-order-driven electronic nematicity in Ni-122 [90]. The interplay between electronic nematicity, CDW order and superconductivity in Ni-122 system thus presents one of the most important and interesting topics in the current pnictide research, especially given the parallels to cuprate superconductors [91] that can be drawn.

[1] A charge density wave is termed as commensurate if the new periodicity is a rational fraction of the lattice constant and considered incommensurate if it is not.

The existence of the PLD in Ni-122 system has been demonstrated by X-ray diffraction studies [87, 90, 92, 93]. In undoped Ni-122 diffuse incommensurate superstructure reflections at $(h \pm 0.28, k, l)$ are observed already at room temperature [93] (the indexing throughout of this chapter refers to the high-T tetragonal phase). Upon cooling, the correlation length of modulation strongly increases around 150K, yet the system remains tetragonal [92, 93]. Thermal expansion studies [93] reveal a second order phase transition at $T_{S'} \approx 142$ K, where orthorhombic distortion implies an unidirectional incommensurate CDW, I-CDW$_1$, at $(h \pm 0.28, k, l)$. At $T_S \approx 138$ K [87] a first order structural phase transition to a triclinic structure takes place (both T_S and $T_{S'}$ are transition temperatures upon warming). In the triclinic phase, a new periodicity of PLD is observed, attributed to I-CDW$_2$ with $(h \pm 1/3 + \delta,\ k,\ l \mp 1/3 + \delta)$ superstructure reflections. The discommensuration vanishes, *i.e.* $\delta \to 0$, slightly below T_S, resulting in a commensurate C-CDW [87, 92, 93] with a wave-vector $(1/3, 0, 1/3)$. There are, however, no abrupt changes in the displacement amplitude at the lock-in transition [87]. Given the fact that the triclinic transition is of the first order, with hysteresis of about 5 K, one can argue that the structural transition is concomitant with the I-CDW$_1$ to C-CDW transition.

On the other hand, optical studies, however, show no signatures of the CDW-induced optical gap [94, 95]. To get further support for the CDW origin of the observed PLD [87, 90, 93] and to gain insights into the relation between CDWs and structure, the information on CDW collective modes is required. To this end, we apply time-resolved optical spectroscopy which has been demonstrated to be particularly sensitive to study low-energy $\mathbf{q} \approx 0$ Raman-active collective modes in systems exhibiting CDW order [62, 96–98]. While obeying similar selection rules to conventional Raman spectroscopy [99], the method offers spec-

tral resolution down to 3 GHz (0.1 cm^{-1}) [97], and provide access to modes at frequencies down to 100 GHz (3 cm^{-1}) [98]. In addition, all-optical study is suitable also for investigations of disordered/inhomogeneous samples [100]. Furthermore, the information on the temperature (T) [62, 96–98] and excitation fluence (F) dependent [101–103] dynamics provide insights into the nature of collective ground states.

4.3 Time-resolved study in $BaNi_2As_2$

For all-optical study we use single crystals of $BaNi_2As_2$ with typical dimensions $2\times2\times0.5$ mm^3 that were grown by self-flux method similar to reported literature [89, 104]. Crystals were mechanically freed from the flux and characterized using X-ray diffraction and energy-dispersive x-ray spectroscopy (EDX). The samples were cleaved along the $a-b$ plane before mounting into an optical cryostat and were kept in vacuum during the measurements. Here, we studied the temperature and excitation density dependence of the photo-induced reflectivity dynamics using an optical pump-probe technique (800 nm pump and 800 nm probe) (see Chapter 2). The beams were at near normal incidence, with polarization at 90 degrees with respect to each other to reduce the noise. The fluence was varied between 0.1 - 5 mJ/cm^2 while the probe fluence was kept at 30 $\mu J/cm^2$.

4.3.1 T-dependence of photoinduced reflectivity dynamics in the near-infrared

We start by measuring the temperature dependence of photo-induced reflectivity transients, $\Delta R/R(t)$, upon increasing the temperature from 10K, with fluence $F = 0.4 mJ/cm^2$. The choice of this fluence is that the photo-induced response is

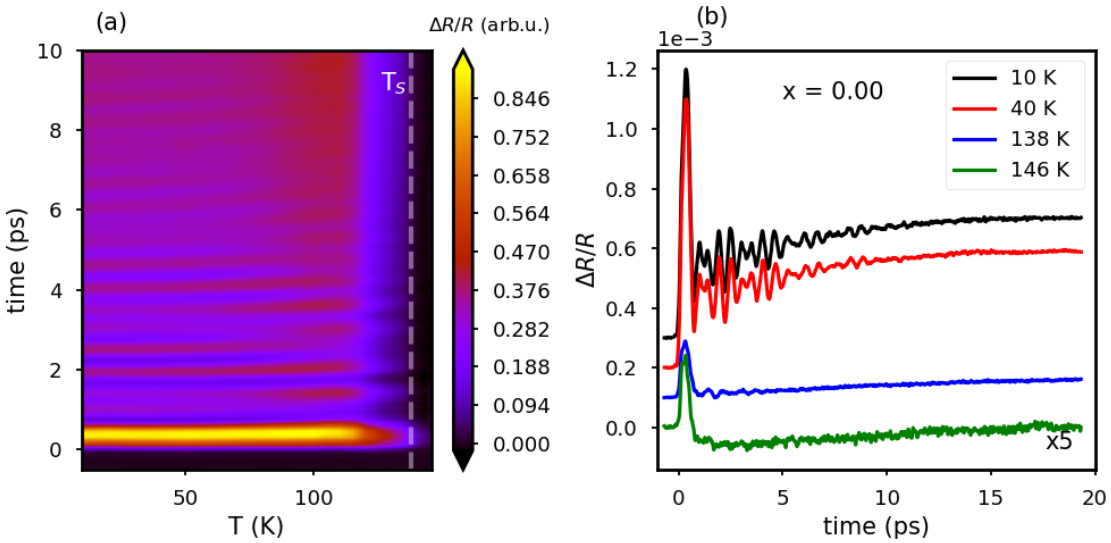

Figure 4.5: Photo-induced change in the in-plane reflectivity on undoped $BaNi_2As_2$ single crystal. (a) Contour map of transient reflectivity between 13 and 149 K, measured with $F = 0.4$ mJ cm^{-2} upon increasing the temperature. Clear oscillatory response is observed on a 10 ps timescale upto the temperature $\approx$ 150 K. (b) Photo-induced change in reflectivity traces at selected temperatures. Figure clearly demonstrate the strong T-dependence of oscillatory and overdamped components.

still linear with fluence, yet it enables high enough dynamic range to study collective dynamics. Figure 4.5(a) presents the contour map of photo-induced reflectivity transients $\Delta R/R(t)$ recorded upon increasing the temperature from 13 K to 149 K. Clear oscillatory response on a timescale of 10 picosecond (ps) is observed upto $\approx$ 150 K, with the magnitude displaying a strong decrease near and above T_S (denoted by vertical white dashed line in Figure 4.5). Figure 4.5(b), presents the photo-induced reflectivity traces at selected temperatures to clearly visualize the oscillatory and overdamped components. In addition to clear temperature dependence of oscillatory components, overdamped response is also strongly T-dependent.

To understand the temperature dependence of photo-induced reflectivity traces,

we first disentangle the oscillatory and overdamped components and analyze them separately. The oscillatory response can be subtracted from the overdamped response by fitting the reflectivity traces by the following exponential decay function:

$$\frac{\Delta R}{R} = H(\sigma, t)\left[A_1 e^{-t/\tau_1} + B + A_2\left(1 - e^{-t/\tau_2}\right)\right], \tag{4.1}$$

where $H(\sigma, t)$ presents the Heaviside step function with an effective rise time σ. The terms in brackets represent the fast decaying process with A_1, τ_1 and the resulting quasi-equilibrium value B, together with the slower buildup process with A_2 and τ_2, taking place on a 10 ps timescale - see the decomposition in inset to Figure 4.6**a**. Figure 4.6**b**, presents the oscillatory part of the signal obtained by subtracting the fit from the reflectivity traces with Eq. 4.1 at selected temperatures.

4.3.2 Collective modes in $BaNi_2As_2$

Here, we start by analysing the oscillatory response to understand the evolution of collective dynamics in Ni-122 over the temperature range between 13 K to 150 K.

First, the residual signal after subtracting the overdamped response at different temperature is analysed using the Fast Fourier Transformation (FFT) to get an overview of the different frequency modes. Figure 4.7 shows the temperature dependence of the FFT of the residual signal left after subtracting fits of the data with Eq.4.1 from the original transients as shown in Fig. 4.6(b). Several modes are clearly resolved already in the FFT spectrum upto 6 THz. However, proper analysis of different modes using FFT spectrum pose difficulties due to

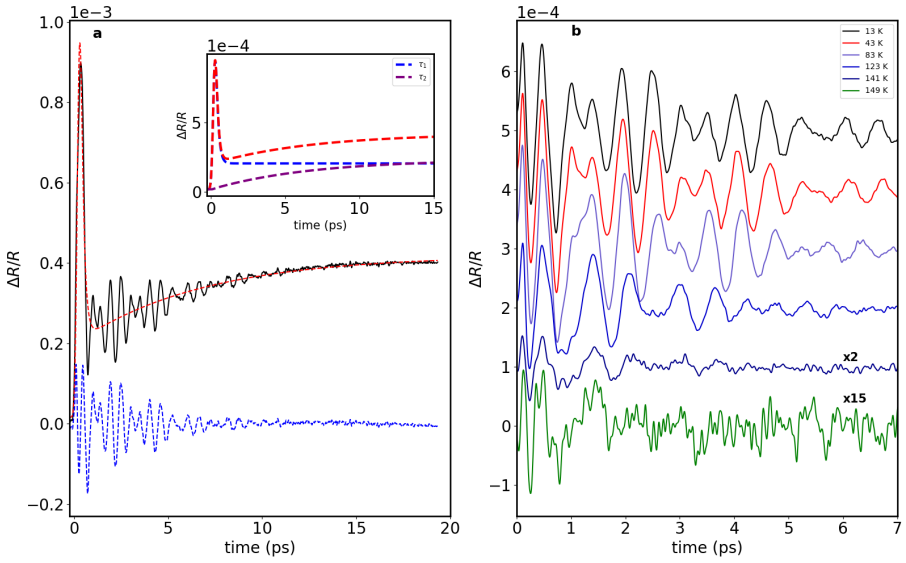

Figure 4.6: Decomposition of oscillatory and overdamped response.**a** Separation of the photo-induced reflectivity transient at 13 K into the overdamped and oscillatory components. Inset shows the decomposition of the non-oscillatory response (dashed blue and purple lines). **b** Oscillatory components at selected temperatures after separating from overdamped response (signals at 141 K and 149 K are multiplied by 2 and 15 respectively).

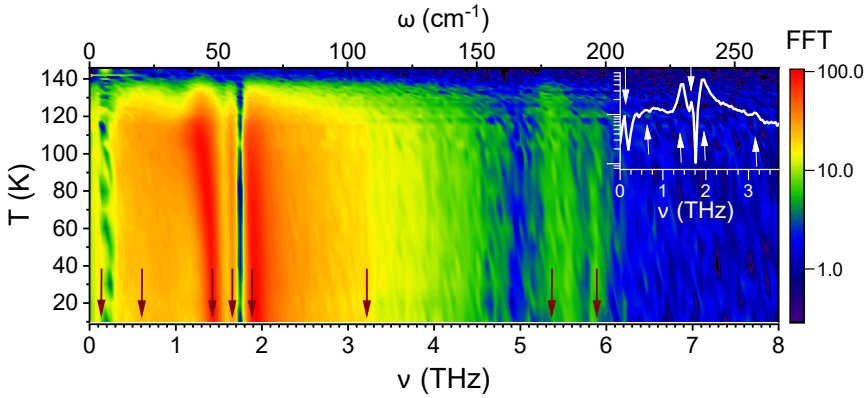

Figure 4.7: Fast Fourier Transform (FFT) contour map. Temperature dependence of the FFT, demonstrating the presence of several modes at low temperatures (denoted by the red arrows). Inset shows the extracted mode frequencies at 13 K (denoted by white arrows).

the incomplete/improper subtraction of the overdamped response especially for the high frequency modes. Note that the fit function 4.1 is only a simplified expression assuming the processes are exponential. To this end, we apply real time fit of the residual signal using sum of damped harmonic oscillators,

$$\sum_i S_i \cos(2\pi\tilde{\nu}_i t + \phi_i) e^{-\Gamma_i t}, \tag{4.2}$$

Taking the information of the different frequency modes from the FFT spectrum as a starting point, we analyze the temperature dependence of the four dominant modes' parameters using the sum of four damped oscillators (see Figure 4.8). Figure 4.8, illustrate the exemplary fitting procedure at 103 K and 143 K respectively. The solid blue line represents the oscillatory part of the signal and is fitted with sum of four oscillators (black dashed line). Individual components are labelled by the corresponding low temperature frequencies.

Performing such a fitting procedure as described above for all data sets, we extracted the evolution of the modes' parameters - central frequencies, linewidths and the spectral weight as a function of temperature. Figure 4.9 presents the results of the analysis of the oscillatory response.

Figure 4.9**a**-**c** presents T-dependences of the extracted mode frequencies ν_i (here $\nu_i^2 = \tilde{\nu}_i^2 + (\Gamma_i/2\pi)^2$ - see [106]), dampings Γ_i, and spectral weights (S_i) of the four dominant modes. Noteworthy, all these low frequency modes are observed up to $\approx$ 150 K, well above $T_S = 138$ K and $T_{S'} = 142$ K. While their spectral weights are dramatically reduced upon increasing the temperature through T_S, their frequencies and linewidths remain nearly constant through T_S and $T_{S'}$.

Generally, the pump-probe technique is mostly sensitive to A_g symmetry mode,

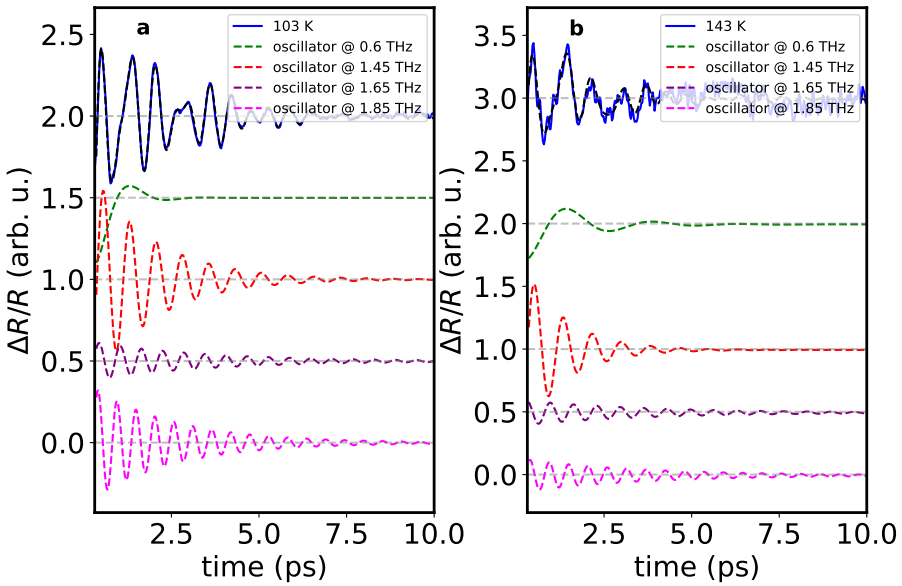

Figure 4.8: **Decomposition of multiple damped oscillator.** Oscillatory response **a** at 103 K and **b** at 143 K (blue solid lines) and the fit using sum of four damped oscillator (black dashed line). Individual frequency components are added for the completeness and offset for clarity.

which couple directly to the carrier density [99, 106]. The stronger the coupling to the carrier density, the larger the spectral weight of the mode. However, in case of broken inversion symmetry, even infrared active modes can be observed [107].

To identify the nature of the modes at low temperature and far above structural transition T_S, we look at the phonon dispersion calculation. In Figure 4.10 we present the result of the phonon dispersion calculations (courtesy of *Rolf Heid*[2]) for the high temperature tetragonal structure. For details on the phonon dispersion calculation one can refer to appendix A. Comparing phonon dispersion calculation and experimentally observed low frequency modes, none of the low frequency modes (see Figure 4.7) matches the calculated $\mathbf{q} = 0$ mode frequencies. Therefore, and based on their T- and F-dependence (will be discussed

[2]Institute for Quantum Materials and Technologies, karlsruhe Institute of Technology

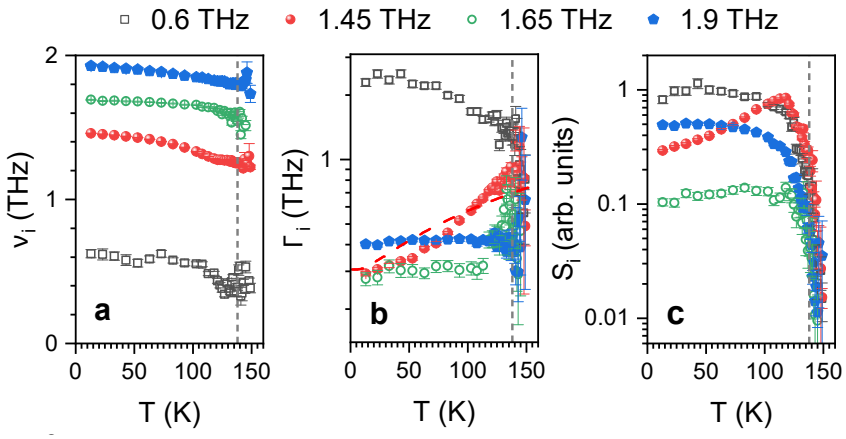

Figure 4.9: Analysis of the oscillatory response. **a**- **c** The temperature dependence of the parameters of the four strongest low-frequency modes, obtained by fitting the oscillatory response with the sum of four damped oscillators: **a** central frequencies, **b** linewidths, and **c** spectral weights. T_S is denoted by vertical dashed lines. The dashed red line in **b** presents the expected T-dependence of the linewidth of 1.45 THz mode for the case, when damping is governed by the anharmonic phonon decay [105]. Figure clearly demonstrate the evolution of the parameters across the triclinic transition at $T_S = 138$ K. The triclinic transition is marked by brown vertical dashed line. The error bars are obtained from the standard deviation of the least-squared fit.

below), we attribute these modes to collective amplitude modes of the CDW order [62, 97, 108–110]. In particular, these low-temperature $\mathbf{q} = 0$ amplitude modes are a result of linear (or possibly higher order [62, 97]) coupling of the underlying electronic modulation with phonons at the wavevector $\mathbf{q}_{CDW}$ (or $n\cdot$ $\mathbf{q}_{CDW}$ for the n-th order coupling [62, 97]) of the high-T phase. Within this scenario [62, 97, 108–111] the low-T frequencies of amplitude modes should be comparable to frequencies of normal state phonons at $\mathbf{q}_{CDW}$ (or $n\cdot$ $\mathbf{q}_{CDW}$ for the higher order coupling), with renormalizations depending on the coupling strengths. Moreover, T-dependence of modes' parameters ν_i, Γ_i and S_i should, in this case, reflect the temperature variation of the underlying electronic order parameter [62, 97, 108–111].

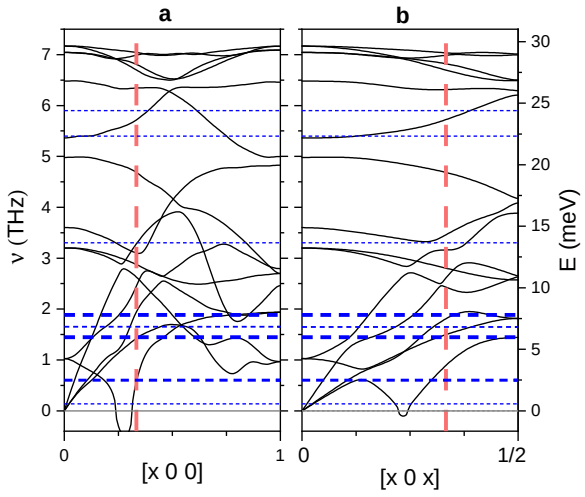

Figure 4.10: Phonon dispersion calculation of the high temperature tetragonal structure. Phonon dispersion along the **a** [100] and **b** [101] directions. The dashed red vertical line in **a** signifies the CDW wave-vectors of the I-CDW while the line in **b** corresponds to the CDW wave-vectors of the C-CDW order. The dashed horizontal lines indicate the low-temperature frequencies of the observed modes. Note that calculations show an instability in an optical branch quite close to the critical wavevector of the I-CDW. The thickness of the horizontal line reflects the modes' strength.

As mentioned above, the first support for the experimentally observed modes to be the amplitude modes follows from calculations of the phonon dispersion, presented in Fig. 4.10. Note that, since these modes appear already above T_S, their frequencies must be compared to phonon dispersion calculations in the high temperature tetragonal phase. Figure 4.10 presents the calculated phonon dispersion in the [100] and [101] directions, along which the modulation of the I-CDW and C-CDW, respectively, is observed. The frequencies of the experimentally observed modes are denoted by the dashed horizontal lines (the line thicknesses reflect the modes' strengths) (see Fig. 4.10).

Indeed, the frequencies of the strongest 1.45 THz and 1.9 THz modes match surprisingly well with the calculated phonon frequencies at the I-CDW modulation wavevector (given by the vertical dashed line in Figure 4.10**a**), support-

ing the linear-coupling scenario. The corresponding (calculated) frequencies of phonons at the C-CDW wavevector, shown in Figure 4.10**b**, are quite similar. As shown in Fig. 4.9, both modes display a pronounced softening upon increasing temperature, much as the dominant amplitude modes in the prototype quasi-1D CDW system $K_{0.3}MoO_3$ [62, 97], as well as dramatic drop in their spectral weights at high temperatures [97]. Finally, the particular T-dependence of Γ for the 1.45 THz mode clearly cannot be described by an anharmonic phonon decay model, given by $\Gamma(\omega, T) = \Gamma_0 + \Gamma_1(1 + 2/e^{h\nu/2k_BT} - 1)$ [105]. Instead, the behavior is similar to prototype CDW systems, where damping is roughly inversely proportional to the order parameter [62, 97].

Given the fact that the structural transition at T_S is of the first order, such a strong T-dependence of frequencies and dampings at $T < T_S$ may sound surprising. However, as amplitude modes are a result of coupling between the electronic order and phonons at the CDW wavevector [62, 97, 109], the T-dependence of the mode frequencies and dampings reflect the T-dependence of the electronic order parameter [62, 97]. Indeed, the T-dependence of PLD [87] as well as of the charge/orbital order [93] do display a pronounced T-dependence within the C-CDW phase.

A strongly damped mode at 0.6 THz also matches the frequency of the calculated high-temperature optical phonon at $\mathbf{q}_{\mathrm{I-CDW}}$. We note, however, that the calculations imply this phonon to have an instability near $\mathbf{q}_{\mathrm{I-CDW}}$, thus the matching frequencies should be taken with a grain of salt. The extracted mode frequency does show a pronounced softening (Fig. 4.9**a**), though it's large damping and rapidly decreasing spectral weight result in a large scatter of the extracted parameters at high temperatures. We further note the anomalous reduction in

damping of the 0.6 THz mode upon increasing the temperature (Fig. 4.9**b**). Such a behavior has not been observed in conventional Peierls CDW systems [62, 97], and may reflect the unconventional nature of the CDW order in this system. We note, that phonon broadening upon cooling was observed for selected modes in $Fe_{1+y}Te_{1-x}Se_x$ [112, 113] and $NaFe_{1-x}Co_xAs$ [114] above and/or below the respective structural phase transitions. Several interpretation have been put forward for these anomalous anharmonic behaviors, that can have distinct origins [112–114].

A weak narrow mode at 1.65 THz is also observed, which does not seem to have a high temperature phonon counterpart at the $\mathbf{q}_{\mathrm{I-CDW}}$. Its low spectral weight may reflect the higher-order coupling nature of this mode.

In addition to the four dominant modes discussed above, several much weaker modes are also observed (see Figure 4.7). Here, we look more closely on the nature of weaker modes observed in the reflectivity data. While these weak modes were resolved already in Fig. 4.7, they are further enhanced through the Fourier Transform of the residuals, obtained by subtraction of fits to the overdamped modes and fits to the main four oscillatory modes from the reflectivity transients. The approach is further sketched in Figure 4.11. Figure 4.11**b** presents the residuals of the fit of the oscillatory component using four damped oscillators (see Fig.4.11**a**) at selected temperatures. By performing the Fast Fourier Transform (FFT) of the residuals (Fig.4.11**b**), we can clearly resolve the weaker modes. Here, Figure 4.11**c** displays the FFT spectra of the residuals. Four weak modes (see the red arrows in Fig.4.11**c**) at frequencies 170 GHz, 3.3 THz, 5.4 THz and 5.9 THz are clearly resolved.

Comparing with phonon dispersion calculation (Figure 4.10), the mode at 5.4

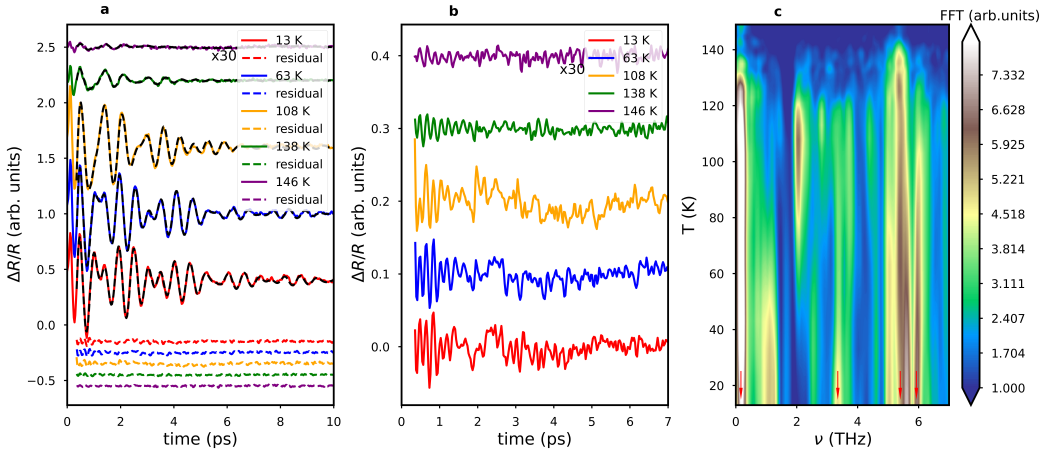

Figure 4.11: Characterization of weaker modes. To determine frequencies of these weaker modes, we first subtract fits to the overdamped response from the $\Delta R/R$ transients, resulting in the oscillatory response. The trace at 146 K has been multiplied by 30 to enhance visibility. **a** Oscillatory response (solid lines) fit to a sum of four damped oscillators (dashed), including the residuals. **b** The residuals of the data at several temperatures, clearly indicating additional periodic reflectivity modulations. **c** Temperature dependence of the FFT spectra of the residuals, clearly demonstrating the presence of several weaker modes in $BaNi_2As_2$. The vertical red arrows denote the low temperature frequencies of the observed weaker modes.

THz is likely the regular A_{1g} phonon which involves the c-axis displacement of As with respect to the Ni square lattice. This mode is commonly observed in time-resolved studies of Fe-122 [115] and is seen also in Raman study at room temperature at 5.28 THz [116]. Also the 3.3 THz mode could be a regular $q = 0$ phonon according to the phonon dispersion calculation, yet it is not observed in Raman studies. The mode at 5.9 THz, on the other hand, is also likely the amplitude mode, as it is neither observed in Raman at room temperature [116] nor it corresponds to a calculated $q = 0$ phonon, and matches the frequency of the phonon at the CDW wavevector (see Fig. 4.10). Finally, there is also a weak mode at $\approx$ 170 GHz (5.67 cm^{-1}). Such a low frequency mode could originate from the acoustic shock wave, propagating with the sound velocity from the sample surface along the c-axis [117]. In such a scenario, the mode

frequency is given by $\nu_a = \frac{2n\nu_s}{\lambda}$, with n being the refractive index at $\lambda = 800$ nm and ν_s the sound velocity along the c-axis. Using ν_s from the calculated phonon dispersions, and with $n \approx 1.8$ [95] gives a much lower value of $\nu_a \approx 30$ GHz. Thus, the 170 GHz mode may also be a result of coupling to the underlying electronic instability. In the case of broken inversion symmetry, even infrared active modes can be observed [107]. If this were the case, this mode could be attributed to a pinned phason. However, up to now no evidence of inversion symmetry breaking in Ni-122 has been reported.

4.3.3 Overdamped modes in $BaNi_2As_2$

We now turn to the overdamped response of the material. Further support for the CDW order in $BaNi_2As_2$ [87, 93] is provided by the T-dependence of overdamped components. Figure 4.12**a** presents the T-dependence of signal amplitudes $A_1 + B$, which corresponds to the peak value of the reflectivity transients near $t = 0$, and A_2 extracted by fitting the transient reflectivity data using Eq. 4.1. In CDW systems the fast decay process with τ_1 has been attributed to an overdamped (collective) response of the CDW condensate [62, 97], while the slower process (A_2,τ_2) has been associated to incoherently excited collective modes [62]. As both are related to the CDW order, their amplitudes should reflect this. Indeed, both components are strongly reduced at high temperatures, with a pronounced change in slope in the vicinity of T_S - see Figure 4.12**a**. Component A_2 displays a maximum well below T_S, similar to the observation in $K_{0.3}MoO_3$ [118]. Above ≈ 150 K the reflectivity transient shows a characteristic metallic response, with fast decay on the 100 fs timescale.

The evolution of timescales τ_1 and τ_2 is shown in Figure 4.12**b**. In the C-CDW phase, up to $\approx 110 - 120$ K, the two timescales show qualitatively similar de-

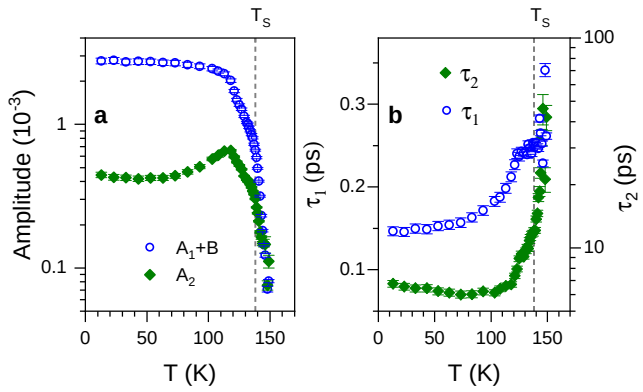

Figure 4.12: Extracted fit parameters of the overdamped components. Temperature dependence of **a** amplitudes and **b** relaxation times, obtained by fitting reflectivity transients using Eq. 4.1. The error bars are the standard deviation of the least-squared fit.

pendence as in prototype 1D CDWs [62, 97, 98]: τ_1 increases with increasing temperature while τ_2 decreases [62, 97, 98]. As τ_1 is inversely proportional to the CDW strength [62, 97], its T-dependence is consistent with the observed softening of the amplitude modes. Its increase with increasing temperature is, however, not as pronounced as in CDW systems with continuous phase transitions, where timescales can change by an order of magnitude when gap is closing in a mean-field fashion [62, 96–98]. From about 130 K τ_1 remains nearly constant up to $\approx$ 150 K. On the other hand, for $T \gtrsim 120$ K τ_2 displays a pronounced increase, though the uncertainties of the extracted parameters start to diverge as signals start to faint. Importantly, all of the observables seem to evolve continuously through T_S, despite the pronounced changes in the electronic and structural properties that are observed, *e.g.,* in the c-axis transport [104] or the optical conductivity [94, 95].

4.3.4 Polarization dependence of transient reflectivity

We performed pump- and probe-polarization dependent studies of transient reflectivity to get additional information on the nature of collective modes and their dependence on the polarization of the pump and the probe light pulses. Both measurement were performed in near-normal incidence (the angles with respect to surface normal were ≈ 8°). Fig. 4.13**a** presents the reflectivity traces recorded at 13 K base temperature with F = 200 μJ/cm^2 with probe polarization being varied between 0° (s-polarization) and 90° (p-polarization), demonstrating negligible probe-polarization dependence. Fig. 4.13**b** presents the corresponding FFT spectra of the oscillatory response, underscoring the polarization independent dynamics.

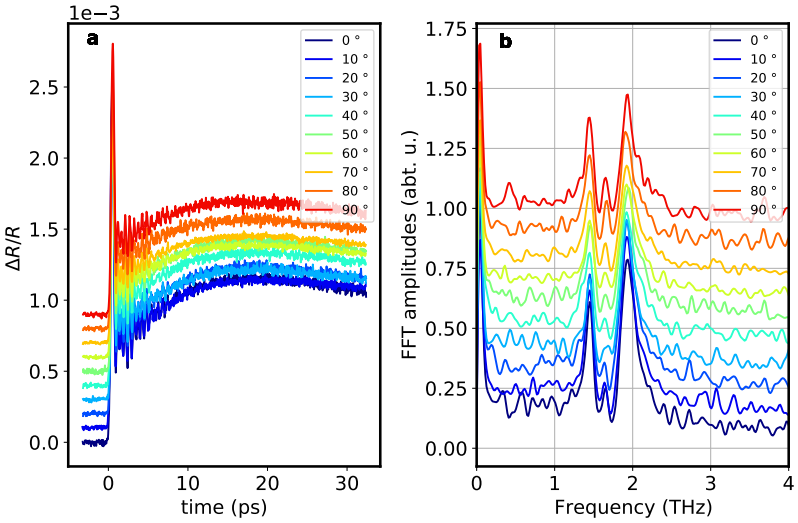

Figure 4.13: Probe polarization dependence of transient reflectivity at 13 K, recorded at excitation density of 200 μJ/cm^2. **a** Reflectivity transients at different probe polarizations from 0° (s-polarization) to 90° (p-polarization). **b** The corresponding FFT of the oscillatory response. Both, reflectivity traces and FFTs are vertically offset for clarity.

4.3.5 Excitation density dependence

Valuable information about the nature of CDW order can be obtained from studies of dynamics as a function of excitation fluence, F. In conventional Peierls CDW systems a saturation of the amplitude of the overdamped response is commonly observed at excitation fluences of the order of 0.1-1 mJ cm^{-2} [98, 101–103]. The corresponding absorbed energy density, at which saturation is reached, is comparable to the electronic part of the CDW condensation energy [101, 103]. Similarly, the spectral weights of amplitude modes saturate at this saturation fluence. The modes are still observed up to excitation densities at which the absorbed energy density reaches the energy density required to heat up the excited volume up to the CDW transition temperature [101]. The reason for this is an ultrafast recovery of the electronic order on a timescale τ_1, which is faster than the collective modes' periods [101].

We performed F—dependence study at 10 K base temperature, with F varied between 0.4 and 5.6 mJ cm^{-2}. The reflectivity transients are presented in Fig. 4.14**a**. Unlike in prototype CDWs, no saturation of the fast overdamped response is observed up to the highest F (inset to Fig. 4.14**b**). The absence of spectroscopic signature of the CDW induced gap in $BaNi_2As_2$ [95] suggest that most of the Fermi surface remains unaffected by the CDW order. Thus, the photo-excited carriers can effectively transfer their energy to the lattice [119], just as in the high-T metallic phase. Nevertheless, the fact that the excitation densities used here do exceed saturation densities in conventional CDW systems by over an order of magnitude suggests an unconventional mechanism driving the CDW in $BaNi_2As_2$. We note that signal A_2 displays a super-linear dependence for $F > 2$ mJ cm^{-2}.

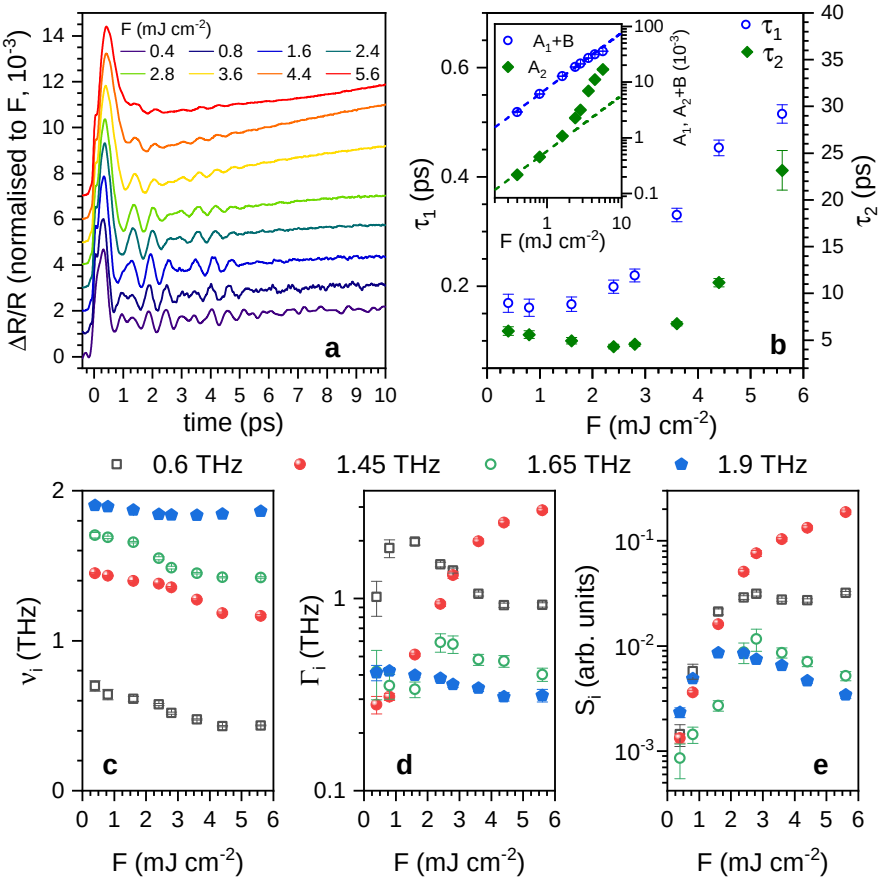

Figure 4.14: Excitation density dependence of collective dynamics recorded at 10 K. **a** Reflectivity transients normalized to excitation fluence. **b** The extracted relaxation timescales τ_1 and τ_2 as a function of excitation fluence, F. Inset presents the F-dependence of amplitudes, with dashed lines presenting linear fits. **c-e** F-dependence of the collective mode parameters ν_i, Γ_i, S_i. The error bars are obtained from the standard deviation of the least-squared fit.

Figure 4.14**b** presents $\tau_1(F)$ and $\tau_2(F)$ for the data recorded at 10 K. Qualitatively, the F-dependence of the two timescales resembles their temperature dependence, similar to observations in Peierls CDW systems [101]. Since τ_1 reflects the recovery of the electronic part of the order parameter, Δ, and it follows from theory [62, 97], $\tau_1 \propto 1/\Delta$, this observation supports a continuous suppression of the electronic order with increasing F. However, in Ni-122 no discontinuous drop in $\tau_1(F)$ is observed up to the highest fluences. In $K_{0.3}MoO_3$ [101] such a drop in $\tau_1(F)$ is observed at the fluence corresponding to the full suppression of the electronic order (about 100 $\mu J/cm^2$)

Figure 4.14**c**-**e** presents the F-dependence of the extracted amplitude mode parameters. A softening upon increasing the fluence is observed for all four modes (Fig. 4.14**c**). However, above ≈ 3 mJ cm^{-2} the values reach a plateau. Such an unusual behavior is not observed in Peierls CDWs [62, 97] and may hold clues to the interplay between the periodic lattice distortion and the underlying electronic instability. An indication of suppression of the underlying electronic order is observed also as saturation of spectral weights of some of the amplitude modes near $F \approx 3$ mJ cm^{-2}, see Fig. 4.14**e.** On the other hand, the mode at 1.45 THz, which is the most similar to main modes in $K_{0.3}MoO_3$, shows no such saturation up to the highest fluences. While the observed anomalies seen near $F \approx 3$ mJ cm^{-2} may be linked to the underlying microscopic mechanism of CDW order in Ni-122, one could also speculate the anomalies may be related to the photo-induced suppression of commensurability.

To put the observed robustness of the CDW against optical excitation into perspective, we note that $F = 1$ mJ cm^{-2} corresponds to the absorbed energy density of about 180 J cm^{-3} (110 meV per formula unit). Assuming rapid thermaliza-

tion between electrons and the lattice, and no other energy decay channels, the resulting temperature of the excited sample volume would reach ≈ 160 K. However, with high conductivity also along the c-axis [104] and the estimated electronic mean free path on 7 nm [120], transport of hot carriers into the bulk on the (sub) picosecond timescale cannot be excluded. Nevertheless, the fact that even at 5.6 mJ cm^{-2} (0.6 eV per formula unit) the CDW order has not collapsed, underscores an unconventional CDW order in in $BaNi_2As_2$ [87, 93].

4.4 Conclusion

In this chapter, we demonstrate the existence of CDW collective modes in $BaNi_2As_2$, which appear well above the triclinic transition temperature. At temperatures well below the triclinic transition, the modes show qualitatively similar temperature dependence as in extensively studied prototype quasi-1D CDW $K_{0.3}MoO_3$ [62, 97, 100]. For temperatures above ≈ 130 K, however, only spectral weights of the modes get suppressed, while their central frequencies and dampings remain largely constant up to ≈ 150 K. This provides an important insight into the relation between the CDW order and the structural phase transitions. While the XRD data [87, 92, 93] clearly show two distinct modulations above and below T_S, the collective modes show no detectable discontinuity of their frequencies and dampings at T_S (nor at $T_{S'}$). This suggests that the C-CDW evolves from the I-CDW$_1$ by gaining additional periodicity along the c-axis. The sequence of phase transitions, with orthorhombicity accompanying the appearance of unidirectional I-CDW$_1$ [93], may suggest charge-order driven nematicity in $BaNi_2As_2$. Moreover, the fact that T_S coincides with I-CDW$_1$—C-CDW transition may in fact support the idea of structural phase transition being mediated by the stabilization of the CDW order. In an alternative scenario, the lock-in CDW supports

the triclinic phase, which otherwise competes with the tetragonal/orthorhombic one, as suggested by the strong reduction of the c/a ratio when entering the triclinic phase, and the first order nature of the transition. The change of the CDW modulation vector is then triggered by the underlying structural change.

While the T-dependence of collective mode dynamics roughly follows the behavior seen in conventional Peierls CDWs, implying the existence of an underlying electronic instability, the resilience of the electronic CDW order against perturbations suggests an unconventional mechanism. Recent photoemission data [121] suggest the band reconstruction to be consistent with the proposed orbitally driven Peierls instability [122, 123]. Such a scenario is further supported by the finding of Ni-Ni dimers [93]. Moreover, also a third type of commensurate CDW order, with $\mathbf{q}_{\mathrm{CDW}} = (1/2, 0, 1/2)$ was observed in $Ba_{1-x}Sr_xNi_2As_2$ for $x > 0.4$ [92]. Thus, systematic doping and pressure dependent studies of collective modes may provide valuable additional clues to the underlying microscopic interactions.

Our results suggest an intimate relation between charge-order and structural instabilities in a Ni-122 system and imply an unconventional origin of the electronic instability, likely associated to orbital ordering [122, 123]. Together with the observed doping dependence of superconducting critical temperature [89], the results provide important input for theoretical models addressing the interplay between high-temperature superconductivity to a close proximity of a competing electronic instability.

4.5 Outlook

4.5.1 Doping dependence study of $BaNi_2As_{1-x}P_x$

We have presented the emergence of collective amplitude modes of the CDW order in an undoped $BaNi_2As_2$ and discussed their nature. Many studies now confirmed the CDW phase is a well established phase in Ni-122 with two distinct periodicity above (I-CDW) and below (C-CDW) the structural phase transition (T_s). At room temperature, the system is in tetragonal phase, as the temperature is lowered the system breaks the rotational point group symmetry into the orthorhombic phase with emergence of unidirectional I-CDW order. The system further breaks the translation symmetry and enters into the triclinic phase with C-CDW order. Furthermore, Ni-122 shows superconductivity already in the undoped case at $\approx$ 0.6 K. One of the intriguing aspect in this material is the great tunability of the superconducting transition temperature. By tuning across the phase transition as a function of chemical doping (be it with Phosphorous on the As site [89], Co/Cu on Ni site [87, 124], or Sr on the Ba site [90]), study revealed the six-fold enhancement of T_c with the suppression of the long range charge order. Furthermore, the correlation of increased electronic nematic fluctuations as a function of doping, suppression of CDW order and the enhancement of superconductivity may suggest the charge order driven nematic fluctuation to be the driving force for the increased T_c in this class of materials. To this end, we proceed with the study of the Phosphorous doped compounds with the similar approach discussed in case of undoped compound. Here, we choose three different doping, one closer to the undoped compound (x = 0.035), second where the superconducting T_c is the highest (x = 0.07) and the last one where the triclinic phase is completely suppressed (x = 0.11). In addition, we compare our results

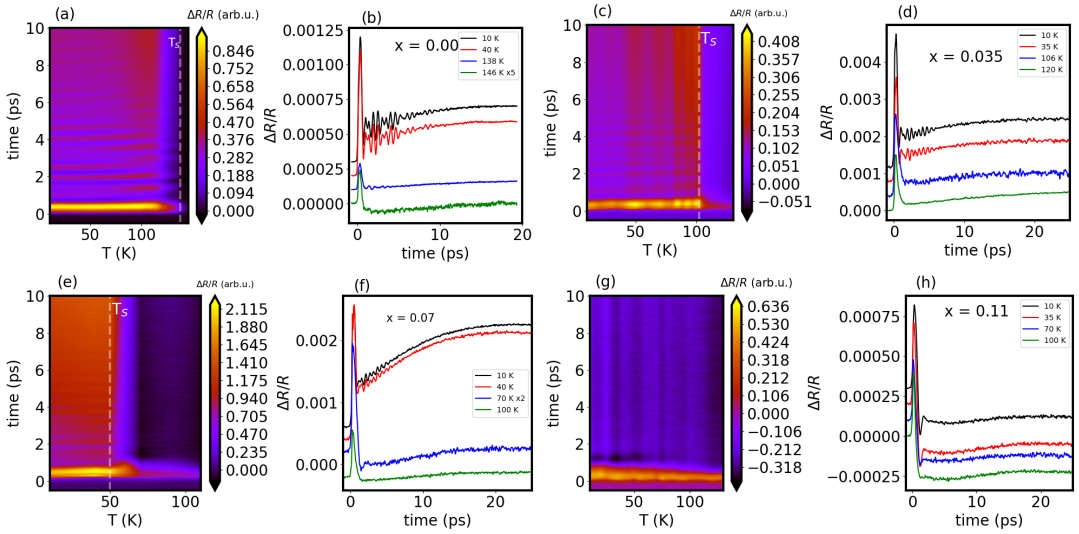

Figure 4.15: (color online): Photo-induced change in reflectivity traces of $BaNi_2(As_{1-x}P_x)_2$ at various doping levels following photo-excitation with 50 fs optical pulses. The measurement is performed at a constant fluence of 0.4 mJ/cm^2 (linear regime) as a function of temperature from 10 K to well above the phase transition in each case. (a), (c), (e), and (g) presents the contour maps of $\Delta R/R$ measured at different dopings, x = 0, x = 0.035, x = 0.07, x = 0.11, respectively. Clear oscillatory (coherent) signal is observed within few picosecond time window with several frequency components (see text) except for x = 0.11, where strongly damped mode is observed within 1 ps. The vertical white dashed line represents the structural phase transition temperature (T_S) at different doping level.(b), (d), (f) and (h) presents the transient reflectivity traces at selected temperatures below and above T_S (see text).

with the undoped compound.

Figure 4.15, presents the photo-induced change in reflectivity recorded at various doping levels by increasing temperature from 10 K to above structural phase transition, T_S, (represented by vertical white dashed line). The data were recorded at a constant fluence of $F = 0.4$ mJ/cm^2 where the response is still in weak perturbation regime (linear) and also enable access to high dynamic range to study the collective response [97]. The photo-induced reflectivity transients for different Phosphorus content, x = 0, x = 0.035, x = 0.07 and x = 0.11 are

presented as a contour maps in Fig 1 (a), (c), (e), and (g) respectively. Clear oscillatory (coherent) response is observed with stripe like shape within first few ps. Figure (b), (d), (f) and (g), presents the corresponding transient reflectivity spectra at selected temperature above and below the phase transition, T_S, except for figure 1 (g) where the triclinic phase is completely suppressed. However, strongly damped mode is still visible in the reflectivity traces upto $\approx$ 100 K. The photo-induced reflectivity traces show the incoherent electronic background together with the coherent (oscillatory) response with multiple frequency components (discussed later). Comparing the reflectivity traces of different dopings, the amplitude of the oscillatory response is found to be stronger in case of undoped sample. The reason simply could be due to the sample quality, measurement errors (external noise due to vibrations) or could also be due to intrinsic fluctuations with increasing doping levels. Nevertheless, the overall trend of the material response at different dopings seem to follow the undoped case except for x = 0.11.

To better understand the oscillatory mode containing several frequency components, we proceed with subtracting the incoherent electronic background with similar approach described above in case of undoped compound. The residual of the fit (oscillatory response) is then Fourier transformed to observe the oscillation spectrum. The Fast Fourier Transform (FFT) of the coherent response and their temperature evolution is presented in Figure 4.16. Several amplitude modes of the CDW phase is observed upon lowering the temperature similar to the undoped compound (see Fig. 4.16(a), (b) and (c)). The low- temperature frequencies of these modes could be linked to amplitude modes of the C-CDW modulation wavevector and present similar behavior as in the case of undoped compound. Dominant modes at 0.6 THz, 1.45 THz, 1.6 THz and 1.9 THz are

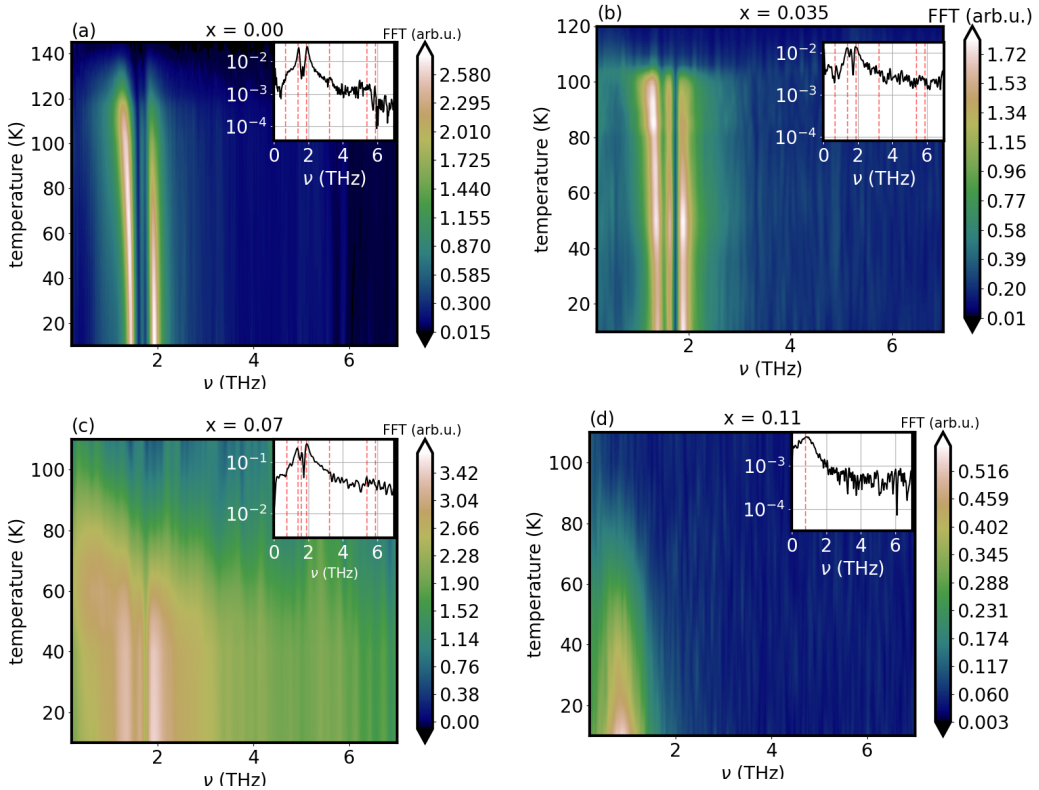

Figure 4.16: (color online): Fast Fourier Transform (FFT) of the oscillatory response. Temperature dependence of the FFT contour maps demonstrating the several frequency modes at various doping level with (a) x= 0, (b) x = 0.035, (c) x = 0.07 and (d) x = 0.11 respectively. Several frequency components with distinct modes appear at low temperature C-CDW phase, with more dominant ones, at frequencies 0.6 THz, 1.45 THz, 1.6 THZ and 1.9 THz for the case of x= 0.0, x = 0.035, and x = 0.07. For the case of x = 0.11, mode at ≈ 0.6 THz slowly softens with increasing temperature and disappear at ≈ 100 K. Inset to each sub-figure shows the FFT trace at 10 K emphasizing several oscillatory modes (highlighted by vertical red dashed line).

present in case of x = 0.035 and x = 0.07 at low temperature and show signature of their existence above triclinic to orthorhombic phase transition, T_S, being consistent with the undoped compound. Moreover, several other frequency components with distinct modes are also visible at 3.2 THZ and 5.5 THz, highlighted by vertical red-dashed line in the inset of Figure 4.16. However, because of the phase fluctuation, these modes are not clearly traceable in the contour maps.

One of the striking observation is the strongly damped mode ≈ 0.6 THz that persist even in case of x = 0.11 sample. The 0.6 THz mode is present in all doping levels at low temperature in the triclinic phase and shows signature of it's existence above structural phase transition in the orthorhomic phase. Is this the signature of the I-CDW mode in the orthorhombic phase that persist even at the triclinic phase? Does this mode become dominant above triclinic to orthorhombic phase transition? What could be the existence of such strongly damped mode? These are still the open questions that need to be address. From our experimental data and the preliminary analysis, the ≈ 0.6 THz mode seem to exist above T_S in the orthorhombic phase and becomes dominant above T_S and with increasing doping concentration. In the first approximation, one can link this mode to the signature of the amplitude mode of I-CDW modulation wavevector, as recent study show the orthorhombic phase to be present even in case of x = 0.11 doped compound all the way down to lowest temperature reached in our experiment [125]. However, more recent thrmodynamic study show that with increasing P content, the system enters into a new phase [126]. The study show that the triclinic and orthorhombic phase disappear near x = 0.08 and are replaced by a new structure leading to the higher superconducting T_c. The study quote the new phase as an hitherto unknown structure. However, this new phase has not been clearly understood. More detail analysis and doping dependence

study at various doping levels could clarify this. In addition, performing similar all optical study (described in this chapter) on other doping compounds, e.g., (Ba,Sr)Ni_2As_2 could help us in understanding the nature of the strongly damped mode and also on the nature of the emergence of new phase.

CHAPTER 5

PHOTO DOPING OF La_2CuO_4

Another class of strongly correlated materials which was investigated within this thesis using time-resolved spectroscopy includes the Mott insulator with partially filled d-electron shell. In particular, we investigated La_2CuO_4 a parent compound of the cuprate high temperature (high T_c) superconductors. The era of high T_c cuprates began in the late 90s when Bednorz and Müller discovered the superconductivity in the complex, layered structure La-Ba-Cu-O ceramics [10]. Ever since many materials are being synthesized and the critical temperature was raised rapidly. All of these materials have copper-oxide planes in common as a main ingredient and are layered structure. Superconductivity emerges in cuprates after electron or hole doping of an antiferromagnetic Mott Insulating ground state. After brief introduction of the Mott insulators and high - T_c superconductivity in cuprates, we present the study of carrier relaxation dynamics using broadband time-resolved spectroscopy. Most of the broadband optical measurements on La_2CuO_4 investigated in this chapter, were performed at the University of Konstanz by former colleague *Markus Bayer* [127]. During

my PhD, I got heavily involved in understanding the photo-doping phenomena in LCO and performed further analysis of the experimental data that lead us to prepare a manuscript for publication. This chapter mainly focuses on the analysis performed and investigation of all the data.

5.1 Mott-Insulator and Charge Transfer Insulator

Mott insulators are the class of strongly correlated materials which should be in the metallic state according to the band structure calculations but are insulating due to the strong electron-electron correlations, the idea first presented by Mott in 1949 [128]. Mott pointed out that the two electrons with spin up and spin down sitting on the same site would feel a strong Coulomb repulsion and the band will split onto two. The lower band is fully occupied and the upper band is empty and the system is an insulator. However, the situation gets more complicated near the metal-insulator transition (MIT) where the fluctuation of charge, spin and orbital correlations are strong.

One of the theoretical model for understanding the transition between Mott insulator and metal was achieved by using lattice fermion model called Hubbard Model. For details reader can follow [29, 130–132]. According to the theory, if the Coulomb repulsion energy (U) between the electrons on the same site is stronger than the hopping integral (t), it is energetically favorable for electrons to remain localized. As a consequence the half filled d-band split into Upper Hubbard Band (UHB) and Lower Hubbard Band (LHB) with insulating behavior. Figure 5.1**a** presents the scenario of a Mott insulator where the half filled d-band split into UHB and LHB and the Fermi level (E_f) lies in-between two splitted

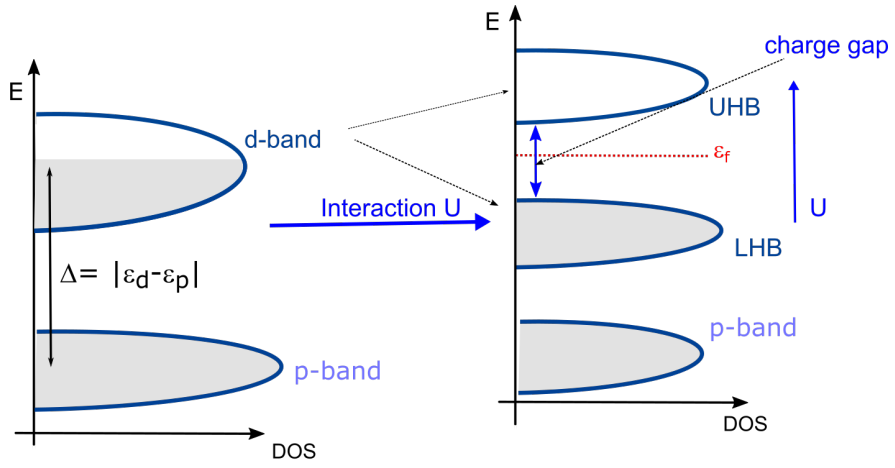

a Mott-Hubbard Insulator

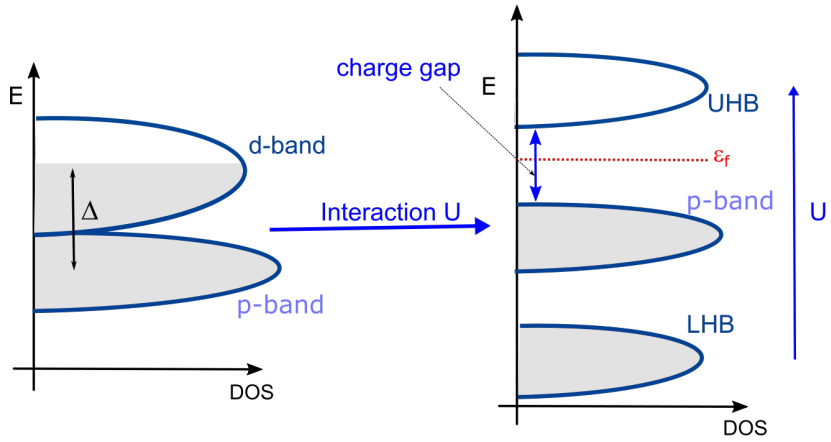

b Charge Transfer Insulator

Figure 5.1: Illustration of the Energy band diagram for **a** Mott-Hubbard insulator and **b** a charge transfer insulator generated by the d-site interaction effect. The occupied d and oxygen 2p band are shaded light gray. Fermi level after interaction effect lies within the gap and is represented by red dashed line. The Mott-Hubbard gap due to on-site coulomb interaction is created between Upper Hubbard Band (UHB) and Lower Hubbard Band and is represented by U. The charge transfer gap (Δ) is created between the UHB and oxygen 2p band. Figure adapted and redrawn from [129]

bands. This implies that the gap here is the $d-d$ gap, the concept only being true for several Mott insulating compounds. Furthermore, Zannen *et al.* [133] extended the Mott Hubbard model, in which, they consider the ligand orbitals in the binding scheme (CuO_2 planes consist of Cu and ligand Oxygen). Considering

the $p-d$ hybridization and the hopping parameters, there was an indication of another charge fluctuation which does not involve U but instead charge transfer energy, Δ. Depending on the size of the U and Δ, one can determine the nature of the energy gap. Figure 5.1**b** presents the concept of charge transfer insulator where the charge transfer gap (Δ) is smaller than the Coulomb repulsion (U), making it a charge transfer insulator which explicitly include oxygen p-band and copper d—band. Indeed, this is the case for LCO where Δ essentially describes the energy needed to promote an electron from oxygen (O_{2p}) ligand orbital to the copper (Cu_{3d}) orbital. Therefore, LCO is commonly referred to as a charge transfer insulator.

5.2 La_2CuO_4 Crystal Structure and Phase Diagram

La_2CuO_4 (LCO) is the antiferromagnetic (AFM) parent compound of the La based cuprates like $La_{2-x}Sr_xCuO_4$ (LSCO) and $La_{2-x}Ba_xCuO_4$ (LBCO), where the superconductivity emerges after doping CuO_2 planes by substituting La with Sr/Ba. The LCO system has the simplest structure among the cuprates family with single CuO_2 plane per unit cell and is thus called a single layer compound. LCO crystalizes in a body-centered tetragonal structure with CuO_2 square plane together with corner sharing array of CuO_6 octahedra. Figure 5.2 presents the crystal structure of LCO. It has a Perovskite like crystal structure composed of CuO_2 planes spaced by 3D transition metal block layers, LaO.

Staring from the undoped parent compound, LCO, and increasing the concentration of doping for example by substituting trivalent lanthanum (La^{3+}) with divalent strontium (Sr^{2+}) or barium (Ba^{2+}) one can tune through different phases.

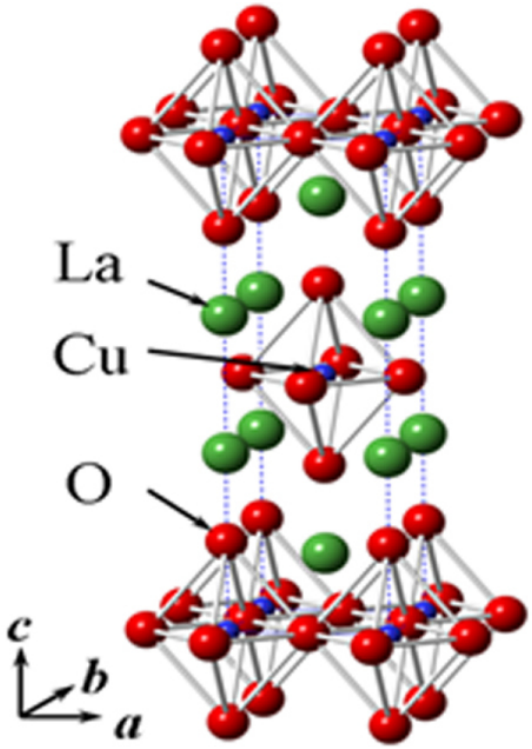

Figure 5.2: Crystal structure of La_2CuO_4. The La, Cu, and O atoms are represented by green, blue and red closed circle respectively. Figure adapted from [134].

In a doped semiconductor picture, the resulting compound is *p*-doped as doping with Sr or Ba removes one electron per copper atom and introduces a hole in the copper oxide plane. By increasing the hole concentration, long range magnetic order disappear and superconducting dome appears. The superconducting dome is maximum at so-called optimal doping where the transition temperature (T_c) into the superconducting phase is the highest. Figure 5.3 presents the exemplary phase diagram of the $La_{2-x}Sr_xCuO_4$ with increasing concentration of Sr.

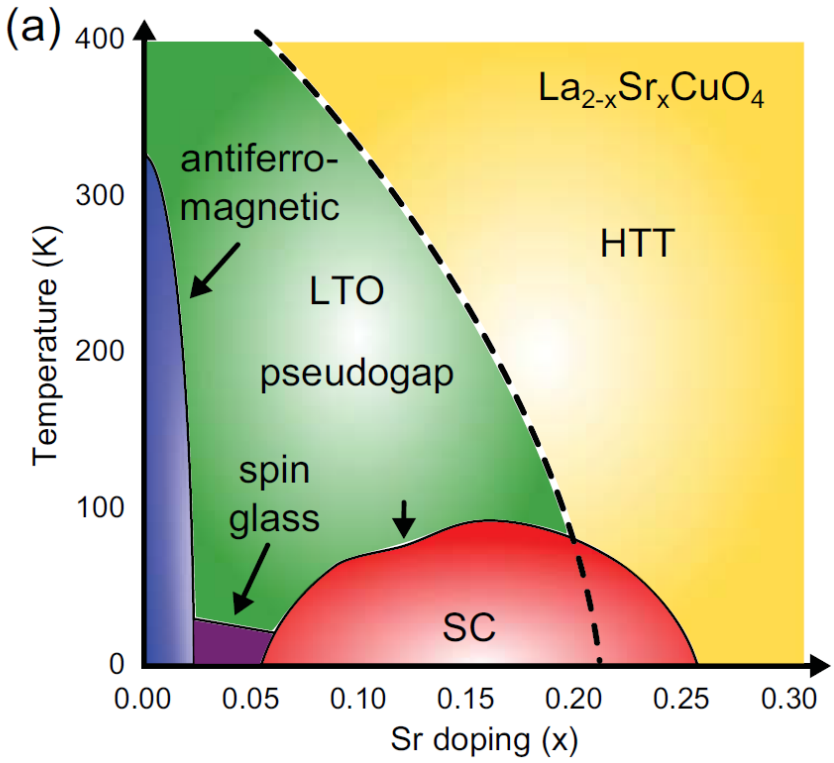

Figure 5.3: Example of a Phase diagram of $La_{2-x}Sr_xCuO_4$. By increasing the concentration of Sr, evolution of different phases including superconductivity is shown. LTO, SC and HTT refer to low temperature orthorhombic, superconducting and high temperature tetragonal phases respectively. Figure adapted from [127].

5.2.1 Optical properties

The parent compound, LCO, investigated here is characterized by a $\approx$ 1.5-2.0 eV charge-transfer gap between the oxygen-derived p-band, located within the Mott gap, and the upper Hubbard band (UHB) (see Fig.5.1**b**). One question that arises is what happens to the electronic structure of the material by doping. Indeed, earlier optical study shows a very strong influence of chemical (hole/electron) doping on the optical spectra with dramatic changes in the spectral weight and the low energy electronic structure [135]. Figure 5.4 presents the optical conductivity measurement on $La_{2-x}Sr_xCuO_4$ with increasing Sr con-

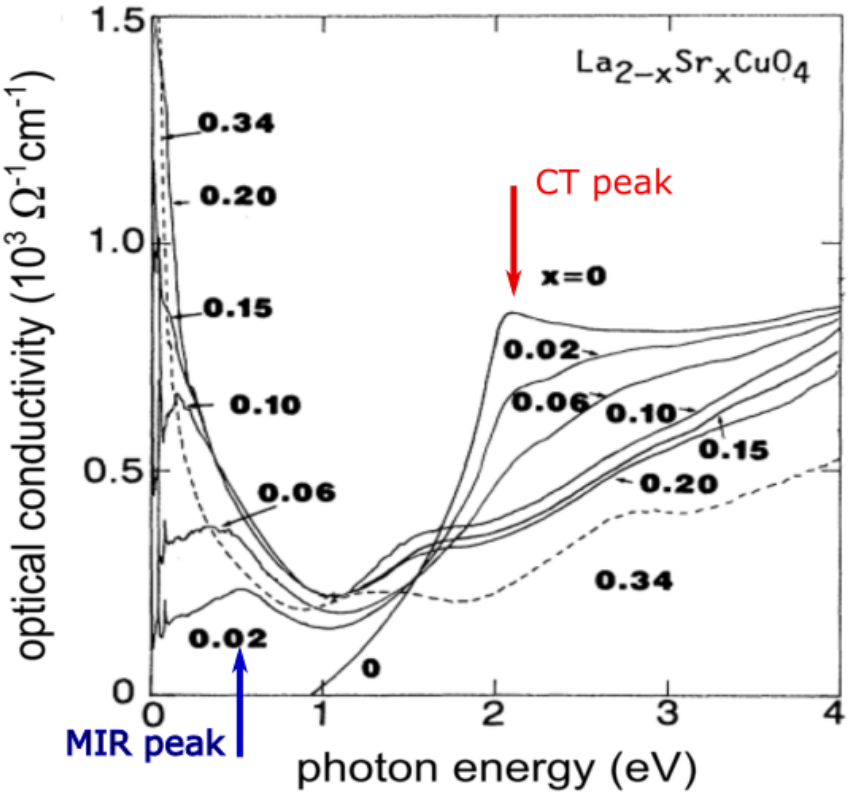

Figure 5.4: Optical conductivity of $La_{2-x}Sr_xCuO_4$ with varying doping concentration (x). By increasing the concentration of Sr, mid-infrared absorption features appears which eventually merge into the Drude free carrier peak as the doping level approach optimal doping. Figure adapted from [135].

centration. Upon increasing Sr concentration, transfer of spectral weight from the charge transfer gap ($\approx$ 2 eV) to low energy region has been observed, with emergence of excitation in the Mid-infrared (MIR) region. When the doping level reaches optimal doping, the MIR peak then eventually merges into the free carrier Drude peak.

However, similar to the problem in understanding high- T_c superconductivity in cuprates, the nature of changes in the low energy structure upon chemical doping, e.g. by introducing a few percent of electrons or holes into the CuO_2 planes is still under intense debate [135–137]. To understand the nature of

MIR excitation feature, several models have been put forward ranging from incoherent motion of doped carriers against the background of AFM spin fluctuations [138, 139], optical transitions involving doping-induced in-gap [140] and Zhang-Rice singlet states [141], polaronic effects [142–144], the interplay between the strong correlations and strong electron-phonon interaction (Hollstein-Hubbard model) [136], just to name the most prominent ones. While the consensus on the nature of MIR peak is still lacking, it can be argued [145] that understanding the nature of MIR excitation carries important clues to understanding the mechanism of high- T_c superconductivity.

5.3 Photo-doping

One aspect of doping a material is the chemical doping, however, chemical doping is not the only way of adding charge carriers into the CuO planes. Substituting with impurity atoms can further induce disorder and can cause possible defects and stain effects in the material. On the other hand, photo-doping creates "free" carriers without inducing disorder, making it a viable technique to study the doping dependent materials' properties. Indeed, soon after the discovery of high-T_c superconductivity in cuprates, first photo-doping studies (excitation with light across the CT gap) were performed, showing a surprising similarity of the changes in optical constants obtained by photo- and chemical doping [146, 147]. Recently, transient absorption studies with femtosecond time resolution showed that the dynamics of photo-induced MIR absorption in undoped LSCO and $Nd_{2-x}Ce_xCuO_4$ (NCCO) proceeds on the femtosecond/picosecond time-scale [148–150], with signatures of transient metallicity in NCCO on the 100 fs timescale [148, 149]. Even though the dynamics of charge carrier in the vicinity of the CT gap have been reported in the earlier studies,

several interpretation have been put forward despite qualitatively similar experimental results. To this end, we investigate the carrier relaxation dynamics in LCO thin films aiming to address the confronting views on the nature of photo-doping and the resulting relaxation dynamics.

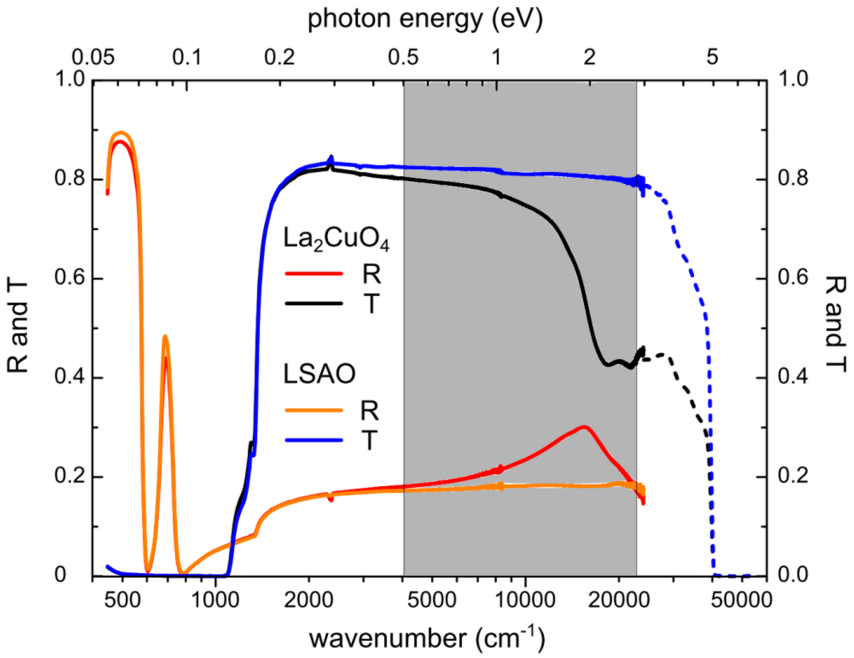

Figure 5.5: Equilibrium reflection and transmission spectra of an undoped LCO sample and blank LSAO substrate in the 0.05 to 5 eV range. Pronounced reflectivity structures at 500 and 700 cm^{-1} are the reststrahlen bands between the transverse optical (TO) and longitudinal optical (LO) modes of the infrared active optical phonons of the substrate material. The direct band absorption of the LSAO substrate sets in at roughly 5 eV and features related to phonons dominate the spectra below 0.2 eV. The focus of the pump-probe experiments is conveniently set to the artefact free spectral range (0.5 -2.6 eV) depicted by grey shaded area. Figure adapted from [127].

5.3.1 Sample and equilibrium properties

The system under study is a high-quality, c-axis oriented, 52 ± 1 nm (80 monolayers) LCO thin films grown on both $LaSrAlO_4$ (LSAO) and $(LaAlO_3)_{0.3}(Sr_2AlTaO_6)_{0.7}$ (LSAT) substrates using molecular beam epitaxy [151]. The film thickness is substantially less than the optical penetration depth at the pump wavelength

of 400 nm, to ensure the homogeneous excitation and probing over the complete spectral range. Prior to the pump-probe measurement the set of samples (undoped films on LSAO and LSAT substrates) and bare substrates were characterized with an FTIR spectrometer to clearly distinguish between thin film and possible substrate responses. The equilibrium reflection and transmission data together with bare LSAO substrate is presented in Figure 5.5 for comparison, over two orders of photon energy (0.05 to 5 eV). The charge transfer (CT) feature is nicely seen at $\approx$ 2 eV, peaking in reflection and analogously showing up as absorption edge in transmission. Besides, the spectrum has a gradual and flat trend in the MIR, as expected for the undoped material. Taking the equilibrium spectra for reflectivity, $R(\omega)$ and transmission, $T(\omega)$, through the LCO thin film on the substrate, as well as the bare substrate, and using Fresnel equation analysis, we obtain the equilibrium complex dielectric function of LCO, $\epsilon(\omega)$, which is found to be consistent with infrared spectroscopy data [135] on single crystals.

5.3.2 Time-resolved study

We measured simultaneously the spectrally resolved transient changes in reflectivity, $\Delta R/R(\omega, t)$, and transmission, $\Delta T/T(\omega, t)$ at room temperature (295 K). For performing such an experiment a fast scan pump-probe setup was used with a time resolution of $\approx$ 120 fs. The sample was excited by a 70 fs pulse at 400 nm, with excitation fluence varied between 100 μJ/cm^2 to 10 mJ/cm^2, corresponding to the absorbed densities ranging from 0.0015 to 0.125 absorbed photons per Cu. The photo-induced changes were recorded over the broad spectral range between 0.5-2.6 eV using an optical-parametric-amplifier. This allows us to determine the changes in the dielectric function of LCO on an ultrafast timescale without the use of a Kramers-Kroenig transformation.

Figure 5.6**a**, **b** presents the time resolved broadband spectra (0.5 – 2.6 eV) with excitation fluence F = 1.8 μJ/cm^2. Combining $\Delta R/R(\omega,t)$ and $\Delta T/T(\omega,t)$ with the static $\epsilon(\omega)$ - see insets to Figure 5.6**c**, **d**, $\Delta\epsilon(\omega,t)$ was extracted by numerically solving a system of Fresnel equations using the so-called RT-method (see appendix B) [152–154]. The extracted $\Delta\epsilon_1(\omega)$ and $\Delta\epsilon_2(\omega)$ are shown in Fig. 5.6**c** and **d**, respectively. At a first glance, one can distinguish large changes near the near the CT gap at $\approx$ 2 eV. From the enhanced absorption below and bleaching above $\approx$ 2 eV, one can infer that the response at frequencies above $\approx$ 1.5 eV is governed by the photo-induced red-shift of the O 2p – UHB charge transfer (CT) transition and its subsequent recovery. Moreover, data reveal the appearance of photo induced absorption (PIA) in the MIR, peaked near $\approx$ 0.6 eV. The relaxation of both spectral features initially proceeds on a (sub) ps timescale, suggesting a common origin.

From the changes in optical constants near $\approx$ 2 eV, with enhanced absorption below and bleaching above $\approx$ 2 eV, we can clearly infer that the response at frequencies above $\approx$ 1.5 eV is largely governed by the photo-induced red-shift of the O 2p – Cu 3d charge transfer (CT) gap and its subsequent recovery. The red-shift of the CT gap has been observed in earlier studies on cuprates [155, 156], as well as on other Mott insulators. The detailed analysis (presented below), shows that the red-shift is accompanied by a substantial spectral broadening of the transition, while the changes in the spectral weight of the CT transition are marginal. These observations are consistent with recent theoretical calculations, which attribute the photo-induced red-shift and broadening of the CT peak to changes in the local orbital occupancy and screening [157].

The microscopic origin of the MIR peak induced either by chemical doping or

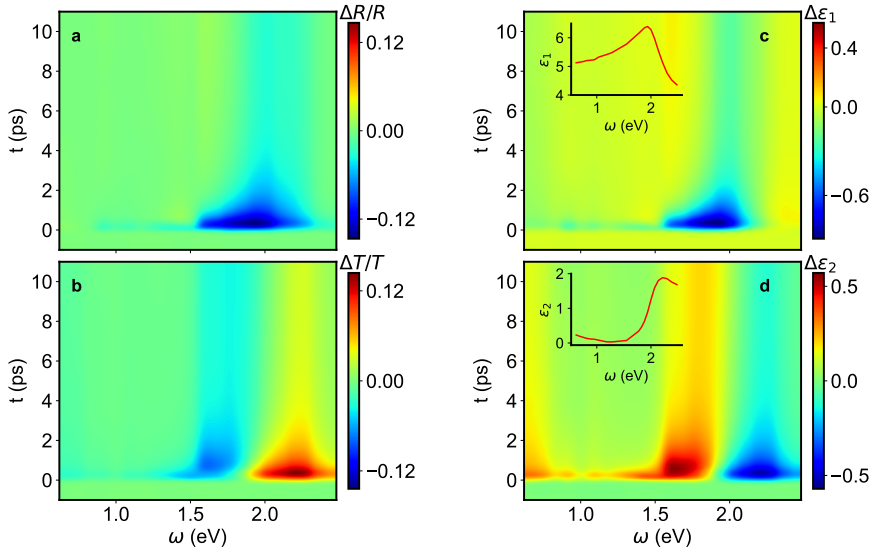

Figure 5.6: Photo-excited carrier dynamics in La_2CuO_4 probed by broadband optical time-resolved spectroscopy. Time- and spectrally resolved **a** $\Delta R/R$ and **b** $\Delta T/T$ on undoped 53 nm LCO film (T = 295 K) after photo-excitation with a 70 fs pulse at 400 nm (3.1 eV) with fluence F = 1.8 mJ/cm^2. **c**, **d** The extracted dynamics of changes in the complex dielectric function with equilibrium $\epsilon(\omega)$ in insets.

photo-excitation is more controversial [135, 136, 138, 139, 141, 158–160]. It follows from the chemical doping studies – be it with oxygen in La_2CuO_{4+d} or with strontium in $La_{2-x}Sr_xCuO_4$ (LSCO) – that the MIR peak, combined with a further absorption feature in the vicinity of 0.13 - 0.2 eV, merges with the far infrared Drude-like peak when doping reaches about 11% [135]. Moreover, it has been observed that the effective density of charge carriers within the CT gap, obtained throught the optical sum-rule analysis, at the low doping levels exceeds the density of chemically doped carriers, x. This indicates an additional spectral weight transfer into the MIR from both the CT transition and the higher lying excitations [135].

5.3.3 Modelling the changes in the dielectric function

A detailed look at the photo-induced changes in the $\epsilon(\omega)$ provides insight into the microscopic origin of the light induced changes. To this end, we quantitatively model the changes in the complex dielectric function, $\Delta\epsilon(\omega)$ using multi-Lorentz model.

$$\epsilon(\omega) = \epsilon_\infty + \sum_j \frac{f_j}{{\omega^2}_j - \omega^2 - i\omega\gamma_j} = \epsilon(_\infty) + \sum_j \epsilon_j(\omega) \tag{5.1}$$

Here, each mode(oscillator) is characterized by its spectral weight, f_j, central frequency, ω_j, and spectral linewidth, γ_j, while ϵ_∞ sums up the contributions of all interband transitions at energy above the experimentally accessible window. We limit the number of modes to a minimum. In particular, we account for the measured changes in the complex dielectric function by considering photo-induced changes in parameters (f_j, ω_j, γ_j) of individual modes. As an example, we discuss the induced changes in $\epsilon(\omega)$ due to photo-induced changes in the charge transfer transition, which is simulated by a Lorentz resonator centered around 2 eV, and characterized by the parameters (f_{CT}, ω_{CT}, γ_{CT}). This example is shown in Figure 5.7. Here, a single Lorentzian oscillator is assumed to describe the absorption edge observed at the charge-transfer transition at $\approx$ 2 eV in equilibrium (red curves in the upper panels). The changes in the dielectric function after photo-excitation can be a result of the change in eigen-frequency $\Delta\omega_{CT}$, giving, e.g., rise to the red-shift of the CT peak (middle panels), or changes in the linewidth $\Delta\gamma_{CT}$, e.g., the broadening of the CT resonance (lower panels), or changes in the spectral weight Δf_{CT}. In case of the latter, the spectral shape of the induced changes of the dielectric constant matches the shape of the dielectric

function itself (upper panels), whereby the sign would be changed in the case $\Delta f_{CT} < 0$.

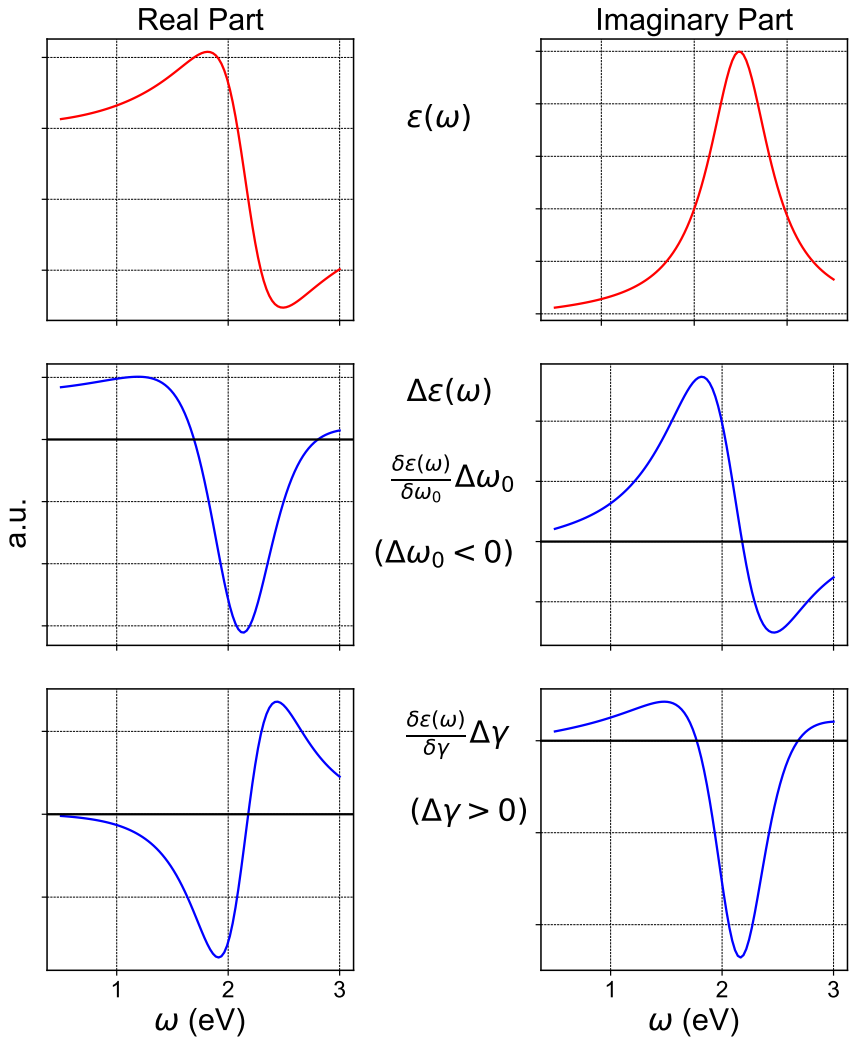

Figure 5.7: Visualization of the resulting changes in $\Delta\epsilon$ by varying the essential parameters of a Lorentzian oscillator. Top panels present the static dielectric function of the unperturbed case, $\epsilon(\omega)$, with ω_0 =2.2 eV, γ_0 = 0.83 eV and f_0 =1 .9 $(eV)^2$. The bottom two rows present the resulting changes in the real part (left), and the imaginary part (right) for the case of photo-induced red-shift of the mode (middle panels) and broadening (bottom panels). Naturally, the reduction/gain of the oscillator spectral weight has the same spectral shape as the oscillator itself.

Now, using the approach described above we start analysing the data. We

start by fitting the equilibrium optical spectra, $\epsilon(\omega)$ using Eq.5.1. Figure 5.8**a** presents the model fit of the experimental $\epsilon_2(\omega)$ of the LCO film, denoted by blue curve. Indeed, as presented in the figure, the experimental data is well modelled by $\epsilon(\omega) = \epsilon_\infty + \epsilon_{CT}(\omega) + \epsilon_{HE}(\omega)$. Here, $\epsilon_{CT}(\omega)$ is the mode corresponding to the CT transition (shown in light red) and $\epsilon_{HE}(\omega)$ is an extra high energy mode (light gray). Furthermore, to account for the changes in the dielectric function and to account for the emergence of the MIR peak, we modeled the data with:

$$\Delta\epsilon(\omega) = \Delta\epsilon_{CT}(\omega) + \epsilon_{MIR}(\omega) + \epsilon_{Drude}(\omega) \tag{5.2}$$

Here, $\Delta\epsilon_{CT}(\omega)$ is governed by the $\Delta\omega_{CT}$ and an increase in linewidth, $\Delta\gamma_{CT}$. $\epsilon_{MIR}(\omega)$ represents the photo-induced MIR mode, centered at $\approx$ 0.6 eV, while $\epsilon_{Drude}(\omega)$ is the possible coherent Drude response.

To account for $\Delta\epsilon(\omega)$ recorded at 0.9 mJ/cm^2, it is actually sufficient to include the reduction of ω_{CT}, an increase in γ_{CT} and the appearance of the MIR mode - see Figure 5.8 **c**, **d**. The fact that no reduction of the CT oscillator strength f_{CT} is required to fit $\Delta\epsilon(\omega)$, suggests that the appearance of the MIR peak must be accompanied by the spectral weight transfer from energies above $\approx$ 3 eV into the MIR range. In other words, the appearance of the MIR is likely to be linked to the spectral weight loss of the optical transition between the lower and upper Hubbard band (LHB-UHB). Moreover, the photo-induced spectral weight loss of the LHB-UHB transition should give rise to a photo-induced reduction of ϵ_∞. However $\Delta\epsilon_\infty$ is likely to be too small to resolve, given the large spectral weight at energies above 3 eV [135].

Following up with the analysis described in figure 5.8, we proceed with the

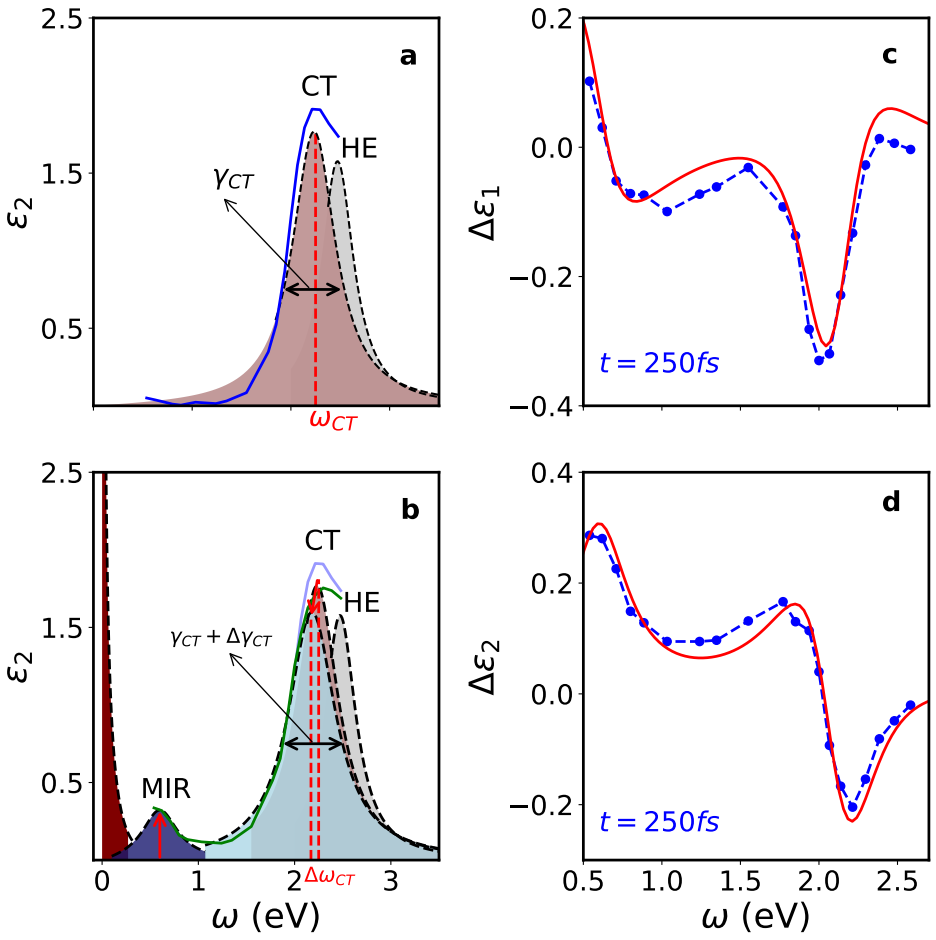

Figure 5.8: Fitting equilibrium $\epsilon(\omega)$ and its photo-induced change, $\Delta\epsilon(\omega)$, by a simple multi-Lorentz model. **a**,**b** Imaginary part of the dielectric function, $\epsilon_2(\omega)$, of the undoped LCO in equilibrium and 250 fs after photo-excitation with F = 0.9 mJ/cm^2 (0.0125 photon per Cu), respectively. Experimental $\epsilon_2(\omega)$ in the equilibrium and in the excited state are shown by the solid blue and green lines, respectively. Both datasets are fit with a multi-Lorentz model, with individual oscillators represented by black dashed lines/ shaded areas. The excited state can be described by the red-shift ($\Delta\omega_{CT}$) and broadening ($\Delta\gamma_{CT}$) of the CT transition, and the appearance of a MIR peak centered at 0.64 eV. We also include the Drude peak (dark red) with the highest spectral weight allowed by the constraints provided by the experimental $\epsilon(\omega)$. **c**,**d** The corresponding spectrally resolved $\Delta\epsilon_1(\omega)$ and $\Delta\epsilon_2(\omega)$, respectively. Experimental data are shown in by blue circles connected by dashed blue line, while the solid red lines present the best fit with Eq.5.2.

excitation fluence dependence dynamics. Chemical doping studies [135] shows that with the increasing doping the MIR peak merge into the coherent Drude peak as the doping level reaches optimal doping. In the first approximation one could expect similar response in the case of photo-doping. To address the photo-doping scenario, we vary the excitation over three order of magnitude and follow the model (see Eq.5.2) to quantitatively analyse the changes in the broadband complex dielectric function $\Delta\epsilon(\omega)$.

Figure 5.9 presents the peak (at 0.2 ps) photo-induced changes in $\epsilon(\omega)$ for the data recorded over a range of excitation densities up to F = 9 mJ/cm^2 (0.125 ph/Cu). The first surprising observation is, that the photo-induced MIR peak grows continuously, without noteworthy shift to lower frequencies, as observed in the case of chemical doping [135]. This is exemplified by a nearly constant position of the energy where $\Delta\epsilon_1$ changes sign, which is pinned at the $\omega_{MIR} \approx$ 0.6 eV. Moreover, even for photo-doping of 0.125 ph/Cu, the measured $\Delta\epsilon_1$ (0.5 eV) > 0. For comparable chemical doping levels $\epsilon_1(\omega)$ (and not only $\Delta\epsilon_1(\omega)$) becomes negative below the corresponding renormalized plasma frequency ω_p (0.6-1.0 eV, depending on doping [135]). This observation suggests the absence - or a negligible contribution - of the photo-doped carriers to the coherent free carrier response. Nonetheless, photo-excitation could result in a Drude-like contribution to $\epsilon(\omega)$ at frequencies below our experimental range, as suggested by recent studies [148, 149, 161]. To estimate the upper limit of the spectral weight of the coherent free carrier response, we added a Drude term to the fit (see Eq. 5.2) with a frequency independent scattering rate, γ_{Drude}, and the spectral weight f_{Drude} as a fit parameters. Using characteristic values for LSCO [135, 162], of γ_{Drude} = 60 THz (2000 cm^{-1}), we obtain the upper limits of the Drude spectral weights as shown in Fig. 5.9 **c**. The resulting f_{Drude} does not exceed 0.1

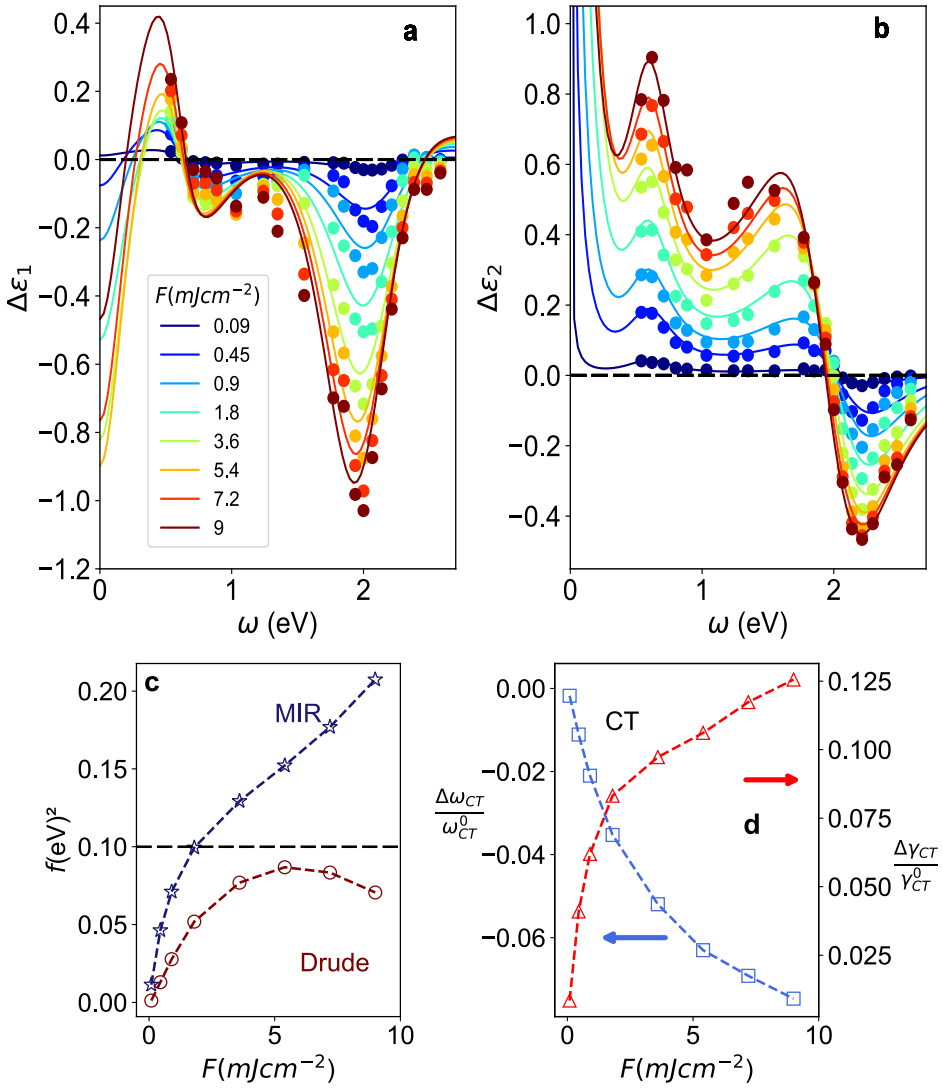

Figure 5.9: Photo-induced changes in the complex dielectric function over large range of excitation densities. **a**,**b** The excitation density dependent $\Delta\epsilon_1(\omega)$ and $\Delta\epsilon_2(\omega)$, given by solid symbols, fit by Eq.5.2. The best fits are represented by solid lines. Even though we do not access the low frequency part of $\Delta\epsilon(\omega)$ directly, the recorded changes pose strong constraints on the spectral weight (or plasma frequency) of the free carrier (Drude) peak. **c** Excitation density dependence of the extracted spectral weights of the photo-induced MIR and Drude peaks. **d** The extracted relative changes in the position of the CT peak (open blue squares) and the CT linewidth (open red triangles). Dotted lines are guide to the eye.

eV^2, corresponding to the (unscreened) plasma frequency of ≈ 0.3 eV. Comparison with the spectral weight of the photo-induced MIR peak, shown in panel **c** of Fig. 5.9**c**, confirms that the character of the low energy excitations does not change substantially with increasing excitation density, i.e., the MIR does not merge with the free carrier Drude peak, even at the highest photo-doping levels.

Our analysis demonstrates that the spectral weight builds up inside the CT gap, most of which is accumulated in the MIR range. The weak/absent contribution of photo-induced carriers to the coherent transport, the rapid picosecond relaxation of mid-gap absorption (discussed below) together with the absence of luminescence in LCO, suggest that the photo-excited charge carriers quickly form weakly bound e-h pairs, which can be considered as Mott-Hubbard excitons [163, 164]. With their binding energy of the order of the AFM coupling strength $J \approx 130$ meV, the optical conductivity of such photo-generated e-h pairs was calculated to have a similar shape to the conductivity spectra of lightly doped cuprates [165]. In this calculation, a rather sharp peak at the binding energy is followed by a broad MIR continuum, corresponding to the incoherent motion of released holons and doublons, plowing through the AFM background [164]. Unlike in the case of chemical doping, both electron-like and hole-like excitations can contribute to the MIR absorption. While their corresponding absorptions may be spectrally separated [164], as suggested by an earlier study [148], no clear evidence of such is observed here, i.e., the peaks are likely too close to be resolved.

5.3.4 Optical sum rule analysis

Photo-excited density dependence and their relaxation dynamics lends further support to the nearly localized nature of the excited carrier. We use the optical

sum rule analysis to follow the excitation density dependent time evolution of the carrier density. The general optical sum rule links the total carrier density, n, with the integral of the real part of the optical conductivity

$$n = \frac{2mV}{\pi e^2} \int_0^{\infty} \sigma_1(\omega^{'}) d\omega^{'} \tag{5.3}$$

where m is the electron mass and V is the unit cell volume (ucv). To estimate the number of photo-excited carriers contributing to the coherent and incoherent transport in LCO, a partial optical sum rule can be used, with the upper frequency limit in Eq. 5.3 set below the optical transitions across the CT gap [135]. From our spectral analysis it follows that the shape of the photo-induced $\sigma_1(\omega)$ does not dramatically change with increasing excitation density, i.e., there is no major shift of the PI MIR peak to lower frequencies, neither does the MIR linewidth change substantially. Therefore, $n_{eff}^{PI}(\omega, t)$, the effective density (in the units of 1/Cu atom) of photo-induced charge carriers involved in the optical transitions up to a photon energy $\hbar\omega$ at a given time delay t, can be estimated as

$$n_{eff}^{pI}(\omega_c, t) = C[n_{eff}^{*}(\omega_c, t) - n_{eff}^{*}(\omega_c, t < 0)] \tag{5.4}$$

$$n_{eff}^{pI}(\omega_c, t) = \frac{2mV}{\pi e^2} \int_{0.5eV}^{\hbar\omega_c} \sigma_1(\omega^{'}, t) d\omega^{'} \tag{5.5}$$

Here ω_c is a cut-off frequency and C is a multiplication factor that takes into the account the contribution to the integral – see Eq.5.3 - from the spectral range below 0.5 eV. For our case C should be of the order of 2, since roughly half of

the MIR spectral weight is below 0.5 eV, and the spectral weight of the possible Drude part is small compared to the MIR spectral weight.

Figure5.10 presents the dependence of n^*_{eff} (Eq.5.5) on ω_c for different time-delays t. Here the dashed line presents the equilibrium values. The relative difference between the n^*_{eff} (following photo-excitation) and n^*_{eff} of the equilibrium (which is effectively negligible) increases up to $\approx$ 1.5 eV. For higher values of the cut-off frequency, the relative difference starts to decrease, signifying the contribution of the red-shift of the CT peak to the signal. Thus, for the following analysis of the time evolution of the photo-induced in-gap carrier density, we fix the cut-off frequency at 1.5 eV (choosing a lower value of the cut-off frequency gives qualitatively the same result). Our analysis reveals, that n^*_{eff} is strongly enhanced below the CT gap with increasing fluence, which is a result of transfer of spectral weight from higher energies to the MIR region.

Now, the photo-induced effective carrier density n^*_{eff} and their dynamics in the photon energy range of 0.5 -1.5 eV can be estimated as

$$n^{pI}_{eff}(t) = C\frac{2m^*_e V}{\pi e^2}\int_{0.5eV}^{1.5eV}[{\sigma_1}^{PI}(\omega,t)-\sigma^0_1(\omega)]d\omega \tag{5.6}$$

Here, ${\sigma_1}^{PI}(\omega,t)$ and $\sigma^0_1(\omega)$ are the real parts of the optical conductivity at a time delay t after excitation and in equilibrium, respectively. V is the unit cell volume (ucv), m^*_e is the electronic band mass, and C is a constant that takes into account also the contribution of the spectral weight at ω<0.5 eV.

Fig.5.11, depicts $n^{PI}_{eff}(t)$ for selected excitation densities (solid lines) (see Eq. 5.6). The recovery of n^{PI}_{eff} proceeds on the ps timescale and is found to be non-exponential even in the low-excitation density limit. The fluence dependence

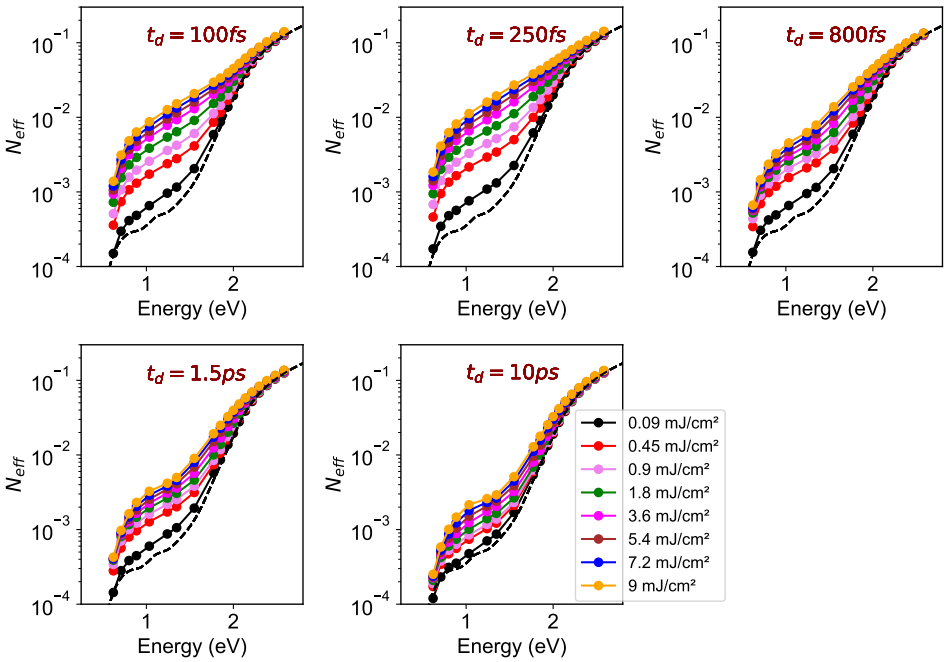

Figure 5.10: Effective number of carriers per Cu after UV photo-excitation for different time-delays and different excitation densities. The equilibrium values of the integral (Eq.5.5) are shown by the black dashed line.

reveals the speeding up of relaxation at high excitation densities, suggesting multi-particle recombination processes at high densities.

To understand the fluence dependence relaxation dynamics of the photo-induced carrier and discuss their possible recombination processes, we proceed with a simple rate equation analysis, considering linear and bi-molecular relaxation terms:

$$\frac{dn}{dt} = -\alpha n - \beta n^2 + n_0 \delta(t) \tag{5.7}$$

Here, α and β are fluence independent constants, and n_0 is the density of photo-generated e-h pairs. The analytical solution of Eq.5.7 is given by:

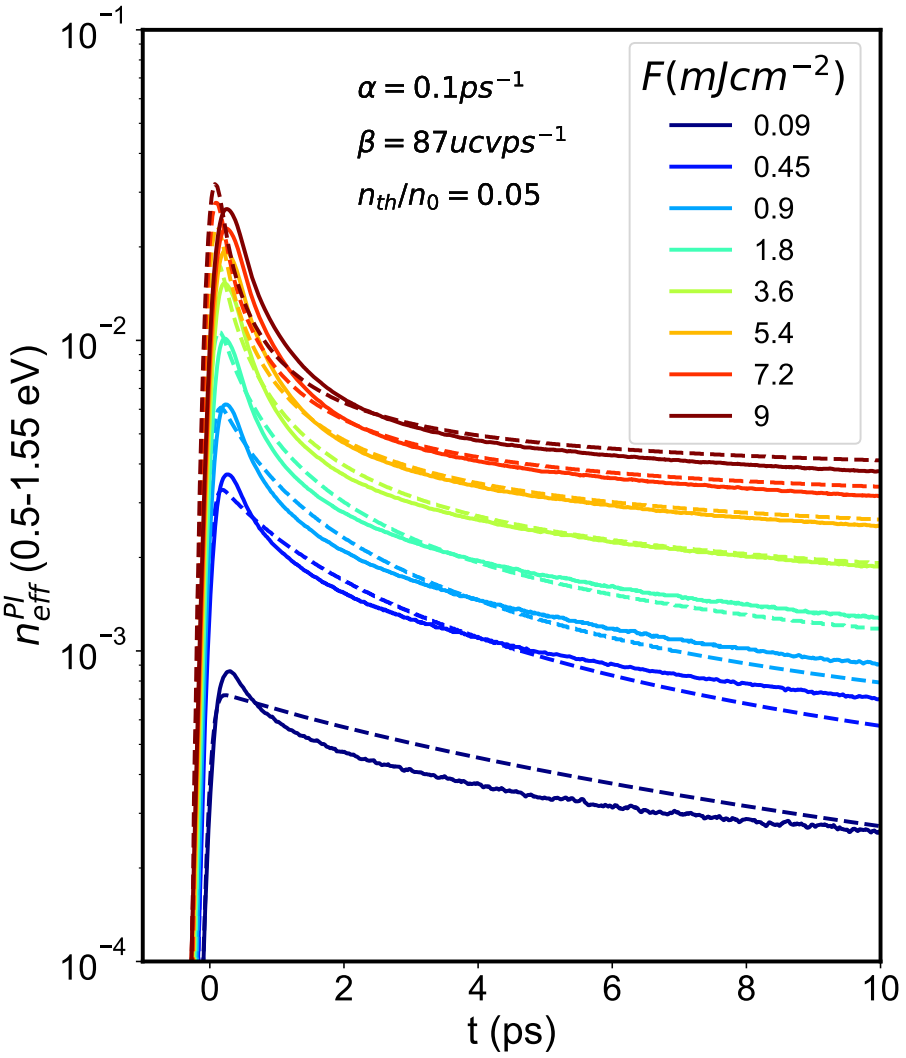

Figure 5.11: Excitation density dependence of the in-gap carrier dynamics. The solid lines present the experimental data, extracted using Eq.5.6 with C = 1. The dashed lines present a global fit using Eq. 5. The extracted fit parameters α and β are given in inset

$$n(t) = \frac{\frac{\alpha}{\beta}}{-1 + (1 + \frac{\frac{\alpha}{\beta}}{n_0 - n_{th}})e^{\alpha t}} + n_{th} \tag{5.8}$$

Here, n_{th} accounts for the signal at large time-delays, which can be attributed to "thermally" activated e-h pairs as a result of the heating-up of the antiferromagnetic background. The results of the global fit of the data with Eq.5.8, convoluted with the system response function, are shown by the dashed lines in Figure 5.11. We assume a constant ratio between n_{th} and n_0, e.g., if at large time delays the temperature increase is governed by the total specific heat. With n_{th}/n_0 =0.05 we obtain $\alpha = 0.1$ ps^{-1} and $\beta = 90$ ps^{-1} ucv.

While at low intensities the agreement between the fit and the data is only qualitative (as pointed out above, the dynamics is non-exponential even in the low-perturbation limit), the model captures the overall trend surprisingly well, especially given the fact that the excitation density is varied over two orders of magnitude, and α and β are kept independent on excitation density.

The absence of a pronounced free carrier response and the fact that the spectral shape of the photo-induced MIR absorption remains constant suggests that photo-excitation (at least in the weak to moderate excitation regime) results in weakly bound e-h pairs. Since the pump photon energy of $\approx$ 3 eV exceeds the $\approx$ 2 eV CT gap, the excess energy of the e-h pair is most likely transferred to phonons via rapid e-ph relaxation [166]. The resulting bound e-h pairs then relax on the picosecond timescale via geminate (i.e., with the electron-like and hole-like carriers being the product of the same primary photo-excitation) recombination (Fig. 5.12 **b**). The relaxation mechanism that is consistent with the above is the recently proposed recombination via multi-magnon emission

[167]. The characteristic relaxation rate $\alpha = 0.1$ ps^{-1}, obtained from the data, is indeed close to the theoretically estimated value [167] of 0.07 ps^{-1} for LCO.

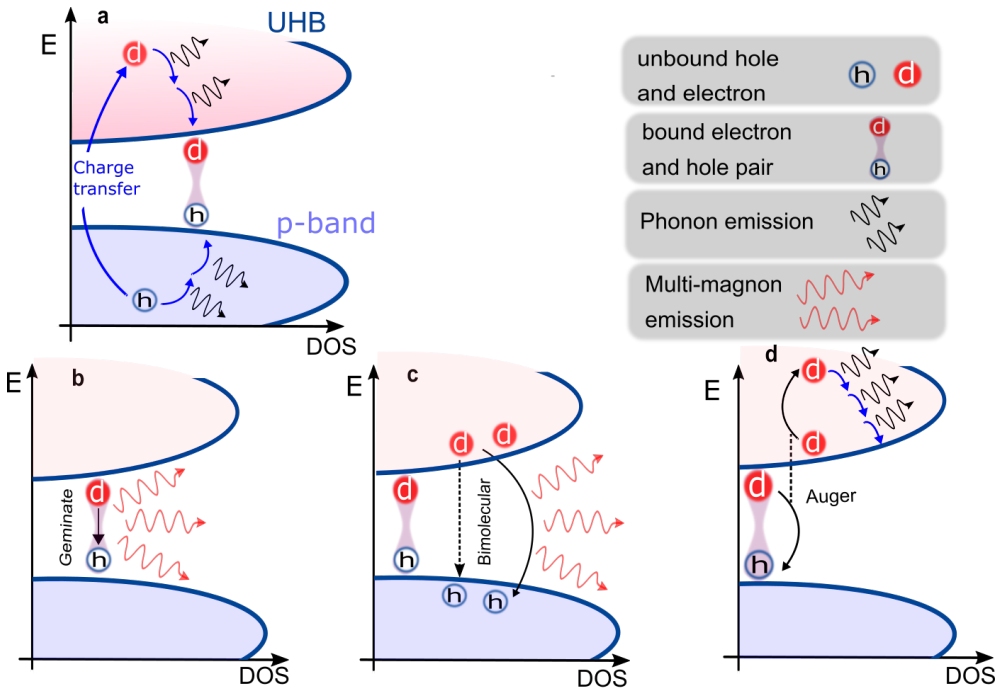

Figure 5.12: Schematic of the proposed relaxation processes. **a** Photo-excitation with photons of energy larger than the CT gap leads to unbound electrons and holes. These form bound e-h pairs of the < 100 fs timescale, with the excess energy rapidly transferred to the lattice [165]. d represents the doubly occupied site. At moderate excitation densities the relaxation proceeds via recombination of bound e-h pairs via multi-magnon emission **b**. At high densities the partial melting of the AFM background results in reduced binding, and is responsible for bi-molecular kinetics. It likely reflects the Auger type process **c**, where a bound pair recombines by transferring the excess energy to a neighboring unbound electron (or hole). The latter releases the excess energy to the lattice via rapid e-ph scattering. Alternatively, bi-molecular relaxation can also be a result of recombination of unbound pairs **d**.

Excitation density dependence, see Fig. 5.11, implies the bi-molecular processes become relevant at excitation densities of ≈ 0.02 e-h pairs/ucv with the extracted coefficient for the bi-molecular (non-geminate) recombination of $\beta = 90$ ucv/ps. At such excitation densities the magnetic excitations generated dur-

ing the recombination process suppress the underlying local AFM order. Since it is the local AFM order that is responsible for binding of e-h pairs, its partial melting results in a combination of bound and unbound e-h pairs. In this case, the bi-molecular recombination kinetics can be attributed to either of the two processes sketched in Fig.5.12 **c** and **d**. For long lime-delays n_{eff}^{PI} scales roughly linearly with excitation density, suggesting the increase in temperature on the 10 ps timescale being determined by the lattice specific heat. This suggests that it is the Auger type of process, sketched in Fig. 5.12 **d**, that is behind the observed bi-molecular kinetics.

Further evidence in support of the proposed scenario can be found in the observed excitation density dependence of the photo-induced MIR spectral weight and the CT gap parameters in Fig. 5.9 **c** and **d**. All of these display a change in slope at excitation density of $\approx$ 2 mJ/cm2, which equals to 2-3 e-h pairs per 100 unit cells. The corresponding absorbed energy of 40 - 60 meV/unit cell, when released to the magnetic excitations, is indeed close to the e-h binding energy of $J \approx 130$ meV, consistent with the proposed melting of the AFM background at high excitation densities being responsible for the observed bimolecular kinetics.

The observed lack of photo-induced metallicity up to highest excitation densities, the robust MIR response and the excitation density dependence of relaxation all suggest that importance of the local AFM order in undoped cuprates. Going beyond ultrafast physics in question, the results suggest the incoherent motion of doped carriers against the background of AFM spin fluctuations [138, 139] to be the origin of the MIR absorption in weakly doped cuprates.

5.3.5 Conclusion

In this chapter, we investigated the transient photo-doping phenomena of La_2CuO_4, the Mott insulating parent compound of the La-based cuprate high temperature superconductor. The transient state is studied by tracking the time-evolution of the broadband complex dielectric function over the spectral range of 0.5 – 2.6 eV by varying the excitation density over three order of magnitude. The changes in the complex dielectric function were analysed using a multi Lorentz and Drude-Lorentz model. The analysis reveal a pronounced renormalization of the CT gap, accompanied by the light-induced mid-gap absorption, resembling the evolution of optical properties by chemical doping. However, we demonstrate, that even at the highest excitation densities, where in the case of comparable chemical doping a metallic state is realized, photo-generated carriers remain largely bound in e-h pairs, underscoring the strength of the underlying antiferromagnetic (AFM) correlations. In addition, using simple rate equation analysis, we study that the fast and intensity independent relaxation dynamics at low to modest excitation densities which suggest that the localized e-h pairs relax through pair-wise recombination via multi-magnon emission. Furthermore, at high excitation densities bimolecular relaxation takes over, attributed to the partial melting of the AFM background.

CHAPTER 6

SUMMARY

Within the framework of this thesis, time-resolved optical spectroscopic techniques have been developed and implemented to study photo-induced dynamics in three different correlated materials- KI system YbB_{12}, CDW system $BaNi_2As_2$ and the parent compound of La-based high T_c superconductor, the AFM Mott insulator La_2CuO_4.

First topic present the transient reflectivity study in KI (see chapter 3). Measurement shows that photo-excited carrier relaxation dynamics is governed by the presence of low energy indirect gap due to hybridization between the localized magnetic moments and the conduction band electrons. Temperature dependence study further shows the change in the low energy electronic structure below 20 K which we attribute to the short range antiferromagnetic correlation between the local magnetic moments. In addition, results imply that the hybridization gap to be present up to the temperature of the order of $E_g/k_B \approx 200$ K and is extremely robust against electronic structure.

Furthermore, time-resolved study in CDW system $BaNi_2As_2$ - a non magnetic analogue of Fe-122 (Iron arsenide)- is presented where several oscillatory modes at low temperature all the way upto $\approx$ 150 K observed. Comparison of the observed modes with phonon dispersion calculations reveals that the dominant and strongly temperature dependent modes are attributed to the collective modes of the CDW while the weaker modes matches the $q = 0$ Raman active modes. The existence of the CDW order above the structural phase transition and their smooth evolution indicate charge-order driven nematicity in $BaNi_2As_2$ and may indeed trigger structural phase transition. Moreover, the excitation density dependence study shows no ultrafast collapse of the CDW up to excitation densities over an order of magnitude higher than in prototype Peierls systems [97, 98, 102], suggesting an unconventional microscopic mechanism.

Finally, in chapter 5, we presented the photo-doping phenomena in undoped parent compound La_2CuO_4 using ultrafast broadband spectroscopic technique. Earlier chemical doping studies strongly suggest the emergence of low energy electronic states in the MIR region which then eventually merge to the free carrier Drude response [135]. By exciting the compound with photon energies of 3 eV, above the charge transfer gap (2 eV), we studied the changes in the spectral range of 0.5 -2.6 eV. Results show the emergence of mid-gap absorption feature at 0.6 eV similar to chemical doping [135]. An evaluation of the data with multi-Lorentz and Drude-Lorentz model strongly suggest that increasing excitation density, the MIR peak does not merge with the free carrier peak, even at the highest photo-doping levels. Furthermore, by studying the carrier relaxation dynamics over large range of excitation densities (over three order of magnitude), the photo-generated carriers remain largely bound in electron-hole pairs and relaxation proceeds through pair wise recombination, underscoring the robustness

of the underlying electron correlation.

It follows that femtosecond pump-probe spectroscopy proves to be a powerful tool to investigate fundamental processes out of equilibrium. By examining the photo-induced changes and the relaxation processes on a fs to ps timescale, various emergent phenomena can be studied such as the collective amplitude modes in CDW system. Moreover, by varying the external parameters such as the temperature, doping/ pressure and studying the non-equilibrium dynamics one can study the underlying mechanisms of these phenomena. The work presented in this thesis are few examples. The application of ultrafast spectroscopy is rapidly growing and is being incorporated in various linear spectroscopic techniques (with additional temporal information) and will remain an important aspect for future research in correlated systems.

APPENDIX A

PHONON DISPERSION CALCULATION

Phonon dispersion calculations are performed by *Rolf Heid*[1] as a part of collaborative work. Lattice dynamics properties for the high-temperature tetragonal structure were calculated using the linear response or density-functional perturbation theory (DFPT) implemented in the mixed-basis pseudo-potential method [168–170]. The electron-ion interaction is described by norm-conserving pseudo-potentials, which were constructed following the descriptions of Hamann, Schlüter, Chiang [171] for Ba and Vanderbilt [172] for Ni and As, respectively. Semi-core states Ba-5p, Ni-3s, Ni-3p were included in the valence space.

In the mixed-basis approach, valence states are expanded in a combination of plane waves and local functions at atomic sites, which allows an efficient description of more localized components of the valence states. Here, plane waves with a cut-off for the kinetic energy of 22 Ry and local functions of p,d type for Ba and s, p, d type for Ni, respectively, were employed. Brillouin-zone integration was

[1] Institute of Quantum Materials and Technologies, Karlsruhe Institute of Technology

performed by sampling a tetragonal $16 \times 16 \times 8$ k-point mesh in conjunction with a Gaussian broadening of 50 meV. The exchange-correlation functional was represented by the general-gradient approximation in the Perdew-Burke-Ernzerhof form [173].

Phonon dispersions along the [100] and [101] directions of the tetragonal structure, shown in Figure 4.10, were obtained by Fourier-interpolation of dynamical matrices calculated by DFPT on a tetragonal $8 \times 8 \times 2$ mesh. A denser 16 x 1 x 1 mesh was used to better resolve the position of the instability in the [100] direction. Structural parameters were taken from room-temperature measurements after [93].

We find similar phonon branches as in a previous work [174], with one notable exception: there occurs an instability in an optical branch near the critical wavevector of the I-CDW of (0.28,0,0), which was missed in the previous study. This instability only shows up, when a sufficiently dense mesh for the calculation of the dynamical matrices is used, and is easily overlooked otherwise.

APPENDIX B

Reflection-Transmission (RT-) Method

Using the Fresnel-equations [152, 153], for a thin film on a thick substrate, the complex refractive index of the sample was calculated over 0.5 eV – 2.5 eV spectral range. Considering the coherent light propagating through the thin film, a system of equations describing the reflection and transmission through the two-layer system (R_{theo} and T_{theo}) was derived, inverted and numerically solved for n and k by inserting the measured equilibrium R_{exp} and T_{exp} for the sample and bare substrate:

$$\begin{pmatrix} R_{theo}(n,k) - R_{exp} \\ T_{theo}(n,k) - T_{exp} \end{pmatrix} ! = \begin{pmatrix} 0 \\ 0 \end{pmatrix}$$

This so-called RT-method is frequently used to characterize and numerically evaluate the optical constants of thin film samples [175, 176]. This variational approach was used also for extracting the time evolution of the complex di-

electric function (ϵ) when evaluating the nonequilibrium data. Here, for a selected photon energy, using the measured dielectric function of the substrate, the known film thickness, the result (measured $R + \Delta R$ and $T + \Delta T$ at a given time delay) is simulated by varying n and k (or ϵ_1 and ϵ_2) of the film, starting from their equilibrium values (R and T). The method is then performed for each time delay.

Author contributions

Here, detailed contributions of the author for each chapter are listed and highlighted.

Time-resolved study in Kondo Insulator YbB_{12} (Chapter 3):

- YbB_{12} single crystal is grown by F. Iga, T. Takabatake and H. Okamura;
- *Own contribution*: Conceiving, Planning, designing and testing of the time-resolved pump-probe setup in reflection geometry for ultrafast study of Kondo Insulator YbB_{12}, under the supervision of Prof. J. Demsar. Performing temperature and fluence dependent study and extraction of the experimental data. In-depth analysis of the reflectivity data using Phenomenological Rothwarf and Taylor model. Preparation of the manuscript [30] together with Prof. J. Demsar with contributions from all coauthors.

Time-resolved study in an unconventional CDW system $BaNi_2As_2$ (Chapter 4):

- Amir A. Haghighirad grew the single crystal samples and performed EDX measurement;
- R. Heid performed phonon dispersion calculations;
- Y. Yao performed Raman studies under supervision of Prof. M. Le Tacon;
- *Own contribution*: Planning, designing and testing of the time-resolved pump-probe setup for ultrafast study of $BaNi_2As_2$ under the supervision of Prof. J. Demsar. Performing ultrafast optical spectroscopy measurements together with V. Grigorev, T. Dong and A. Mejas. Analysis of the experimental data together with V. Grigorev and Prof. J. Demsar. Preparation of the manuscript [72] together with V. Grigorev and Prof. J. Demsar with contribution from all authors.

Photo-doping of La_2CuO_4 (Chapter 5):

- G. Logvenov and I. Bozovic grew the La_2CuO_4 thin film samples;
- M. Beyer and M. Obergfell performed the ultrafast broadband measurement under the supervision of Prof. J. Demsar;
- Z. Lenarcic and P. Prelovsek provided the theoretical support;
- *Own contribution*: Extensive analysis of the experimetal data obtained from optical broadband setup (utilizing optical-parametric-amplifier) under the supervision of Prof. J. Demsar. Preparation of the manuscript (*in preparation*) together with Prof. J. Demsar with contribution from all coauthors.

BIBLIOGRAPHY

[1] G. Kotliar and D. Vollhardt. "Strongly Correlated Materials: Insights From Dynamical Mean-Field Theory" (2004).

[2] E. Morosan et al. "Strongly correlated materials". *Advanced Materials* **24** (2012), pp. 4896–4923.

[3] H Kamerlingh Onnes. "Further experiments with Liquid Helium. D. On the change of Electrical Resistance of Pure Metals at very low Temperatures, etc. V. The Disappearance of the resistance of mercury". *Koninklijke Nederlandse Akademie van Wetenschappen Proceedings Series B Physical Sciences* **14** (1911), pp. 113–115.

[4] J. Bardeen, L. N. Cooper, and J. R. Schrieffer. "Theory of superconductivity". *Physical review* **108** (1957), p. 1175.

[5] R. E. Peierls. *Quantum Theory of Solids*. New York: Oxford University, 1955.

[6] B. Becker et al. "Strongly coupled charge-density wave transition in single-crystal $Lu_5Ir_4Si_{10}$". *Phys. Rev. B* **59** (11 1999), pp. 7266–7269. DOI: 10.1103/PhysRevB.59.7266.

[7] F. Galli et al. "Charge-Density-Wave Transitions in the Local-Moment Magnet $Er_5Ir_4Si_{10}$". *Phys. Rev. Lett.* **85** (1 2000), pp. 158–161. DOI: 10.1103/PhysRevLett.85.158.

[8] C.-W. Chen, J. Choe, and E Morosan. "Charge density waves in strongly correlated electron systems". *Reports on Progress in Physics* **79** (2016), p. 084505. DOI: 10.1088/0034-4885/79/8/084505.

[9] F. Steglich et al. "Superconductivity in the Presence of Strong Pauli Paramagnetism: $CeCu_2Si_2$". *Phys. Rev. Lett.* **43** (25 1979), pp. 1892–1896. DOI: 10.1103/PhysRevLett.43.1892.

[10] J. G. Bednorz and K. A. Müller. "Possible highT c superconductivity in the BaLaCuO system". *Zeitschrift für Physik B Condensed Matter 1986 64:2* **64** (1986), pp. 189–193. DOI: 10.1007/BF01303701.

[11] Y. Kamihara et al. "Iron-Based Layered Superconductor La[$O_{1-x}F_x$]FeAs ($x = 0.05 - 0.12$) with Tc = 26 K". *Journal of the American Chemical Society* **130** (2008), pp. 3296–3297. DOI: 10.1021/ja800073m.

[12] F.-C. Hsu et al. "Superconductivity in the PbO-type structure α-FeSe". *Proceedings of the National Academy of Sciences* **105** (2008), pp. 14262–14264. DOI: 10.1073/pnas.0807325105.

[13] X. Wang et al. "The superconductivity at 18 K in LiFeAs system". *Solid State Communications* **148** (2008), pp. 538–540. DOI: 10.1016/j.ssc.2008.09.057.

[14] D. R. Parker et al. "Structure, antiferromagnetism and superconductivity of the layered iron arsenide NaFeAs". *Chem. Commun.* (16 2009), pp. 2189–2191. DOI: 10.1039/B818911K.

[15] A. F. Wang et al. "Phase diagram and calorimetric properties of $NaFe_{1-x}Co_xAs$". *Phys. Rev. B* **85** (22 2012), p. 224521. DOI: 10.1103/PhysRevB.85.224521.

[16] C. V. Shank and E. P. Ippen. "Subpicosecond kilowatt pulses from a mode-locked cw dye laser". *Applied Physics Letters* **24** (2003), p. 373. DOI: 10.1063/1.1655222.

[17] T. B. Norris. "Femtosecond pulse amplification at 250 kHz with a Ti:sapphire regenerative amplifier and application to continuum generation". *Optics Letters, Vol. 17, Issue 14, pp. 1009-1011* **17** (1992), pp. 1009–1011. DOI: 10.1364/OL.17.001009.

[18] R. H. Groeneveld, R. Sprik, and A. Lagendijk. "Femtosecond spectroscopy of electron-electron and electron-phonon energy relaxation in Ag and Au". *Physical Review B* **51** (1995), p. 11433.

[19] (). DOI: 10.1088/0953-8984/18/16/r01.

[20] S. D. Brorson. "Femtosecond thermomodulation measurements of transport and relaxation in metals and superconductors" (1990).

[21] J Demsar and T Dekorsy. *Carrier dynamics in bulk semiconductors and metals after ultrashort pulse excitation*. Ed. by R. P. Prasankumar and A. J. Taylor. CRC press, 2012.

[22] S. Anisimov, B. Kapeliovich, T. Perelman, et al. "Electron emission from metal surfaces exposed to ultrashort laser pulses". *Zh. Eksp. Teor. Fiz* **66** (1974), pp. 375–377.

[23] M. Kaganov, E. Lifshitz, and L. Tanatarov. "Relaxation between electrons and the crystalline lattice". *Soviet Physics-JETP* **4** (1957), pp. 173–178.

[24] P. B. Allen. "Theory of thermal relaxation of electrons in metals". *Physical review letters* **59** (1987), p. 1460.

[25] K. Ahn et al. "Ultrafast quasiparticle relaxation dynamics in normal metals and heavy-fermion materials". *Physical Review B* **69** (2004), p. 045114.

[26] W. de Haas, J. de Boer, and G. van dën Berg. "The electrical resistance of gold, copper and lead at low temperatures". *Physica* **1** (1934), pp. 1115–1124. DOI: https://doi.org/10.1016/S0031-8914(34)80310-2.

[27] G. J. van den Berg. "Anomalies in Dilute Metallic Solutions of Transition Metals". *Low Temperature Physics LT9*. Ed. by J. G. Daunt et al. Boston, MA: Springer US, 1965, pp. 955–984.

[28] J Kondo and K Yamaji. "Progr. theor". *Phys.(Kyoto)* **32** (1964), p. 37.

[29] P. W. Anderson. "Localized Magnetic States in Metals". *Phys. Rev.* **124** (1 1961), pp. 41–53. DOI: 10.1103/PhysRev.124.41.

[30] A. R. Pokharel et al. "Robust hybridization gap in the Kondo insulator YbB_{12} probed by femtosecond optical spectroscopy". *Phys. Rev. B* **103** (11 2021), p. 115134. DOI: 10.1103/PhysRevB.103.115134.

[31] G. Zwicknagl. "Quasi-particles in heavy fermion systems". *Advances in Physics* **41** (1992), pp. 203–302. DOI: 10.1080/00018739200101503. eprint: https://doi.org/10.1080/00018739200101503.

[32] G. R. Stewart. *Rev. Mod. Phys.* **56** (4 1984), p. 755. DOI: 10.1103/RevModPhys.56.755.

[33] P. S. Riseborough. *Advances in Physics* **49** (2000), pp. 257–320. DOI: 10.1080/000187300243345.

[34] L. Degiorgi. *Rev. Mod. Phys.* **71** (3 1999), pp. 687–734. DOI: 10.1103/RevModPhys.71.687.

[35] P. Coleman. *Handbook of Magnetism and Advanced Magnetic Materials*. American Cancer Society, 2007. DOI: 10.1002/9780470022184.hmm105.

[36] A. Amato. "Heavy-fermion systems studied by μSR technique". *Rev. Mod. Phys.* **69** (4 1997), pp. 1119–1180. DOI: 10.1103/RevModPhys.69.1119.

[37] F. Strigari. "Hybridization and crystal-field effects in Kondo insulators studied by means of core-level spectroscopy". PhD thesis. Universität zu Köln, 2015.

[38] M. A. Ruderman and C. Kittel. *Phys. Rev.* **96** (1 1954), pp. 99–102. DOI: 10.1103/PhysRev.96.99.

[39] T. Kasuya. *Progress of Theoretical Physics* **16** (1956), pp. 45–57. DOI: 10.1143/PTP.16.45.

[40] K. Yosida. *Phys. Rev.* **106** (5 1957), pp. 893–898. DOI: 10.1103/PhysRev.106.893.

[41] P. S. Riseborough. "Heavy fermion semiconductors". **49** (2010), pp. 257–320. DOI: 10.1080/000187300243345.

[42] H. Okamura et al. *Journal of the Physical Society of Japan* **74** (2005), pp. 1954–1957. DOI: 10.1143/jpsj.74.1954.

[43] Y. Takeda et al. *Phys. Rev. B* **73** (3 2006), p. 033202. DOI: 10.1103/PhysRevB.73.033202.

[44] K. Hagiwara et al. English. *Nature Communications* **7** (2016). DOI: 10.1038/ncomms12690.

[45] F. Iga, N. Shimizu, and T. Takabatake. *Journal of Magnetism and Magnetic Materials* **177-181** (1998), pp. 337 –338. DOI: https://doi.org/10.1016/S0304-8853(97)00493-9.

[46] M. Okawa et al. *Phys. Rev. B* **92** (16 2015), p. 161108. DOI: 10.1103/PhysRevB.92.161108.

[47] Z. Xiang et al. *Science* **362** (2018), pp. 65–69. DOI: 10.1126/science.aap9607.

[48] Y. Xu et al. *Phys. Rev. Lett.* **116** (24 2016), p. 246403. DOI: 10.1103/PhysRevLett.116.246403.

[49] O. Erten et al. *Phys. Rev. Lett.* **119** (5 2017), p. 057603. DOI: 10.1103/PhysRevLett.119.057603.

[50] R. Peters, T. Yoshida, and N. Kawakami. *Phys. Rev. B* **100** (8 2019), p. 085124. DOI: 10.1103/PhysRevB.100.085124.

[51] J. Demsar et al. *Phys. Rev. Lett.* **91** (2 2003), p. 027401. DOI: 10.1103/PhysRevLett.91.027401.

[52] J. Demsar et al. *Phys. Rev. Lett.* **96** (3 2006), p. 037401. DOI: 10.1103/PhysRevLett.96.037401.

[53] K. S. Burch et al. *Phys. Rev. Lett.* **100** (2 2008), p. 026409. DOI: 10.1103/PhysRevLett.100.026409.

[54] J. Demsar et al. *Phys. Rev. B* **80** (8 2009), p. 085121. DOI: 10.1103/PhysRevB.80.085121.

[55] E. E. M. Chia et al. *Phys. Rev. B* **84** (17 2011), p. 174412. DOI: 10.1103/PhysRevB.84.174412.

[56] J. Zhang et al. *Phys. Rev. B* **97** (15 2018), p. 155119. DOI: 10.1103/PhysRevB.97.155119.

[57] A. Rothwarf and B. N. Taylor. *Phys. Rev. Lett.* **19** (1 1967), pp. 27–30. DOI: 10.1103/PhysRevLett.19.27.

[58] V. V. Kabanov, J. Demsar, and D. Mihailovic. *Phys. Rev. Lett.* **95** (14 2005), p. 147002. DOI: 10.1103/PhysRevLett.95.147002.

[59] J. Demsar et al. *Phys. Rev. Lett.* **91** (26 2003), p. 267002. DOI: 10.1103/PhysRevLett.91.267002.

[60] M. Beck et al. *Phys. Rev. Lett.* **107** (17 2011), p. 177007. DOI: 10.1103/PhysRevLett.107.177007.

[61] J. Demsar. *Journal of Low Temperature Physics* (2020).

[62] H. Schaefer, V. V. Kabanov, and J. Demsar. "Collective modes in quasi-one-dimensional charge-density wave systems probed by femtosecond time-resolved optical studies". *Phys. Rev. B* **89** (4 2014), p. 045106. DOI: 10.1103/PhysRevB.89.045106.

[63] W. H. Parker. *Phys. Rev. B* **12** (9 1975), pp. 3667–3672. DOI: 10.1103/PhysRevB.12.3667.

[64] B. Bucher et al. *Physica B: Condensed Matter* **199-200** (1994), pp. 489 –491. DOI: https://doi.org/10.1016/0921-4526(94)91879-1.

[65] X. Zhang et al. *Phys. Rev. X* **3** (1 2013), p. 011011. DOI: 10.1103/PhysRevX.3.011011.

[66] S. Winerl and H. Okamura. *unpublished* ().

[67] M. Beck et al. *Phys. Rev. B* **95** (8 2017), p. 085106. DOI: 10.1103/PhysRevB.95.085106.

[68] D. J. Chadi and M. L. Cohen. "Electronic band structures and charge densities of NbC and NbN". *Phys. Rev. B* **10** (2 1974), pp. 496–500. DOI: 10.1103/PhysRevB.10.496.

[69] M. Heinecke et al. "Quantum oscillations and the Fermi surface of LuBI2". *Z. Phys. B* **98** (1995), pp. 231–237. DOI: 10.1007/BF01324529.

[70] G. Grüner. "The dynamics of charge-density waves". *Rev. Mod. Phys.* **60** (4 1988), pp. 1129–1181. DOI: 10.1103/RevModPhys.60.1129.

[71] G. Grüner. *Density Waves in Solids*. Massachusetts: Addison - Wesley Publishing Company, 1994.

[72] A. R. Pokharel et al. "Dynamics of collective modes in an unconventional charge density wave system BaNi2As2". *Communications Physics 2022 5:1* **5** (1 2022), pp. 1–8. DOI: 10.1038/s42005-022-00919-x.

[73] K Rossnagel. "On the origin of charge-density waves in select layered transition-metal dichalcogenides". *Journal of Physics: Condensed Matter* **23** (2011), p. 213001. DOI: 10.1088/0953-8984/23/21/213001.

[74] J Lindhard. "ON THE PROPERTIES OF A GAS OF CHARGED PARTICLES". *Kgl. Danske Videnskab. Selskab Mat.-fys. Medd.* **28** (1954).

[75] W. Kohn. "Image of the Fermi Surface in the Vibration Spectrum of a Metal". *Phys. Rev. Lett.* **2** (9 1959), pp. 393–394. DOI: 10.1103/PhysRevLett.2.393.

[76] X. Zhu et al. “Misconceptions associated with the origin of charge density waves”. *Advances in Physics: X* **2** (2017), pp. 622–640. DOI: 10.1080/23746149.2017.1343098. eprint: https://doi.org/10.1080/23746149.2017.1343098.

[77] E. J. Woll and W. Kohn. “Images of the Fermi Surface in Phonon Spectra of Metals”. *Phys. Rev.* **126** (5 1962), pp. 1693–1697. DOI: 10.1103/PhysRev.126.1693.

[78] J. Chaussy et al. “Phase transitions in NbSe3”. *Solid State Communications* **20** (1976), pp. 759–763. DOI: https://doi.org/10.1016/0038-1098(76)90289-1.

[79] P. Gressier, L. Guemas, and A. Meerschaut. “Preparation and structure of ditantalum iodide octaselenide, Ta_2ISe_8”. *Acta Crystallographica Section B* **38** (1982), pp. 2877–2879. DOI: 10.1107/S0567740882010176.

[80] M Sato et al. “Neutron inelastic scattering and X-ray structural study of the charge-density-wave state in Ksub0.3/subMoOsub3/sub”. *Journal of Physics C: Solid State Physics* **18** (1985), pp. 2603–2614. DOI: 10.1088/0022-3719/18/13/007.

[81] J. M. Tranquada et al. “Evidence for stripe correlations of spins and holes in copper oxide superconductors”. *Nature 1995 375:6532* **375** (1995), pp. 561–563. DOI: 10.1038/375561a0.

[82] T. Wu et al. “Magnetic-field-induced charge-stripe order in the high-temperature superconductor YBa2Cu3Oy”. *Nature 2011 477:7363* **477** (2011), pp. 191–194. DOI: 10.1038/nature10345.

[83] K. Y. Shin et al. “Charge density wave formation in R_2Te_5 (R = Nd, Sm, and Gd)”. *Phys. Rev. B* **77** (16 2008), p. 165101. DOI: 10.1103/PhysRevB.77.165101.

[84] R. G. Moore et al. “Fermi surface evolution across multiple charge density wave transitions in $ErTe_3$”. *Phys. Rev. B* **81** (7 2010), p. 073102. DOI: 10.1103/PhysRevB.81.073102.

[85] S. K. Goh et al. “Ambient Pressure Structural Quantum Critical Point in the Phase Diagram of $(Ca_xSr_{1-x})_3Rh_4Sn_{13}$”. *Phys. Rev. Lett.* **114** (9 2015), p. 097002. DOI: 10.1103/PhysRevLett.114.097002.

[86] L. E. Klintberg et al. “Pressure- and Composition-Induced Structural Quantum Phase Transition in the Cubic Superconductor $(Sr, Ca)_3Ir_4Sn_{13}$”. *Phys. Rev. Lett.* **109** (23 2012), p. 237008. DOI: 10.1103/PhysRevLett.109.237008.

[87] S. Lee et al. “Unconventional Charge Density Wave Order in the Pnictide Superconductor $Ba(Ni_{1-x}Co_x)_2As_2$)”. *Phys. Rev. Lett.* **122** (14 2019), p. 147601. DOI: 10.1103/PhysRevLett.122.147601.

[88] F Ronning et al. "The first order phase transition and superconductivity in $BaNi_2As_2$ single crystals". *Journal of Physics: Condensed Matter* **20** (2008), p. 342203. DOI: 10.1088/0953-8984/20/34/342203.

[89] K. Kudo et al. "Giant Phonon Softening and Enhancement of Superconductivity by Phosphorus Doping of $BaNi_2As_2$". *Phys. Rev. Lett.* **109** (9 2012), p. 097002. DOI: 10.1103/PhysRevLett.109.097002.

[90] C. Eckberg et al. "Sixfold enhancement of superconductivity in a tunable electronic nematic system". *Nature Physics* **16** (2020), pp. 346–350. DOI: 10.1038/s41567-019-0736-9.

[91] G. Ghiringhelli et al. "Long-Range Incommensurate Charge Fluctuations in $(Y,Nd)Ba_2Cu_3O_{6+x}$". *Science* **337** (2012), pp. 821–825. DOI: 10.1126/science.1223532.

[92] S. Lee et al. "Multiple Charge Density Waves and Superconductivity Nucleation at Antiphase Domain Walls in the Nematic Pnictide $Ba_{1-x}Sr_xNi_2As_2$". *Phys. Rev. Lett.* **127** (2 2021), p. 027602. DOI: 10.1103/PhysRevLett.127.027602.

[93] M. Merz et al. "Rotational symmetry breaking at the incommensurate charge-density-wave transition in $Ba(Ni,Co)_2(As,P)_2$: Possible nematic phase induced by charge/orbital fluctuations". *Phys. Rev. B* **104** (18 2021), p. 184509. DOI: 10.1103/PhysRevB.104.184509.

[94] Z. G. Chen et al. "Origin of the structural phase transition in $BaNi_2As_2$ at 130 K: A combined study of optical spectroscopy and band structure calculations". *Phys. Rev. B* **80** (9 2009), p. 094506. DOI: 10.1103/PhysRevB.80.094506.

[95] Z. G. Chen, W. Z. Hu, and N. L. Wang. "Different nature of instabilities in $BaFe_2As_2$ and $BaNi_2As_2$ as revealed by optical spectroscopy". *physica status solidi (b)* **247** (2010), pp. 495–499. DOI: https://doi.org/10.1002/pssb.200983069.

[96] J. Demsar et al. "Femtosecond snapshots of gap-forming charge-density-wave correlations in quasi-two-dimensional dichalcogenides $1T-TaS_2$ and $2H-TaSe_2$". *Phys. Rev. B* **66** (4 2002), p. 041101. DOI: 10.1103/PhysRevB.66.041101.

[97] H. Schäfer et al. "Disentanglement of the Electronic and Lattice Parts of the Order Parameter in a 1D Charge Density Wave System Probed by Femtosecond Spectroscopy". *Phys. Rev. Lett.* **105** (6 2010), p. 066402. DOI: 10.1103/PhysRevLett.105.066402.

[98] H. Schaefer et al. "Dynamics of charge density wave order in the quasi one dimensional conductor $(TaSe_4)_2I$ probed by femtosecond optical spectroscopy". *The European Physical Journal Special Topics* **222** (2013), pp. 1005–1016. DOI: 10.1140/epjst/e2013-01902-4.

[99] T. E. Stevens, J. Kuhl, and R. Merlin. "Coherent phonon generation and the two stimulated Raman tensors". *Phys. Rev. B* **65** (14 2002), p. 144304. DOI: 10.1103/PhysRevB.65.144304.

[100] D. Dominko et al. "Detection of charge density wave ground state in granular thin films of blue bronze $\mathbf{K}_{0.3}MoO_3$ by femtosecond spectroscopy". *Journal of Applied Physics* **110** (2011), p. 014907. DOI: 10.1063/1.3606418.

[101] A. Tomeljak et al. "Dynamics of Photoinduced Charge-Density-Wave to Metal Phase Transition in $\mathbf{K}_{0.3}MoO_3$". *Phys. Rev. Lett.* **102** (6 2009), p. 066404. DOI: 10.1103/PhysRevLett.102.066404.

[102] R. Yusupov et al. "Coherent dynamics of macroscopic electronic order through a symmetry breaking transition". *Nature Physics* **6** (2010), pp. 681–684. DOI: 10.1038/nphys1738.

[103] L. Stojchevska et al. "Mechanisms of nonthermal destruction of the superconducting state and melting of the charge-density-wave state by femtosecond laser pulses". *Phys. Rev. B* **84** (18 2011), p. 180507. DOI: 10.1103/PhysRevB.84.180507.

[104] A. S. Sefat et al. "Structure and anisotropic properties of $BaFe_{2-x}Ni_xAs_2$ ($x = 0$, 1, and 2) single crystals". *Phys. Rev. B* **79** (9 2009), p. 094508. DOI: 10.1103/PhysRevB.79.094508.

[105] J. Menéndez and M. Cardona. "Temperature dependence of the first-order Raman scattering by phonons in Si, Ge, and $\alpha-$Sn: Anharmonic effects". *Phys. Rev. B* **29** (4 1984), pp. 2051–2059. DOI: 10.1103/PhysRevB.29.2051.

[106] H. J. Zeiger et al. "Theory for displacive excitation of coherent phonons". *Phys. Rev. B* **45** (2 1992), pp. 768–778. DOI: 10.1103/PhysRevB.45.768.

[107] D. Dominko et al. "Static and dynamic properties of low-temperature order in the one-dimensional semiconductor $(NbSe_4)_3I$". *Phys. Rev. B* **94** (10 2016), p. 104113. DOI: 10.1103/PhysRevB.94.104113.

[108] M. J. Rice. "Organic Linear Conductors as Systems for the Study of Electron-Phonon Interactions in the Organic Solid State". *Phys. Rev. Lett.* **37** (1 1976), pp. 36–39. DOI: 10.1103/PhysRevLett.37.36.

[109] V. A. Golovko and A. P. Levanyuk. "Light scattering and the dispersion of susceptibilities in an incommensurate phase". *Zh. Eksp. Teor. Fiz.* **81** (1981), pp. 2296–2313.

[110] M. D. Thomson et al. "Phase-channel dynamics reveal the role of impurities and screening in a quasi-one-dimensional charge-density wave system". *Scientific Reports* **7** (2017), p. 2039. DOI: 10.1038/s41598-017-02198-x.

[111] M. Schubert et al. "Collective Modes and Structural Modulation in Ni-Mn-Ga(Co) Martensite Thin Films Probed by Femtosecond Spectroscopy and Scanning Tunneling Microscopy". *Phys. Rev. Lett.* **115** (7 2015), p. 076402. DOI: 10.1103/PhysRevLett.115.076402.

[112] V. Gnezdilov et al. "Anomalous optical phonons in FeTe chalcogenides: Spin state, magnetic order, and lattice anharmonicity". *Phys. Rev. B* **83** (24 2011), p. 245127. DOI: 10.1103/PhysRevB.83.245127.

[113] Y. J. Um et al. "Anomalous dependence of c-axis polarized Fe B_{1g} phonon mode with Fe and Se concentrations in $Fe_{1+y}Te_{1-x}Se_x$". *Phys. Rev. B* **85** (6 2012), p. 064519. DOI: 10.1103/PhysRevB.85.064519.

[114] Y. J. Um et al. "Superconductivity-induced phonon renormalization on $NaFe_{1-x}Co_xAs$". *Phys. Rev. B* **89** (18 2014), p. 184510. DOI: 10.1103/PhysRevB.89.184510.

[115] K. W. Kim et al. "Ultrafast transient generation of spin-density-wave order in the normal state of BaFe2As2 driven by coherent lattice vibrations". *Nature Materials* **11** (2012), pp. 497–501. DOI: 10.1038/nmat3294.

[116] Y. Yao et al. "An electronic nematic liquid in BaNi2As2". *Nature Communications 2022 13:1* **13** (1 2022), pp. 1–9. DOI: 10.1038/s41467-022-32112-7.

[117] I. Bozovic et al. "Long-lived coherent acoustic waves generated by femtosecond light pulses". *Phys. Rev. B* **69** (13 2004), p. 132503. DOI: 10.1103/PhysRevB.69.132503.

[118] J. Demsar, familyi=c., given=K., giveni=K., „ and D. Mihailovic. "Single Particle and Collective Excitations in the One-Dimensional Charge Density Wave Solid $K_{0.3}MoO_3$ Probed in Real Time by Femtosecond Spectroscopy". *Phys. Rev. Lett.* **83** (4 1999), pp. 800–803. DOI: 10.1103/PhysRevLett.83.800.

[119] M. Obergfell and J. Demsar. "Tracking the Time Evolution of the Electron Distribution Function in Copper by Femtosecond Broadband Optical Spectroscopy". *Phys. Rev. Lett.* **124** (3 2020), p. 037401. DOI: 10.1103/PhysRevLett.124.037401.

[120] N. Kurita et al. "Low-Temperature Magnetothermal Transport Investigation of a Ni-Based Superconductor $BaNi_2As_2$: Evidence for Fully Gapped Superconductivity". *Phys. Rev. Lett.* **102** (14 2009), p. 147004. DOI: 10.1103/PhysRevLett.102.147004.

[121] T. Noda et al. "Orbital-Dependent Band Renormalization in $BaNi_2(As_{1x}P_x)_2$ (x = 0.00 and 0.092)". *Journal of the Physical Society of Japan* **86** (2017), p. 064708. DOI: 10.7566/JPSJ.86.064708.

[122] D. Khomskii and T Mizokawa. “Orbitally induced Peierls state in spinels”. *Physical review letters* **94** (2005), p. 156402. DOI: 10.1103/PhysRevLett.94.156402.

[123] S. V. Streltsov and D. I. Khomskii. “Orbital-dependent singlet dimers and orbital-selective Peierls transitions in transition-metal compounds”. *Phys. Rev. B* **89** (16 2014), 161112(R). DOI: 10.1103/PhysRevB.89.161112.

[124] K. Kudo, M. Takasuga, and M. Nohara. “Copper Doping of BaNi _{2} As _{2}: Giant Phonon Softening and Superconductivity Enhancement”. *arXiv preprint arXiv:1704.04854* (2017).

[125] Y. Yao et al. “An electronic nematic liquid in BaNi2As2”. *Nature communications* **13** (2022), pp. 1–9.

[126] C. Meingast et al. “Charge-density-wave transitions, phase diagram, soft phonon and possible electronic nematicity: a thermodynamic investigation of BaNi2 (As, P) 2”. *arXiv preprint arXiv:2207.02294* (2022).

[127] M. Bayer. “Photo-Doping Phenomena in the High-Temperature Superconductor $La_{2-x}Sr_xCuO_4$”. PhD thesis. Universität Konstanz, 2011.

[128] N. F. Mott. “The Basis of the Electron Theory of Metals, with Special Reference to the Transition Metals”. *Proceedings of the Physical Society. Section A* **62** (1949), pp. 416–422. DOI: 10.1088/0370-1298/62/7/303.

[129] M. Imada, A. Fujimori, and Y. Tokura. “Metal-insulator transitions”. *Rev. Mod. Phys.* **70** (4 1998), pp. 1039–1263. DOI: 10.1103/RevModPhys.70.1039.

[130] J. Hubbard and B. H. Flowers. “Electron correlations in narrow energy bands”. *Proceedings of the Royal Society of London. Series A. Mathematical and Physical Sciences* **276** (1963), pp. 238–257. DOI: 10.1098/rspa.1963.0204.

[131] J. Hubbard and B. H. Flowers. “Electron correlations in narrow energy bands. II. The degenerate band case”. *Proceedings of the Royal Society of London. Series A. Mathematical and Physical Sciences* **277** (1964), pp. 237–259. DOI: 10.1098/rspa.1964.0019.

[132] J. Kanamori. “Electron Correlation and Ferromagnetism of Transition Metals”. *Progress of Theoretical Physics* **30** (1963), pp. 275–289. DOI: 10.1143/PTP.30.275. eprint: https://academic.oup.com/ptp/article-pdf/30/3/275/5278869/30-3-275.pdf.

[133] J. Zaanen, G. A. Sawatzky, and J. W. Allen. “Band gaps and electronic structure of transition-metal compounds”. *Phys. Rev. Lett.* **55** (4 1985), pp. 418–421. DOI: 10.1103/PhysRevLett.55.418.

[134] H. Hosono et al. **16** (2015), p. 033503. DOI: 10.1088/1468-6996/16/3/033503.

[135] S. Uchida et al. "Optical spectra of $La_{2-x}Sr_xCuO_4$: Effect of carrier doping on the electronic structure of the CuO_2 plane". *Phys. Rev. B* **43** (10 1991), pp. 7942–7954. DOI: 10.1103/PhysRevB.43.7942.

[136] A. S. Mishchenko et al. "Charge Dynamics of Doped Holes in High T_c Cuprate Superconductors: A Clue from Optical Conductivity". *Phys. Rev. Lett.* **100** (16 2008), p. 166401. DOI: 10.1103/PhysRevLett.100.166401.

[137] S. Zhou, Y. Wang, and Z. Wang. "Doublon-holon binding, Mott transition, and fractionalized antiferromagnet in the Hubbard model". *Phys. Rev. B* **89** (19 2014), p. 195119. DOI: 10.1103/PhysRevB.89.195119.

[138] E. Dagotto et al. "Optical conductivity of the two-dimensional Hubbard model". *Phys. Rev. B* **45** (17 1992), pp. 10107–10110. DOI: 10.1103/PhysRevB.45.10107.

[139] A. Comanac et al. "Optical conductivity and the correlation strength of high-temperature copper-oxide superconductors". *Nature Physics 2008 4:4* **4** (4 2008), pp. 287–290. DOI: 10.1038/nphys883.

[140] D. S. Fisher, G. Kotliar, and G. Moeller. "Midgap states in doped Mott insulators in infinite dimensions". *Phys. Rev. B* **52** (24 1995), pp. 17112–17118. DOI: 10.1103/PhysRevB.52.17112.

[141] J. Wagner, W. Hanke, and D. J. Scalapino. "Optical, magnetic, and single-particle excitations in the multiband Hubbard model for cuprate superconductors". *Phys. Rev. B* **43** (13 1991), pp. 10517–10529. DOI: 10.1103/PhysRevB.43.10517.

[142] *Polarons and Bipolarons in High-Tc Superconductors and Related Materials*. Cambridge University Press, 1995. DOI: 10.1017/CBO9780511599811.

[143] A. Alexandrov, V. Kabanov, and D. Ray. "Polaron theory of mid-infrared conductivity a numerical cluster solution". *Physica C: Superconductivity* **224** (1994), pp. 247–255. DOI: https://doi.org/10.1016/0921-4534(94)90261-5.

[144] O. Rösch et al. "Polaronic Behavior of Undoped High-T_c Cuprate Superconductors from Angle-Resolved Photoemission Spectra". *Phys. Rev. Lett.* **95** (22 2005), p. 227002. DOI: 10.1103/PhysRevLett.95.227002.

[145] A. J. Leggett. "A “midinfrared” scenario for cuprate superconductivity". *Proceedings of the National Academy of Sciences* **96** (1999), pp. 8365–8372. DOI: 10.1073/pnas.96.15.8365. eprint: https://www.pnas.org/doi/pdf/10.1073/pnas.96.15.8365.

[146] J. M. Ginder et al. "Photoexcitations in La_2CuO_4: 2-eV energy gap and long-lived defect states". *Phys. Rev. B* **37** (13 1988), pp. 7506–7509. DOI: 10.1103/PhysRevB.37.7506.

[147] Y. H. Kim, S.-W. Cheong, and Z. Fisk. "Dynamics of Photogenerated Charge Carriers in Cuprates". *Phys. Rev. Lett.* **67** (16 1991), pp. 2227–2230. DOI: 10.1103/PhysRevLett.67.2227.

[148] H. Okamoto et al. "Ultrafast charge dynamics in photoexcited Nd_2CuO_4 and La_2CuO_4 cuprate compounds investigated by femtosecond absorption spectroscopy". *Phys. Rev. B* **82** (6 2010), p. 060513. DOI: 10.1103/PhysRevB.82.060513.

[149] H. Okamoto et al. "Photoinduced transition from Mott insulator to metal in the undoped cuprates Nd_2CuO_4 and La_2CuO_4". *Phys. Rev. B* **83** (12 2011), p. 125102. DOI: 10.1103/PhysRevB.83.125102.

[150] T. Miyamoto et al. "Probing ultrafast spin-relaxation and precession dynamics in a cuprate Mott insulator with seven-femtosecond optical pulses". *Nature Communications 2018 9:1* **9** (1 2018), pp. 1–7. DOI: 10.1038/s41467-018-06312-z.

[151] I. Bozovic. "Atomic-layer engineering of superconducting oxides: yesterday, today, tomorrow". *IEEE Transactions on Applied Superconductivity* **11** (2001), pp. 2686–2695. DOI: 10.1109/77.919617.

[152] M. Dressel and G. Grüner. *Electrodynamics of Solids: Optical Properties of Electrons in Matter*. Cambridge University Press, 2002. DOI: 10.1017/CBO9780511606168.

[153] M. Born et al. *Principles of Optics: Electromagnetic Theory of Propagation, Interference and Diffraction of Light*. 7th ed. Cambridge University Press, 1999. DOI: 10.1017/CBO9781139644181.

[154] M. A. Dupertuis, M. Proctor, and B. Acklin. "Generalization of complex Snell–Descartes and Fresnel laws". *J. Opt. Soc. Am. A* **11** (1994), pp. 1159–1166. DOI: 10.1364/JOSAA.11.001159.

[155] K. Matsuda et al. "Femtosecond spectroscopic studies of the ultrafast relaxation process in the charge-transfer state of insulating cuprates". *Phys. Rev. B* **50** (6 1994), pp. 4097–4101. DOI: 10.1103/PhysRevB.50.4097.

[156] F. Novelli et al. "Witnessing the formation and relaxation of dressed quasi-particles in a strongly correlated electron system". *Nature Communications* (2014). DOI: 10.1038/ncomms6112.

[157] , familyi=v., given=Denis, giveni=D., „ et al. "Dynamics of photodoped charge transfer insulators". *Phys. Rev. B* **100** (4 2019), p. 041111. DOI: 10.1103/PhysRevB.100.041111.

[158] J. P. Falck et al. "Charge-transfer spectrum and its temperature dependence in La_2CuO_4". *Phys. Rev. Lett.* **69** (7 1992), pp. 1109–1112. DOI: 10.1103/PhysRevLett.69.1109.

[159] J. D. Perkins et al. "Midinfrared optical excitations in undoped lamellar copper oxides". *Phys. Rev. B* **58** (14 1998), pp. 9390–9401. DOI: 10.1103/PhysRevB.58.9390.

[160] J. D. Perkins et al. "Mid-infrared optical absorption in undoped lamellar copper oxides". *Phys. Rev. Lett.* **71** (10 1993), pp. 1621–1624. DOI: 10.1103/PhysRevLett.71.1621.

[161] J. C. Petersen et al. "Transient terahertz photoconductivity of insulating cuprates". *Phys. Rev. B* **96** (11 2017), p. 115133. DOI: 10.1103/PhysRevB.96.115133.

[162] T. Timusk and B. Statt. "The pseudogap in high-temperature superconductors: an experimental survey". *Reports on Progress in Physics* **62** (1999), p. 61.

[163] Z. Lenarčič and P. Prelovšek. "Ultrafast charge recombination in a photoexcited Mott-Hubbard insulator". *Physical Review Letters* **111** (2013), p. 016401.

[164] K. Shinjo and T. Tohyama. "Photoinduced absorptions inside the Mott gap in the two-dimensional extended Hubbard model". *Physical Review B* **96** (2017), p. 195141.

[165] Z. Lenarcic. "Nonequilibrium properties of Mott insulators". PhD thesis. University of Ljubljana, 2015.

[166] C Gadermaier et al. "Electron-phonon coupling in high-temperature cuprate superconductors determined from electron relaxation rates". *Physical review letters* **105** (2010), p. 257001.

[167] S. M. Gilbertson et al. "Ultrafast photoemission spectroscopy of the uranium dioxide UO 2 Mott insulator: Evidence for a robust energy gap structure". *Physical Review Letters* **112** (2014), p. 087402.

[168] R. Heid and K.-P. Bohnen. "Linear response in a density-functional mixed-basis approach". *Phys. Rev. B* **60** (6 1999), R3709–R3712. DOI: 10.1103/PhysRevB.60.R3709.

[169] S. G. Louie, K.-M. Ho, and M. L. Cohen. "Self-consistent mixed-basis approach to the electronic structure of solids". *Phys. Rev. B* **19** (4 1979), pp. 1774–1782. DOI: 10.1103/PhysRevB.19.1774.

[170] B. Meyer et al. *FORTRAN90 Program for Mixed-Basis Pseudopotential Calculations for Crystals, Max-Planck-Institut für Metallforschung*. Stuttgart (unpublished).

[171] D. R. Hamann, M. Schlüter, and C. Chiang. "Norm-Conserving Pseudopotentials". *Phys. Rev. Lett.* **43** (20 1979), pp. 1494–1497. DOI: 10.1103/PhysRevLett.43.1494.

[172] D. Vanderbilt. "Optimally smooth norm-conserving pseudopotentials". *Phys. Rev. B* **32** (12 1985), pp. 8412–8415. DOI: 10.1103/PhysRevB.32.8412.

[173] J. P. Perdew, K. Burke, and M. Ernzerhof. "Generalized Gradient Approximation Made Simple". *Phys. Rev. Lett.* **77** (18 1996), pp. 3865–3868. DOI: 10.1103/PhysRevLett.77.3865.

[174] A. Subedi and D. J. Singh. "Density functional study of $BaNi_2As_2$: Electronic structure, phonons, and electron-phonon superconductivity". *Phys. Rev. B* **78** (13 2008), p. 132511. DOI: 10.1103/PhysRevB.78.132511.

[175] B. Harbecke. "Coherent and incoherent reflection and transmission of multilayer structures". *Applied Physics B* **39** (1986), pp. 165–170.

[176] P.-O. Nilsson. "Determination of optical constants from intensity measurements at normal incidence". *Applied Optics* **7** (1968), pp. 435–442.

Acknowledgements

My PhD work would not have been possible without the help and creative input from many people in one way or the other. Whereas it is nearly impossible to list everybody who made a contribution, there are those who deserve special acknowledgment. First and foremost, I would like to thank my supervisor Professor Jure Demsar for giving me an opportunity to work in his group. I truly admire his unyielding support both professionally and personally and also giving me a freedom of exploring research independently. This has always kept me motivated and kept me in the right track throughout my PhD.

I would like to thank our sample providers Dr. A. A. Haghighirad, Dr. F. Iga, Dr. T. Takabatake, Prof. H. Okamura, Dr. G. Logvenov and Dr. I. Bozovic, without them my PhD project would have been just imaginary.

I would like to acknowledge the funding support from SFB TRR288 Elasto-Q-Mat and TRR 173-268565370 Spin+X.

My gratitude goes to my colleagues Volodia, Sergei, Amon and Tao for their tremendous support in the lab and also for making my PhD period more lively. Furthermore, special thanks goes to my office mate, Steinn Y. Agustsson for his constant support throughout my PhD. Interaction with him been an integral part of my PhD work.

It is entirely fitting to thank all my friends for their support during this truly stressful time. Special gratitude goes to my wife for her emotional support, encouragement and inspiration. My deepest gratitude goes to my sisters for their constant love and support.

Finally, I am forever indebted to my parents for their never ending support and always providing me all the fortitude necessary throughout all my studies. This thesis is dedicated to them.

...

PUBLICATIONS

The following is the list of published/in-preparation articles I authored during my doctoral studies.

[1] A. R. Pokharel et al. "Robust hybridization gap in the Kondo insulator YbB_{12} probed by femtosecond optical spectroscopy". *Phys. Rev. B* **103** (11 2021), p. 115134. DOI: 10.1103/PhysRevB.103.115134.

[2] A. R. Pokharel et al. "Dynamics of collective modes in an unconventional charge density wave system BaNi2As2". *Communications Physics 2022 5:1* **5** (1 2022), pp. 1–8. DOI: 10.1038/s42005-022-00919-x.

[3] A. R. Pokharel et al. "Dynamics of light-induced electron-hole pairs in the Mott insulator La_2CuO_4". *in-preparation* (2022).

[4] V. Grigorev et al. "Optically-triggered strain-driven Néel vector manipulation in a metallic antiferromagnet". *arXiv preprint arXiv:2205.05411* (2022).

[5] S Sobolev et al. "Time-resolved Studies of the Energy Gap Dynamics of Superconducting MgB_2 Thin Films Excited by Resonant Narrow-Band Terahertz Pulse". *in-preparation* (2022).